Exploring Cosmic-ray acceleration in the Galactic realm

David I. Jones
BSc(Hons)

School of Chemistry & Physics, University of Adelaide

October 20, 2009

A thesis submitted in total fulfillment of the requirements for the degree of Doctor of Philosophy

Introduction 1

This chapter gives a brief outline and discussion of fundamental topics which are important for the study of the cosmic ray (CR) spectrum which has blossomed over the 100-or-so years since the discovery that the ionization of atmospheric gas increased as a function of height (and hence were extra-terrestrial in origin) by Viktor Hess in 1912. Cosmic rays, as was the name given to the particles producing the observed ionization, are energetic, charged particles arriving at earth and although dependent on the energy, are composed mostly (90%) of protons. CRs have been studied using many different techniques, all of which are not discussed here, since this thesis deals with radio observations which can be used to explore the nature of the CR spectrum observed throughout the Galaxy (for a good review of CR research see Longair 1994).

Despite a concerted effort over the last ~50 years or so, we still do not have conclusive evidence of where and how CRs are accelerated to multi-TeV energies in Galactic sources. Since directional neutrino astronomy is at least 10–20 years behind γ-ray astronomy, a deeper understanding of how and where CRs are accelerated will come from improving evidence for either nucleonic or electronic source of γ-rays from Galactic sources. This is especially true for the Galactic centre (GC), where a detailed knowledge of particle acceleration in this region can aid with (i) answering the question as to why the GC is under-luminous with respect to other radio-loud galaxies (i.e. the lack of observable jets given the mass of the black hole inferred to exist at the GC) and (ii) application of particle acceleration in other galaxies.

The spectacular explosion in the number of Galactic objects that exhibit emission up to energies of a terra-electron volt (1 TeV $=$ 10^{12} eV) detected by instruments such as the High Energy Stereoscopic System (HESS), illustrates that particle acceleration up to energies >100 TeV (such as in RX J1713.7-3946) can occur in Galactic objects since the observed γ-rays are produced by particles at still higher energies. Typically it is thought that shell-type supernova remnants (SNRs) should be the dominant sites of Galactic CR acceleration up to $\sim 10^{15}$ eV (Ginzburg, 1964), where CRs are injected into SNR shock fronts and accelerated through diffusive shock acceleration. γ-rays can then be produced through the interaction of the CRs with ambient molecular matter and/or electromagnetic fields. The observation of γ-rays from a SNR however, is not conclusive evidence that SNRs can accelerate particles to this energy because processes such as inverse Compton scattering can produce TeV γ-rays by (previously accelerated) electrons that can up-scatter photons from various background photon fields (such as the cosmic microwave background).

1.1 The Cosmic Ray spectrum

Figure 1.1 shows the flux of CRs arriving at earth which is remarkably featureless over an amazing *twelve orders-of-magnitude in energy*. There are two departures from a spectrum following a power-law of exponent $\gamma = -2.7$ (for $dN/dE \propto E^{\gamma}$) – one at $\sim 10^{15-16}$ eV known as the "knee" and one at $\sim 10^{19}$ eV known as the "ankle".

NOTE:
This figure is included on page 2 of the print copy of
the thesis held in the University of Adelaide Library.

Figure 1.1: The flux of Cosmic rays at the top of the earth's atmosphere as a function of energy. Image sourced from `http://astroparticle.uchicago.edu/sciam1.jpg`

At the lowest energies, below ~ 1 GeV, CRs are prevented from reaching the earth by the solar wind and the strength of the local magnetic field. The Sun can also accelerate particles (also known as solar energetic particles) in events such as solar flares and are composed of mostly electrons, positrons and some protons, although these particles are not, strictly speaking, CRs. The composition of the CR spectrum is energy dependent although dominated by protons at most energies. By simple counting of all CRs at the top of the earth's atmosphere, 98% are protons and heavier nuclei, whilst 2% are electrons. The protons and heavier nuclei are represented by about 87% protons, 12% helium and about

1% heavier nuclei (Longair, 1994).

At the knee, the slope of the spectrum of CRs steepens for reasons which are not currently clear, although it has been hypothesized that it is the upper limit in energy that SNRs can reach (e.g. Protheroe & Clay (2004)). At energies between the knee and the ankle – $10^{15-16} \gtrsim E \lesssim 10^{19}$ eV – the origin of the CRs is thought to gradually change from Galactic to extragalactic. This is due to the theoretical expectation that CRs can only be accelerated in a region which is larger than the *gyro-radius*, r_g, of the particle which is defined as:

$$r_g = \frac{E}{ZeB},$$ (1.1)

where E is the energy of the particle, Z is the atomic number, e the charge and B the magnetic field amplitude. Thus Equation 1.1 shows that at energies of $\sim 10^{18}$ eV, the gyro-radius of a proton is on the order of the Galactic disk thickness of $h \sim 2$ kpc (Gaensler et al, 2008) (labelled as "d" in Figure 1.2). Hence particles at higher energies cannot be contained in the Galaxy and will escape – indeed this prediction is borne out in the observation that there is no significant excess in CR events with energies greater than $\sim 10^{20}$ eV from the direction of the Galaxy (Abraham et al., 2007).
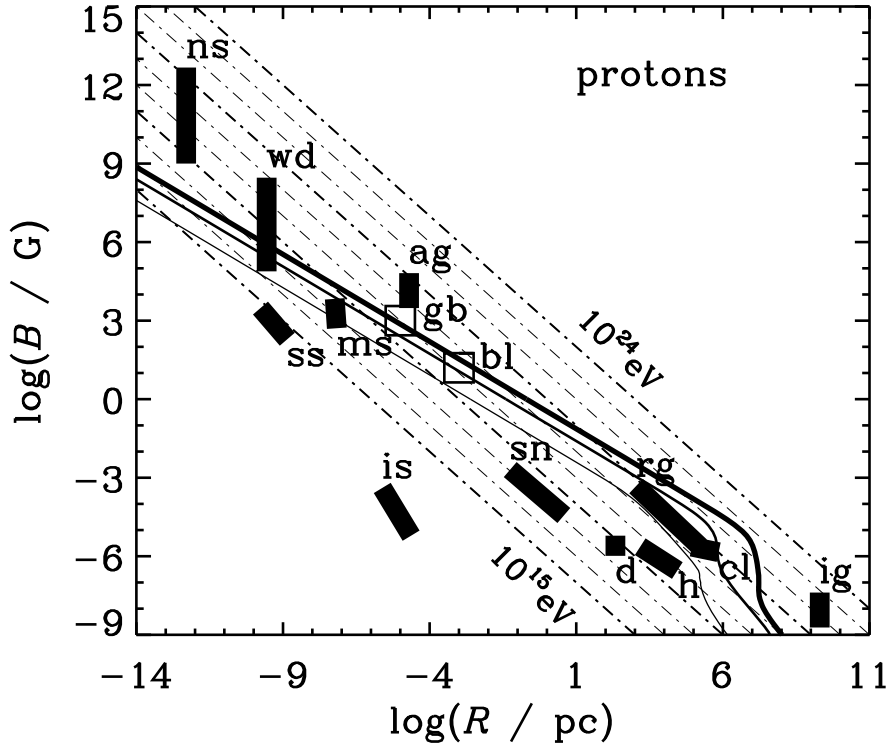

Figure 1.2: This plot, known as a Hillas diagram, (from Hillas (1984) after Protheroe (2004)) summarizes the size scales of objects which, for a given magnetic field, can accelerate particles up to an energy given by the diagonal lines. The solid lines are the maximum energy of proton acceleration of various efficiencies (see Protheroe (2004) for more details). The labels are: neutron stars (ns); white dwarves (wd); sunspots (ss); magnetic stars (ms); AGN (ag); interstellar space (is); supernova remnants (sn); radio galaxy lobes (rg); Galactic disk (d) and halo (h); clusters of galaxies (cl); and the intergalactic medium (ig). The open squares labelled "bl" and "gb" are two models for synchrotron proton blazars and γ-ray bursts – see Protheroe (2004) for details.

The theoretical expectation that the source size has to be larger than a particles gyrora-dius for the source to contain it has been neatly summarized by Hillas (1984). Figure 1.2

shows in what has become known as a Hillas diagram, the linear sizes of objects plotted against the expected magnetic field amplitude found within those sources. The diagonal lines show, as a function of source size and magnetic field, the maximum energy, E_{max}, to which a particle of a given atomic number can be accelerated. This can be derived by equating the maximum rate of energy gain with the rate of energy loss due to synchrotron for an electron and proton, so that the maximum energy achievable is (Protheroe & Clay, 2004):

$$E_e^{\text{max}} = 6.0 \times 10^2 \xi^{1/2} \left(\frac{B}{1\,\text{T}} \right)^{-1/2} \text{ GeV}, \tag{1.2}$$

$$E_p^{\text{max}} = 2.0 \times 10^9 \xi^{1/2} \left(\frac{B}{1\,\text{T}} \right)^{-1/2} \text{ GeV}, \tag{1.3}$$

where B is the magnetic field and ξ is an acceleration-mechanism dependent efficiency co-efficient.

Figure 1.2 shows that there are a number of possible sources of cosmic-rays, however it is thought that the main source of CRs in the Galaxy is supernova remnants (Longair, 1994). The main sources of extra-Galactic CRs at the highest energies are thought to be radio galaxies and clusters of galaxies (see below). Figure 1.2 also shows that the Galactic disk and halo is capable of accelerating particles up to very high energies. Given that the Galactic centre (GC) – which we define to be the central $2° \times 1°$ of the Galaxy – contains up to $\sim 10\%$ of the H_2 mass of the Galaxy, it is expected (and will be shown later) to be a very capable of accelerating particles to very high energies.

At the highest energies – $E \gtrsim 10^{16-17}$ eV and above – the sources of CRs observed at earth are thought to be extra-Galactic in origin. Theoretically, there should however, be a limit to the distance from which CRs can reach the earth, and this limit – calculated independently in 1966 by Greisen and Zatsepin and Kuzmin – is known as the GZK limit (Geisen, 1966; Zatsepin & Kuzmin, 1966). Greisen, Zatsepin and Kuzmin calculated that due to the interactions between CRs and the cosmic microwave background radiation (CMBR), there should exist a deficit of CRs with an energy above $\sim 6 \times 10^{19}$ eV. The mean path length associated with this interaction implies that only sources which are closer than about 200 Mpc (1 Mpc = 10^6 pc = 3.26×10^6 light-years; Abraham et al. 2007) should be a source of the highest energy CRs. Given the low flux of the highest energy CRs (c.f. Figure 1.1), the existence of this cutoff is still hotly debated, although data from the recently completed southern half of the Pierre Auger Observatory suggests that the flux of CRs is indeed highly attenuated above $\sim 6 \times 10^{19}$ eV (Abraham et al., 2007).

Nucleonic vs. Electronic acceleration

This thesis deals extensively with particle acceleration, which can be broadly categorized into two types: nucleonic and electronic particle acceleration.

The theme of this thesis, however, is not the particle acceleration *per se*, but what processes are responsible for the observed γ-ray and radio intensities. Thus throughout this thesis, the terms nucleonic and electronic acceleration pertains to the *dominant* γ-ray and/or radio continuum production mechanisms (i.e., a "nucleonic source" is a source where the γ-ray emission is predominantly produced by the decay of neutral pions created in proton-proton interactions and synchrotron emission via the production of secondary electrons and positrons).

It must be noted that most sources of CRs are expected to accelerate *both* electrons and nucleonic particles to CR energies, but here we again stress that when a source is labelled as a nucleonic or electronic source, it is done so because there is evidence that the subsequent radiation detected is dominated by processes attributable to nucleonic or electronic acceleration.

1.1.1 Galactic Cosmic rays

It was shown in the preceding section, that there are a handful of possible sources of CRs which we observe at the top of the earth's atmosphere which we discuss briefly here. Two of these source – SNRs and the GC – are the main topics of chapters in this thesis (Chapter 8 for SNRs and Chapters 7 and 9 for the GC) , and will be described there in more detail.

Supernova Remnants: SNRs

SNRs result from the violent deaths of massive stars (M$\gtrsim$ 5 M$_\odot$) that release huge amounts of energy and it was realized very early on (Baade & Zwicky, 1934) that they may be the dominant source of Galactic CRs. This is based on the observation that the CR luminosity of $L_{CR} \approx V_D \rho_{CR}/\tau_{esc} \sim 10^{41}$ erg s^{-1} matches that of a population of SNRs if only a small fraction of their kinetic energy is converted into CRs. The observed Galactic SNR rate of 1/30 yr and a conversion factor (for SNR kinetic energy to CR acceleration) of a few percent (Gabici et al, 2008) gives a general agreement to this model. This observation is reinforced by a great amount of effort in theoretical modeling, which has shown (and it will be shown in Chapter 4) that shocks resulting from the expansion of SNRs into the surrounding interstellar medium (ISM) can efficiently accelerate particles. Recently, a correlation of non-thermal radio emission from SNR shocks with VHE γ-ray emission discovered by Imaging Atmospheric Cherenkov Telescopes (IACTs; see Chapter 3 for an in-depth description of these telescopes) such as H.E.S.S.. This correlation is exactly what is expected to be produced when protons and heavier nuclei are accelerated by the shock fronts and interact with the ISM producing γ-rays through pion decay. In this scenario, the shock front associated with the SNR can lead to two results: (i) the surrounding matter (i.e., the ISM) being swept up into the shock front, and (ii) the amplification of the surrounding magnetic field if it is tied to the surrounding material.

There are, however, some considerable problems to overcome before the unambiguous detection of the acceleration of CRs from SNRs can be claimed. One such problem is that γ-ray emission in SNRs – although a nucleonic (i.e., protons) is favoured – can also be (in most cases) explained by electronic processes provided that the magnetic field amplification by the shock front is not too high (i.e., $B \lesssim 10\,\mu$G; Gabici et al 2008), since this leads to a lower flux due to inverse-Compton scattering compared to synchrotron emission (c.f. Chapter 4).

Pulsars & Neutron Stars

Pulsars and neutron stars are extremely rapidly rotating, compact objects which are supported by electron degeneracy pressure from collapse into a singularity. Since they are not of importance for this thesis, this description will be brief. There are two potential sites of CR acceleration in pulsars and neutron star:

1. During the collapse, the high ionization fraction of the matter results in a regime where the magnetic field lines are "frozen in" to the ionized material surrounding the object,

such that magnetic field amplitudes (in a dipole configuration) of $\sim 10^{13}$ G are created. From the huge electric fields generated by pulsars and neutron stars, particles can be accelerated because of the potential difference created up to a maximum energy of (G. Rowell, unpublished lecture notes):

$$E_{max} \sim 8 \times 10^{20} Z (B/10^{13} \text{ G})(\omega/3000 \text{ Hz})^2, \tag{1.4}$$

where ω is the rotational frequency of the star. Because of the magnetic field configuration, the newly accelerated particles are ejected along the axis of rotation of the object. If the earth is located along the line of sight of the magnetic axis of the object, the subsequent radiation (such as radio synchrotron emission from accelerated electrons) can be observed.

2. For various reasons (such as magnetic breaking), a pulsar or neutron star will decelerate, with a total *spin down power* of $\dot{E} = I\omega\dot{\omega} \sim 10^{32} - 10^{39}$ erg s^{-1} which is available to accelerate particles.

1.1.2 Sources of extra-Galactic cosmic-rays

There is much debate as to which extragalactic objects are able to accelerate CRs up to the highest energies (Abraham et al., 2007). Here we briefly discuss some potential sources, which broadly fall into two categories: bottom-up and top-down. Bottom-up sources are those in which the particles are accelerated from lower energies to ultra-high energies (UHE) within a region, such as a radio-galaxy, whereas top-down sources are those in which UHE CRs are created from topological defects.

Radio-galaxies

Extragalactic sources of CRs are most likely to be powerful radio galaxies, such as active galactic nuclei (AGN). It is thought that CRs are accelerated either from the centres of galaxies where supermassive black holes (SBH) are thought to accrete matter and expel them in objects known as jets, or from where the jets interact with the intergalactic medium producing shocks in regions known as hotspots (Protheroe & Clay (2004) and references therein).

Z-bursts and dark-matter

Amongst the most exotic possible explanations for the origin of extragalactic CRs are topological defects of various types, such as supermassive particles, cosmic strings, etc. (Protheroe & Clay, 2004).

1.2 Distribution of molecular matter in the Galaxy

Molecular line observations show that the density of matter along the line-of-sight increases towards the Sagittarius constellation, which lies in the direction of the centre of our Galaxy. Low density tracers, such as ^{12}CO show that the average molecular surface density is $\sim$ 5 M$_\odot$ pc^{-2} (Morris & Serabyn, 1996) until the central half-kiloparsec delineates a region which is known as the central molecular zone (CMZ). The CMZ contains $5 - 10 \times 10^7$ M$_\odot$ at a much higher density of $n_H \gtrsim 10^4$ cm^{-3} than that found in the disk of the Galaxy (and because of the high filling factors – $f \gtrsim 0.1$ – represents a surface density of several hundred M$_\odot$ pc^{-2}

and contains $\sim$ 10% of the H_2 mass of the Galaxy. Given such an extreme environment, it is not surprising that such a diversity of unique sources are found in this region.

1.2.1 The Galactic Centre

The centre of our Galaxy is a large subject of this thesis, and Figure 1.3 shows an image of the central 2° of the Galaxy at 330 MHz (LaRosa et al., 2000). Chapters 6 and 7 give a detailed description of most of the major sources in this image, so here we give a general overview of the region paying particular attention to the broadband spectrum of the region: for a more detail review, see Melia & Falke (2001).
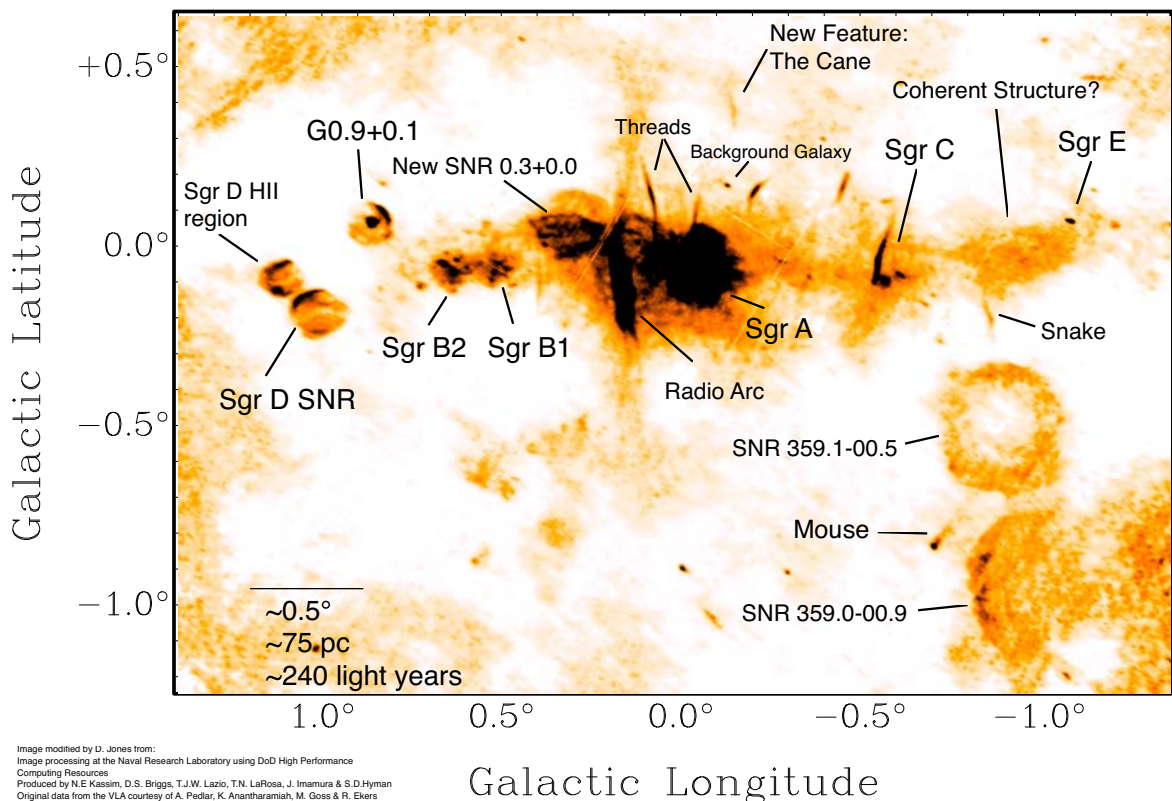

Figure 1.3: Image of the Galactic centre at 330 MHz (λ90 cm) from the VLA at a resolution of $42'' \times 24''$ (after LaRosa et al. (2000); see lower left for exact attributions). This shows the large variety of sources within the central 300 parsecs of our Galaxy.

Although our view of the GC is hampered at visible and ultra-violet wavelengths by $\sim$ 30 magnitudes of absorption by dust and gas (as evidenced in Figure 1.4, where the blue emission is due to dust emission). An absorption of 30 magnitudes is equivalent to an absorbing column of $N_H \approx 6 \times 10^{22}$ cm^{-2} (Predehl & Schmitt, 1995) and is extremely large, given an average Galactic value of a few $\times 10^{19}$ cm^{-2}. The view at other wavelengths represented by radio, infrared, X-ray and γ-ray observations however, is spectacular (c.f. Figures 1.3, 1.4 and 1.7 respectively). It shows that the GC contains a variety of sources such as SNRs, giant HII regions, and non-thermal radio filaments (NTFs): we now discuss this region briefly, paying particular attention to the structure of Sgr A (since the radio observations presented in Chapter 7 do not reveal the full structure of this important region) and the high energy spectrum and morphology of the region.
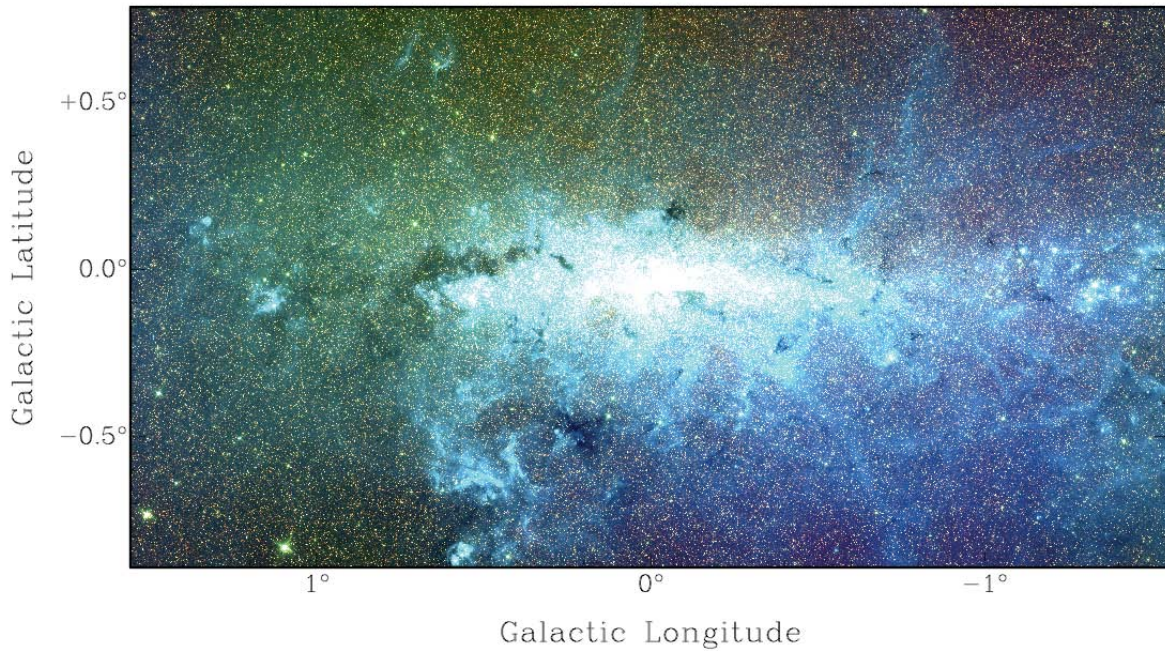
Figure 1.4: A 3-colour image of the GC at 4.5 μm (red), 5.8 μm (green), and 8.0 μm (blue) from the GLIMPSE satellite at a resolution of $\sim 2''$. The 8.0 μm emission traces Polycyclic Aromatic Hydrocarbons (PAHs), and is created by molecules created in massive hot stars being excited by UV photons. The 4.5 μm and 5.8 μm emission traces ionized and shocked gas.

Sgr A*

It was first hypothesized in 1971 by Lyden-Bell & Rees (1971) that the centre of our Galaxy should harbour a massive compact object. Three years later, Balick & Brown (1974) discovered a bright point source at radio frequencies located at the dynamical centre of the Galaxy (and is the bright point source at the centre of the spiral shaped source in Figure 1.5), however, it has taken until the last decade to establish that an object, with mass $M \approx 4 \times 10^6 \, M_\odot$ resides within a region of $\lesssim 0.015$ pc of the dynamical centre of our Galaxy (Baganoff et al. (2003) and references therein). That this source – dubbed Sgr A* – has been observed only at radio frequencies but has not been clearly observed at other wavelengths unlike the nuclei of other galaxies, makes Sgr A* a very enigmatic object (van Eldik, 2008). The non-detection of Sgr A* at high frequencies can best be illustrated by comparing the bolometric luminosity of a black hole of $4 \times 10^6 \, M_\odot$ radiating at the Eddington rate is $L_E \sim 3 \times 10^{44}$ erg s^{-1}, whereas the bolometric luminosity of Sgr A* is $\lesssim 10^{37}$ erg s^{-1} (Narayan et al, 1998), implying that either the accretion efficiency is extremely low or that the conversion of gravitational potential energy into radiative energy is very inefficient.

Radio observations of Sgr A* since its discovery have revealed that Sgr A* itself is a complicated source. Sgr A* has a spectrum which is non-thermal (i.e. $\alpha \lesssim -0.3$ for $S_\nu \propto \nu^\alpha$) at radio-continuum frequencies and there has only – so far – been a contentious detection of Sgr A* at 330 MHz (Nord et al (2004); see Roy & Rao (2006) for a discussion about the low-frequency detections of Sgr A*). Polarimetric spectral studies of the region have shown that Sgr A* is linearly unpolarized up to radio frequencies of 112 GHz with an upper limit of 1.8% (Bower et al., 2001). Circular polarization has been detected at frequencies as low as 4.8 GHz at a fractional percentage of −0.37% (Bower et al., 1999, 2002; Sault et al., 1999) with both the Very Large Array (VLA) and the Australia Telescope Compact Array (ATCA). At higher

frequencies, observations with the SCUBA camera on the James Clerk-Maxwell Telescope (JMCT) has shown that Sgr A* is not only linearly polarized at wavelengths between 750 and 2000 μm at a level of 10^{+9}_{-4}%, but that this polarization depends on frequency (Aitken et al., 2001). There have, to date, not been any convincing mid- or near-IR detections of Sgr A* (see Aharonian & Neronov (2005) for a review of the broadband spectrum of Sgr A*).

NOTE:
This figure is included on page 9 of the print copy of the thesis held in the University of Adelaide Library.

Figure 1.5: Sgr A at 4.8 GHz imaged with the VLA. Sgr A* is the bright point source, located at the centre of the spiral. Sgr A East is the shell like object at the left and Sgr A West is the spiral located in the west of the image. All of these sources are located within the Sgr A 7' 'halo' – see text and Chapter 7. Image taken from `http://www.astro.utu.fi/~cflynn/galdyn/l13.html`.

Sgr A

Figure 1.6 shows a schematic of the Sgr A region in Right Ascension and Declination co-ordinates from Baganoff et al. (2003). It shows that – as evidenced in the 4.8 GHz image of Figure 1.5 – Sgr A* is located within a spiral-like structure. This spiral is thermal in nature and is thought to consist of gas and dust which has been ionized by stars, spiraling around the Sgr A* (c.f. Figure 3 of Yusef-Zadeh, Melia & Wardle 2000). Surrounding these 'streamers' is a massive ($> 10^4$ M$_\odot$) and luminous ($L \sim 2 \times 10^7$ $L_\odot$; Yusef-Zadeh, Melia & Wardle 2000) toroidal configuration of matter known as the circum-nuclear disk (CND), which is observed with molecular line emission (see Yusef-Zadeh, Melia & Wardle 2000) and contains the streamers seen in Figure 1.5. The CND revolves at a velocity of ~ 112 km s^{-1} not around Sgr A*, but around a cluster of stars known as IRS 16 complex, which itself revolves about Sgr A* . The emission from the CND and the cluster region (also known as

the stellar-wind region; Crocker et al. (2007)) is explained by UV photons produced in the stellar-wind region being re-radiated as near- and far-IR photons by the CND. Altogether, the sources of Sgr A*, the streamers, and the CND, which are predominantly thermal, make up what is known as Sgr A West.

NOTE:
This figure is included on page 10 of the print copy of
the thesis held in the University of Adelaide Library.

Figure 1.6: (*Left): A schematic of the structure of the Sgr A region based on molecular line and radio continuum observations over the past* ~ 40 *years (Baganoff et al., 2003). (Right): Possible orientation of the positional structure of Sgr A based on radio-continuum and molecular-line emission (Yusef-Zadeh, Melia & Wardle, 2000).*

Figure 1.5 shows a low-level of emission to the east of Sgr A* from a source that is known as Sgr A East. Since Sgr A East has a non-thermal spectrum at radio-continuum frequencies and is shell-like in structure, it is hypothesized that this source is a SNR. Estimates of the kinematics required to produce a shell of this size in the GC environment infer that (assuming a single SNR event) the initial energy is ~ 10^{51} erg, an energy which is not inconsistent with an SNR.

All of these sources appear to be embedded in a large structure, known as the Sgr A 'halo' (as labeled in Figure 1.6). This structure, which is ~ 7′ in size, appears to be a mixture of thermal and non-thermal emission which can be explained by either a number of SNRs Pedlar et al. (1989) or ionized material with a component of non-thermal electrons accelerated by the collision of Sgr A East with nearby molecular clouds (Yusef-Zadeh, Melia & Wardle, 2000).

1.2.2 High energy emission from the GC

There has recently been much activity in the detection and characterization of the morphology and spectrum of the GC region at the highest energies. The X-ray satellites of *Chandra* and *XMM-Newton* have given an excellent view of the GC region at X-ray (1-10 keV) energies and high resolution (0″.5 − 10″), uncovering many features. At even higher (TeV) energies, the recent construction of high-sensitivity and high-resolution γ-ray instruments such as HESS has also given us an unparalleled view of the GC region.

X-ray emission

The large column depth towards the Galactic centre (viz. $N_H \sim 6 \times 10^{22}$) implies that the obscuring medium (gas and dust) first becomes partially transparent to X-rays at energies $\gtrsim 2$ keV. This has lead to numerous X-ray missions observing the GC regions since X-ray astrophysics was in its infancy (see Baganoff et al. (2003) and references therein). Early X-ray observations could only provide upper limits on the luminosity of Sgr A* itself at $L \approx 10^{35-37}$ erg s^{-1} until Baganoff et al. (2003) used *Chandra* to observe Sgr A* at arcsecond resolution with a luminosity of $\sim 2.4 \times 10^{33}$ erg s^{-1} (this is 10 orders-of-magnitude fainter than an X-ray source predicted by standard accretion models for the SBH) and found a source whose properties are consistent with accretion onto a SBH. They has also found observational evidence for variation of Sgr A* at X-ray energies on hourly timescales and longer (Baganoff et al. (2003) and references therein).

It has subsequently been shown that Sgr A* has two X-ray states: quiescent and flaring. The quiescent state shows a source with a steady flux, whereas in a flaring state, the X-ray luminosity increases to $2.89 \pm 0.41 \times 10^{35}$ ergs s^{-1} in the hard X-ray band[1], and is active on timescales $\lesssim 40$ minutes (Belanger et al., 2004).

On larger size scales, X-ray emission associated with all of the major sources of radio emission in Sgr A have been observed. The X-ray emission from Sgr A East implies that the shell of radio continuum emission is consistent with a Type II SNR, and that the X-ray emission from Sgr A West is the result of a thermal plasma that also produces the radio continuum emission (c.f. Figure 1.5). Large plumes rising from opposite sides of Sgr A, together with strong fluorescent line emission from cold Fe in Sgr B2 with no obvious irradiator nearby led Koyama et al (1996) to conclude that Sgr A* had an outburst about 300 years ago (the light travel time from Sgr A* to Sgr B2 assuming $d_{GC} = 8$ kpc) where the X-ray luminosity peaked at about 3×10^{39} erg s^{-1}.

γ-ray emission

The first spaced-based γ-ray observatories, such as OSSI and COS-B, were not sensitive enough to observe a source coincident with the GC at GeV energies. The first instrument to observe a source within the central few degrees of the Galaxy was the EGRET telescope (Meyer-Hasselwander, et al., 1998), although later analysis has shown that this source is not coincident with Sgr A (at a 95% confidence level: Pohl 2005). Analysis of this source revealed no evidence for the CR spectrum at GeV energies in the region being either (i) over-normalized with respect to the CR spectrum observed at the top of earth's atmosphere or (ii) having a different spectral index.

γ-ray emission was first detected from the GC region in 2004 by a number of γ-ray IACT telescopes, including Whipple, CANGAROO, H.E.S.S., and MAGIC (Kosack et al. (2004), Tsuchiya et al. (2004), Aharonian et al. (2004), Albert et al. (2006) respectively). The observations by the H.E.S.S. telescope, shown in Figure 1.7 (*Top*), have revealed a strong ($> 50\sigma$ from ~ 50 hours observations Aharonian et al. 2004) point source, roughly coincident with Sgr A. There is also a (weaker) source coincident with the SNR G0.9+0.1 (c.f. Figure 1.3 and Chapter 7), as can be seen in Figure 1.7 (*Top*). The point source spectrum – in contrast to the spectrum of the source observed by EGRET – shows that the spectral index is flatter (known as being "harder") than the local CR spectrum with a spectral index of

---

[1]here we define *hard* X-rays to be photons with energies from 10 to 100s of keV, and *soft* X-rays to be photons with energies of $1 - 10$ keV.
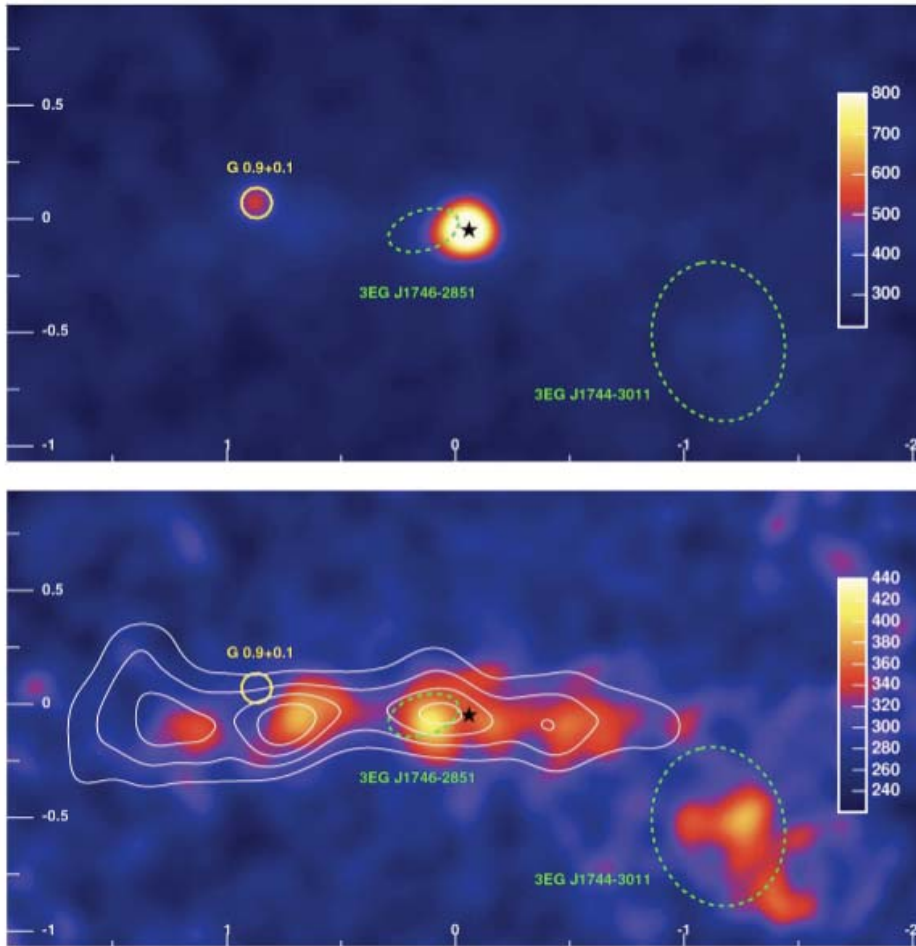
Figure 1.7: Image of the Galactic centre in TeV γ-rays from the HESS instrument (Aharonian et al, 2006). (*Top*): Image showing the two point-like sources, positionally consistent with Sgr A (the central black hole, Sgr A* is represented by the solid (black) star) and the SNR G+0.9+0.1. (*Bottom*): Image of the same region once the two point sources shown in the top panel have been subtracted. Overlaid on the TeV γ-ray emission are white contours showing the ^{13}CS emission within the region and illustrating the remarkable correlation of the TeV γ-ray and molecular line emission.

$\Gamma = -2.2 \pm 0.04(stat.) \pm 0.10(sys.)$, where "*stat.*" are statistical errors and "sys." are systematic errors (Aharonian et al., 2004). The spectral index determined by H.E.S.S. was also confirmed by the MAGIC γ-ray telescope, which found a spectral index of $\Gamma = -2.2 \pm 0.2$. In 2006, Aharonian et al (2006) showed that with over 100 hours of observation that the H.E.S.S. point source is coincident with Sgr A* within a position error of $\sim 2''$, which is consistent with Sgr A* being the source of the TeV γ-rays – in contrast with the EGRET source at GeV energies.

Figure 1.7 (*Bottom*) shows that in addition to the two point sources, there is a broad level of TeV γ-ray emission found in the GC region. There are a couple of important results from the analysis of this extended emission:

1. The spectral index of the extended emission is the same as that for the point source coincident with Sgr A*. Interestingly, this spectral index is not seen to vary as a function of position throughout the region.

2. The extended emission is also – as shown in Figure 1.7 (*Bottom*) – well correlated with the molecular line emission in the region (the white contours in Figure 1.7 (*Bottom*)

represent the ^{13}CS emission convolved to the ~ 4′ resolution of H.E.S.S.).

Models for VHE γ-ray GC emission from H.E.S.S. J1745-290

There are a number of possible models for the compact (as opposed to the extended) VHE γ-ray emission from the GC including acceleration of nucleonic and/or electronic particles and dark matter scenarios.

1. *Dark matter particle* decay or annihilation is perhaps the most exotic explanation for the VHE γ-rays from the central γ-ray source. This scenario is disfavored, however, because (i) the flat VHE γ-ray spectrum extending up to 20 TeV is hard to reproduce with most models for dark matter (Aharonian et al., 1997) and (ii) unnaturally high DM particle masses have to be assumed to account for the presence of emission at the highest energies (van Eldik, 2008).

2. *Electronic models*, such as strong and ordered magnetic fields close to the SBH event horizon (Aharonian & Neronov, 2005), stellar winds from massive stars close to the SBH (Quataert & Loeb, 2005), or the termination shock of the subrelativistic wind from the central part of the advection-dominated accretion flow on to the SBH (Atoyan & Dermer, 2005).

3. *Nucleonic models*, such as the acceleration of nucleonic particles in the GC region by one or more sources. In this scenario, the TeV γ-ray emission is produced by protons accelerated up to TeV energies close to the event horizon of the SBH, or in shocks in an accretion disk located close to the event horizon.

4. *The pulsar Wind Nebula G359.95-0.04*, which was discovered in a recent deep *Chandra* exposure of the GC by Wang, Lu & Gotthelf (2006). Despite the low X-ray luminosity of this object, it has been shown by Hinton & Aharonian (2007) that this source can simultaneously explain the X-ray and γ-ray energy emission with a population of non-thermal electrons.

The nucleonic and electronic scenarios discussed above both predict that the γ-ray emission should be correlated with longer wavelength variability (van Eldik, 2008). Searches for time-variability (on all time scales of days, months and years, between instruments sampling different size scales), has not revealed an observed correlation of γ-ray emission with emission at other wavelengths. Although this does not rule out nucleonic and/or electronic particle acceleration near the SBH as the primary mechanism for the production of the observed TeV γ-ray emission, it perhaps points to other sources, such as the PWN G359.95-0.04 as the source.

1.3 Galactic magnetic fields

This thesis uses non-thermal synchrotron emission from (primary or secondary) electrons together with an expectation for the CR spectrum in a region of the Galaxy to infer magnetic field amplitudes. Since magnetic fields play an important role in not only particle acceleration, but also gas dymamics, and star formation in the Galaxy, there has been much effort in the past to try and determine the strength and structure of the magnetic field amplitude – both in general and on small scales – within the Galaxy. This section summarizes current knowledge of magnetic field amplitude and structure in our Galaxy.

1.3.1   Methods for determining magnetic field strength and structure

The large scale magnetic field structure within the Galaxy has been explored using a number of methods that mainly deal with polarized radio synchrotron emission due to (relativistic) CR electrons within the Galaxy. Additionally, thermal electrons in the hot component of the ISM will rotate the electric vector of the light emitted from pulsars, with the amount of rotation proportional to the magnetic field strength along the line-of-sight.

Dispersion and Rotation Measures as an estimate of the Galactic Magnetic field

The amplitude of the magnetic field along the line of sight can be obtained through the careful study of the arrival time of radio pulses from pulsars. Because the emission from pulsars is polarized, the ionized component of the ISM between the pulsar and us will cause the electric vector of the light to rotate an amount which is proportional to:

$$\theta = 0.81\lambda^2 \int_0^l n_e B_{\parallel} dl = 0.81\lambda^2 RM \text{ [rad]}, \tag{1.5}$$

where λ is the wavelength of the emission in meters, n_e is the electron number density in the ISM in electrons cm^{-3} , $B_{\parallel}$ is the parallel component of the magnetic field measured in Gauss and the integral is taken over the path-length, l between us and the pulsar measured in parsecs. Measurements of the delay times of pulsar signals as a function of frequency can be used to obtain an estimate of the free electron content of the Galaxy. This quantity (the delay of signals as a function of frequency) is known as the dispersion measure (DM) and is:

$$DM \approx 4.15 \times 10^9 \frac{1}{\nu^2} \int_0^l n_e dl \text{ [s]}, \tag{1.6}$$

where n_e is the electron density measured in electrons cm^{-3} , ν is the frequency in Hz and l is the distance in parsecs. Thus one can obtain an estimate of the magnetic field amplitude along the line-of-sight:

$$B_{\parallel} \sim \frac{RM}{DM}, \tag{1.7}$$

where the sign of $B_{\parallel}$ gives information about the direction of the magnetic field component parallel to the line-of-sight. Through studies of pulsars throughout the Galaxy, nominal values of $n_e \sim 1$ cm^{-3} and $B_{\parallel} \sim 6\,\mu$G are obtained. It should be noted, however, that this only applies to regular magnetic field structures over a given region. If there are field complexities, such as turbulence and irregularities, then the estimate of the field strength and direction become dependent on the magnetic field structure.

Polarization of Starlight

Another way to measure the strength of the Galactic magnetic field is to look at the polarization of starlight throughout the Galaxy. At optical wavelengths, the amount of polarization has been found to increase with distance through the Galactic plane, and strongly correlates with the extinction by interstellar dust. This occurs because the dust grains scatter preferentially scatter the incident starlight with the electric vector parallel to the dust grain's major axis (Longair, 1994). The magnetic field of the Galaxy is thought to align dust grains on large scales leading to the correlation. The mechanisms for this alignment are thought to be the ferromagnetic properties of the grains such that their minor axes will be parallel to the magnetic field direction (Longair, 1994).
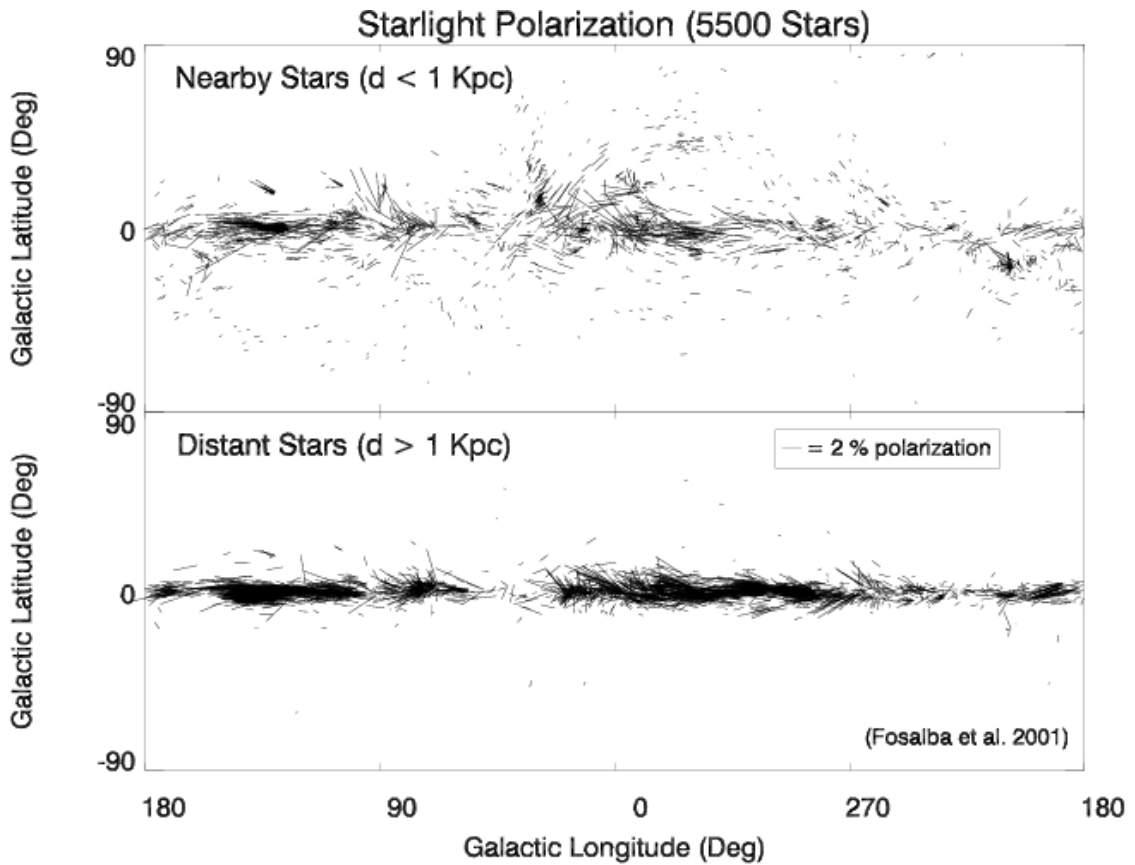
Figure 1.8: Polarization direction and strength (vector length is proportional to strength) as a function of Galactic longitude and latitude for (*Top*) nearby stars of $d \lesssim 1$ kpc and (*Bottom*) farther stars of $d \gtrsim 1$ kpc. This plot shows the large scale structure of the magnetic field of the Galaxy as traced by polarized starlight.

A plot of the polarization strength and direction, shown in Figure 1.8, reveals that the structure of the magnetic field is primarily parallel to the plane of the Galaxy. Because of our location, the top panel is thought to be because it is tracing the structure of the local spiral arm in which we are located, however, several prominent features can be observed, such as the North Polar Spur – a large magnetic loop rising out of the plane at $\sim l = 30°$. The length of the vectors in Figure 1.8 indicates that the strength of the Galactic magnetic field is $\sim 6\,\mu$G.

Zeeman Splitting of 21 cm and OH maser emission lines

The strength and structure of the magnetic field in the Galaxy can also be probed via the observation of the splitting of the 21 cm neutral hydrogen line or 1720 MHz OH-maser emission into several components. Neutral hydrogen, which consists of a single proton and an electron, emits a photon when the spin of the electron changes. The presence of a magnetic field whose field lines are parallel to the line-of-sight results in two emission lines which are circularly polarized in the opposite sense (i.e., a left and right handed polarised line profile) on each side of the central line frequency of 1420 MHz. The frequency separation of these lines is proportional to the line-of-sight magnetic field strength and can also occur in maser species, such as the most commonly studied OH-maser lines at 1720 MHz.

Using this technique, the estimated average Galactic magnetic field strength is $\sim 10\,\mu$G –

higher than the estimates derived using the techniques described above. This discrepancy is thought to be due to selection effects, in that the line separation (for the 21 cm line) from Zeeman splitting amounts to 28 GHz T^{-1}, so that detectors have to be sensitive to a line separation of 10 Hz at 1420 MHz (Longair (1994); for reference, spectral-line observations with the ATCA has channels which are, at most, ~ 2 kHz in width). The necessity for such a high degree of spectral precision leads to unambiguous detections only in regions where there is a higher magnetic field, since these regions will have lines which are separated by a larger band in frequency.

1.3.2   The amplitude and structure of the Galactic Magnetic field

Although there are some very good tools with which to probe the structure of the magnetic field in the Galaxy, there are conflicting lines of evidence, and comparisons with extra-Galactic sources provide more confusion. Here we summarize the current state of knowledge. For an excellent review, see Beck (2008).

Magnetic field amplitude

The magnetic field within our Galaxy has been observed to be generally well correlated with that of the matter density of the Galaxy (Crutcher, 2007). This may arise because in regions with a high ionization fraction (such as star formation regions, which are preferentially found in the spiral arms and the GC), the magnetic field lines become 'frozen into' (i.e. following Alfvén's theorem) the matter so that when the density increases, so does the magnetic field. Using an average molecular hydrogen density of $\sim 10^3$ cm^{-3}, Crutcher (2007) derived an average value of the magnetic field amplitude in the Galaxy of $\sim 6 \pm 1.8\,\mu$G based on a density correlation power-law of order $n^{0.65\pm0.05}$ and consistent with the techniques presented above.
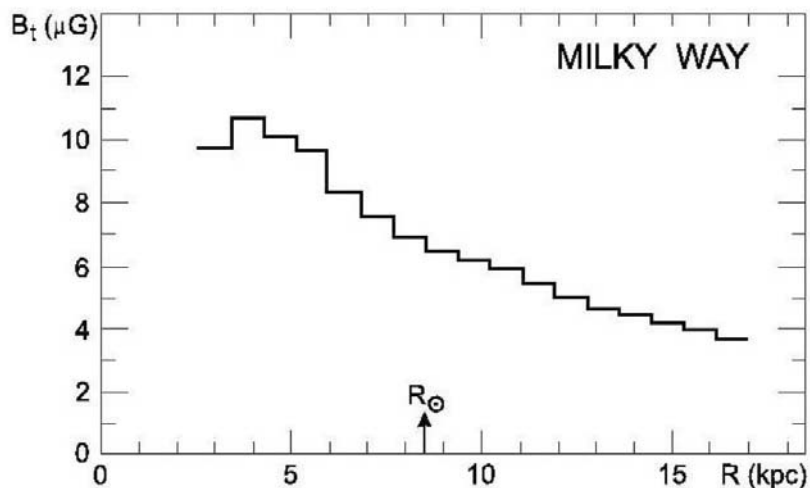

Figure 1.9: The magnetic field amplitude of the Galaxy as a function of Galacto-centric radius estimated from equipartition considerations, and a CR energy density derived from GeV γ-ray observations (Beck, 2008).

This can be compared to the expected magnetic field strength derived from equipartition arguments (which are explored in more detail in Chapter 9), which is shown as a function of Galactocentric radius in Figure 1.9. Equipartition considerations can produce an estimate of the magnetic field amplitude by assuming that the energy density in (the regular component

of) magnetic fields are in rough equipartition with the energy density of CRs. As Figure 1.9 shows, the equipartition magnetic field amplitude of the Galaxy is ~ 6 μG at the solar-circle (the Galacto-centric radius at which the Sun is located) and rises to ~ 10 μG towards the GC. γ-ray emissivities can provide a test as to the validity of the equipartition argument, since the equipartition field strength is only a function of magnetic field and CR density. This follows for two reasons: (i) GHz synchrotron photons for reasonable (i.e., μG) magnetic fields are produced by ~GeV electrons and (ii) observations of GeV γ-rays suggests that they trace the molecular emission and hence imply a nucleonic origin to the emission. The fact that these estimates match well is a positive sign that the equipartition argument – at least locally – is valid.

There is some evidence, however, that such an assumption may not be valid everywhere – especially in starburst galaxies (Thompson et al., 2006). As such, equipartition arguments are currently under debate in extreme regions and should only be used as a lower-limit for the magnetic field amplitude in the Galactic centre – this debate is the subject of Chapter 9.

Magnetic field structure

Although there is reasonable agreement on the amplitude of the Galactic magnetic field (at least locally), there is not such good agreement on the structure of the magnetic field. Figure 1.10 shows a model for the structure of the Galactic magnetic field (Sun et al., 2008). This model is derived from observations of polarized (radio-continuum) emission and RMs from extra-Galactic sources and show a regular magnetic field structure with a magnetic field reversal at ~ 1 − 2 kpc inside the solar-circle – the Sagittarius/Carina arm of the Galaxy – and agrees with studies from the RMs of Southern Galactic Plane pulsars (Brown et al., 2007).

Other evidence, however, does not agree with this model, in that additional structure of the field is required. More detailed anayses (Beck (2008) and references therein) of the RM of pulsars indicate that the magnetic field has two more field-direction reversals: one in the Perseus arm and again in the inner molecular ring. A third possibility is that there are just two reversals: between the local-field and the Carina arm and another between the Carina and the Crux arm (Noutsos et al., 2008).

These lines of evidence – mostly derived from studies of populations of RMs from pulsars – show that not only is the number of field reversals uncertain, but the position of reversal is also a matter of debate. Indeed, when models of the magnetic field structure observed in our Galaxy are searched for in other galaxies, there seems to be a lack of evidence that this sort of magnetic structure is common (though this may be because of the relatively coarse beams with which we can study other galaxies compared to our own).

1.4 Conclusions

This chapter has provided a brief outline of the importance and difficulties which are inherent in discovering the sites of CR acceleration within our Galaxy and beyond. We have shown that despite almost a century of intense research, we are little closer to finding concrete evidence for CR accelerators – although the Pierre Auger Observatories discovery of a correlation between CR events at $E \gtrsim 10^{18}$ eV and AGN in the local universe is a big step.

We have also presented a rough outline of the two mechanisms which are possible for the production of CRs: nucleonic and electronic acceleration. We have summarized the

NOTE:
This figure is included on page 18 of the print copy of
the thesis held in the University of Adelaide Library.

Figure 1.10: An axisymmetric model for the Galactic magnetic field in Galacto-centric coordinates as seen from the north Galactic pole. The vector length indicates magnetic field amplitude with the local regular component of the field shown in the top left of the figure. The opposite direction magnetic field direction are indicated by the thicker vectors. The structure of the field comes from polarization and rotation measure estimates (Sun et al., 2008).

main sources from which it is thought that CR nucleons and electrons are accelerated up to the highest energies. We have summarized our knowledge of our place in the Galaxy in terms of its molecular and magnetic structure. We have shown that, although great progress has been made since the maturation of radio astrophysics, there are large gaps in our knowledge about the structure of the magnetic field which permeates the Galaxy.

We have presented evidence of the large and growing investigation of high- and very-high energy phemonena in the central couple of parsecs of our Galaxy. Recent X-ray and VHE γ-ray observations have shown that the structure in this region – representing the closest example of a SBH available – is just as complicated and fascinating as at radio wavelengths.

Finally, we note that since directional neutrino astrophysics will not be a mature observational science for the foreseeable future, methods using current high-sensitivity, high-resolution instruments – such as radio interferometers and γ-ray telescopes – are the best way to elucidate the nature of CR acceleration within our Galaxy.

Fundamentals of radio astronomy 2

2.1 Introduction

The work presented in this thesis relies upon both single- and multiple-dish (also known as an interferometer) astronomy. In this chapter, we outline the basic principles which govern radio astronomy. The basic techniques used in aperture synthesis radio astronomy, which is a specific type of radio interferometer, since the observations presented in this thesis were obtained with the Australia Telescope Compact Array (ATCA) and the Very Large Array (VLA)[1] are discussed. Because much of this thesis is based on the observations of bright and complex regions, we place a particular emphasis on image deconvolution techniques.

The published collection of lectures from the Sixth NRAO/NMIMT Synthesis Imaging Summer School (Taylor, Carilli & Perley (1999); hereafter, TCP99) contains a great deal of discussion of the fundamentals of radio aperture synthesis imaging. The details from a number of these lectures (primarily Lectures 1 (Clark), 2 (Thompson), 5 (Fomalont & Perley), 8 (Cornwell, Braun & Briggs) and 9 (Wrobel & Walker)) are summarised here.

2.2 Fundamentals of radio interferometry

Radio astronomy can be thought of as the measurement of the intensity distribution, $I_\nu(l,m)$, in the direction, $\vec{s}$, of a source located at $\vec{R}$, after its propagation to Earth. Because for a radio telescope of diameter, D, observing at wavelength λ, the angular resolution θ, is set by the Rayleigh criterion, $\theta \sim 1.22\lambda/D$, unrealistically large dish sizes are required for high resolution imaging to be practicable with single-dishes. Instead of adding this signal over a time interval as is the case in single-dish radio astronomy, the solution is to connect two smaller dishes and measure the *spatial coherence function* (also known as the "visibility function"), defined as:

$$V_\nu(\vec{r}_1, \vec{r}_2) = \int I_\nu(\vec{s}) e^{-2\pi i \nu \vec{s} \cdot (\vec{r}_1 - \vec{r}_2)/c} d\Omega, \tag{2.1}$$

where ν is the frequency, c is the speed of light, and the integral is taken over solid angle $d\Omega$ of the celestial sphere. Essentially, the spatial coherence function is how well the signal, received at each antenna correlates (in the sense that the multiplication of the (complex) signals received at each telescope from a source constructively interferes).

For the observation of a source, Figure 2.1 shows the definition of a coordinate system where the component of the separation vector between the two dishes is $\vec{r}_1 - \vec{r}_2 = (u, v, w)$ and $\vec{s} = (l, m, n = \sqrt{1 - l^2 - m^2})$ is the vector component towards the source. If there is only an east-west component to an interferometer (which is true for the ATCA, but not the VLA),

---

[1]It must be noted that the VLA data were observed and reduced by others.

NOTE:
This figure is included on page 20 of the print copy of
the thesis held in the University of Adelaide Library.

Figure 2.1: Coordinate system used for synthesis imaging. The (u, v, w) and (l, m, n) right handed cooredinate systems are used to express interferometer baselines and source brightness distribution respectively. Sourced from `http://www.merlin.ac.uk/user_guide/OnlineMUG/newch0-node33.html`.

then the interferometer is said to be co-planar, and one can set $w = 0$, reducing Equation 2.1 to a two dimensional Fourier transform:

$$V_\nu(u, v) = \iint I_\nu(l, m) \frac{e^{-2\pi i(ul+vm)}}{\sqrt{1 - l^2 - m^2}} dl dm. \tag{2.2}$$

Equation 2.2 shows that in radio interferometry, there are two fundamental planes: (i) the sky plane, represented by the (l,m) coordinates in Figure 2.3, and (ii) the telescope plane which is known as the *uv*-plane, represented by the (u,v) coordinates. Importantly, it also shows that *the relationship between the sky-plane, and the telescope plane is related by a Fourier transform.*

In order to image a source, Equation 2.2 has to be inverted to recover the original intensity distribution. There are however, numerous effects which hamper such a simple recovery of the intensity distribution, which we now discuss.

2.2.1 The effects of discrete sampling

Interferometry by its very nature will not sample every position in the *uv*-plane, since it is not (usually) desirable for two elements (as telescopes are known as) in an array to be so close as to hinder the performance of the element. (When the field-of-view of a telescope is hindered by another telescope, this is known as shadowing. Shadowing is a problem for most telescopes, but particularly for East-West arrays, such as the ATCA observing sources near the celestial equator. Although advantageous to avoid during observation, the data reduction software package, MIRIAD, used in this thesis takes account of visibilities that are affected by shadowing.)

It is also assumed that each pair of elements sample and average the incoming signal over a time period which is shorter than the time over which the complex gains, noise and offsets are expected to vary. Since the field of view (FoV) of a telescope is limited because of the Rayleigh criterion, then these changes are going to come from the edge of the FoV, and it can be shown that this implies that the integration time, Δt in seconds, of the interferometer should be:

$$\Delta t_{\text{int}} \lesssim 2D/B_{\text{km}}, \tag{2.3}$$

where B_{km} is the baseline distance in kilometers and D is the diameter of the dish in meters. Due to the large amounts of data that can be generated from observations, and the need to have as many independent samples in the uv-plane as is possible, the integration time is a trade-off. In some cases, such as very long baseline interferometry, where sources can be extremely compact and large amounts of data can be generated, the entire primary beam area may not be imaged. The effect of not imaging the entire primary beam is equivalent to increasing the diameter of the dish which, in turn, allows a longer sample time. This is because the Fourier transform of the primary beam (in the image plane into the uv-plane) is a Gaussian: convolving each sample visibility in the uv-plane by this Gaussian, will make the sample larger. In general, however, and for the observations presented in this thesis, it is wise to image an area larger than the primary beam. This is because (strong) sources outside the primary beam area can affect imaging and degrade sensitivity. Deconvolution of a region which includes these sources will mitigate their effect on the entire image. The Fourier relationship between the sky and telescope planes also makes it necessary to adequately sample in time (i.e., at or higher than the Nyquist rate), so that small smaller averaging times give smaller points in the uv-plane and vice-versa.

In practice then, the visibility function is sampled only at discrete places on the uv-plane so that Equation 2.2 is modified by a sampling function, $S(u, v)$, which is constructed such that the function is zero where no data has been taken. The intensity function is then given by:

$$I_\nu^D(l, m) = \iint V_\nu(u, v) S(u, v) e^{2\pi i(ul+vm)} du dv, \tag{2.4}$$

which is usually referred to as the *dirty image*. Inspection of Equation 2.4 shows that because of the sampling function, a simple two-element interferometer will lead to poor image reconstruction. It is for this reason that in practice, interferometers are constructed with many dishes located in specific positions so as to sample the uv-plane as evenly as possible.

Because of the Fourier relationship between the uv-plane and the sky plane, the dirty image can be neatly expressed as the convolution of the actual intensity distribution, $I_\nu(l, m)$ and the *synthesised beam* or *point spread function, B*, so that:

$$I_\nu^D = I_\nu * B. \tag{2.5}$$

That is, B is the Fourier transform of the sampling function:

$$B(l, m) = \iint S(u, v) e^{2\pi i(ul-vm)} du dv. \tag{2.6}$$

Obtaining the true source intensity, I_ν from the *dirty image* I_ν^D is known as *image deconvolution*, and is described in detail in Section 2.4.

2.2.2 The effect of finite bandwidth

Until now, there is an implicit assumption that any interferometer measuring sky visibilities as per Equation 2.2 does so over a sufficiently small range of bandwidth so as to be called *monochromatic*. In practice, an interferometer will sample the incoming electromagnetic wave over a range in frequency, and so one should consider the response of an interferometer in the case limited bandwidth.

<div style="border:1px solid black; padding:1em; text-align:center;">

NOTE:
This figure is included on page 22 of the print copy of
the thesis held in the University of Adelaide Library.

</div>

Figure 2.2: Fringe amplitude as a function of angle from phase centre illustrating the decrease in sensitivity as one gets further from the phase centre of an observation. The 'fringe amplitude' is the real part of the complex cross-correlation product normalised to the total power of a source. Figure taken from 'Fundamentals of Radio Astronomy' lecture given by R. A. Perley, given at the Ninth Synthesis Imaging School, Socorro, New Mexico, June 15–22, 2004.

To illustrate the effect of finite bandwidth on aperture synthesis imaging, we define a function $G(\nu)$ as the amplitude and phase variation of the signal's path in frequency. If the source does not vary over the chosen bandwidth, $\Delta\nu$, at a central frequency ν_0, then the finite bandwidth changes the visibility function of Equation 2.2 to:

$$V = \iint I_\nu(\vec{s})\text{sinc}(\tau_g \Delta\nu)e^{-2i\pi\nu_0\tau_g}d\Omega, \tag{2.7}$$

where the $\text{sinc}(x)$ is defined as:

$$\text{sinc}(x) = \frac{\sin(\pi x)}{\pi x}, \tag{2.8}$$

and

$$\tau_g \sim \frac{B}{c}\sin\theta \sim \frac{B\theta}{\lambda\nu} \sim \frac{\theta}{\theta_{res}\nu}, \tag{2.9}$$

where B is the distance between two interferometer elements, c is the speed of light, λ is the wavelength, θ/θ_{res} is the source offset in units of the fringe separation. A 'sinc' function is used in Equation 2.7 because, although the functional form in the time domain is a sinusoid, in frequency space it is a rectangular function and so the 'sinc' function acts as a bandwidth filter. The effect of this filter is to decrease the response of the interferometer as a function

of angle from the phase centre until a zero is reached at $(\Delta\nu/\nu)(\theta/(\lambda/B)) = 1$, as can be seen in Figure 2.2.

The above analysis shows that because interferometers can only observe with a finite bandwidth, this will cause a loss of coherence towards the edge of the field known as bandwidth smearing (chromatic aberration). Thus when planning observations, one has to bear in mind that if a sources intrinsic size approaches that of the primary beam size, then there will be a loss of coherence, especially if the bandwidth is large. This effect is overcome by splitting up the bandwidth into a number of channels and performing the Fourier transform channel by channel. This gives the added benefit of sampling a larger part of the uv-plane (and in image deconvolution with ATCA data is known as 'multi-frequency synthesis'). Conversely, if one ignores the larger extent of the sample in the uv-plane, then there are errors introduced into the imaging process, the result of which is bandwidth smearing. It should be noted that the VLA data used in this thesis has been taken in 'spectral mode', which gives a finer bandwidth of the channels so as to mitigate the effect of bandwidth smearing.

2.2.3 Earth-rotation synthesis

As discussed above, to image a source at sufficiently high resolution and sensitivity (c.f. Equation 2.15), one needs to sample the uv-plane at a large number of positions. The simplest way to do this is to point the telescope on a source and let the earth rotate which makes such observations known as *Earth-rotation synthesis*. When the elements of an interferometer are aligned in an east-west direction, the path traced out by successive samples as projected onto the uv-plane will be an ellipse. Placing telescopes at various distances from one another will cause ellipses of varying *uv-distances* to be traced out in the uv-plane. This is evidenced in Figure 2.3, where the VLA has been used to observe a source as the earth rotates. This figure also illustrates how when baselines are not co-planar, then the paths traced by each baseline is not necessarily ellipses with loci at the center of the uv-plane.

Figure 2.3 also illustrates that earth-rotation synthesis cannot sample the uv-plane at the centre. This position in the uv-plane corresponds to the total power point (i.e., the flux density contained within the entire FoV of the telescope), and can only be obtained through the addition of single-dish data (c.f. Section 2.5.3).

2.3 Calibration

The previous section showed how, under certain simplifying assumptions, a pair (or more) of antennae samples the spatial coherence function. The data from each pair of antennae is then recorded, and each baseline defines a point on what is known as the uv-plane, and are known as *visibilities*. However, the recorded visibilities differ from the true visibility because one cannot build a "perfect" radio telescope (in the sense that Equation 2.1 is exact). The process of identifying errors in the visibility data and correcting them is known as *calibration*.

The actual visibilities recorded by an interferometer, $\tilde{V}_{i,j}(t)$ (the subscripts i and j refer to a particular pair of antennae, or baseline) are related to the true visibilities, $V_{ij}(t)$, by a simple linear relationship (if the interferometer is soundly engineered):

$$\tilde{V}_{i,j}(t) = G_{ij}(t)V_{ij}(t) + \epsilon_{ij}(t) + \eta_{ij}(t), \tag{2.10}$$
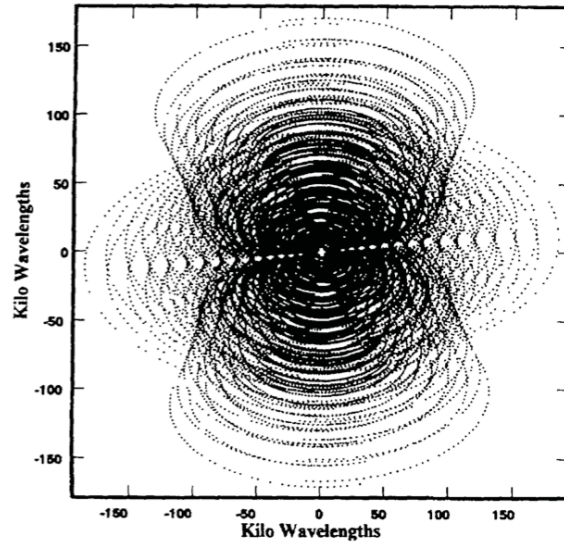
Figure 2.3: An example of the *uv*-plane coverage for an observation with the VLA at a declination of 30° from Stanimirovic (2002). Note that the samples do not trace out regular ellipses, as would be with a co-planar interferometer, such as the ATCA. Also note the complete absence of samples at the centre of the *uv*-plane (i.e., where $u = v = 0$): this is the total power, and the issues with this are discussed in Section 2.5.3.

where t is the time of the observation, $G_{ij}(t)$ is the baseline-based complex gain, $\epsilon_{ij}(t)$ is the baseline-based complex offset, and $\eta_{ij}(t)$ is a stochastic complex noise. That the components here are complex is a convenience: it is the combination of two correlator outputs into one complex quantity.

The complex gain factor can be approximated by the product of the two associated antenna based complex gains (since most errors occur *before* the signal is correlated) $g_i(t)$ and $g_j(t)$,

$$G_{ij}(t) = g_i(t)g_j^*(t) = a_i(t)a_j(t)e^{i(\phi_i(t)-\phi_j(t))}, \tag{2.11}$$

where $a_i(t)$ is an antenna based amplitude correction and $\phi_i(t)$ is an amplitude based phase correction. These corrections are determined by the use of *amplitude and phase calibrators* (known as primary and secondary calibrators) at suitable times during the observations. The absolute flux density of an observation is scaled using the primary (amplitude) calibrator, which for the ATCA is 1934-638, which must be observed at some point during every observation run (although because of the steep spectrum of this source, observations at higher frequencies – such as millimeter wavelengths – objects such as Uranus has to be used as a primary flux calibrator). The gains and phases are then calibrated using a secondary calibrator (a strong point source located near the source of interest) observed regularly (at least once an hour) throughout the observational period.

2.4 Image deconvolution

As was seen in Section 2.2.3, using a strictly east-west interferometer together with Earth-rotation synthesis can lead to a relatively simple set of equations for image deconvolution. This is not a safe assumption for the VLA, and hence the deconvolution algorithms are different for each telescope. Since this thesis only deals with VLA images which have already been deconvolved, such issues will not be described here.

2.4.1   Deconvolution

Equation 2.1 showed that there was a Fourier relationship between the source intensity and the measured visibilities. Section 2.3 showed that these visibilities are often corrupted, for which there are certain helpful remedies. However, one assumption that was ignored was the discretisation of the signal from the interferometer. Since the measured visibility is only a finite number of noisy samples, the true sky intensity, $I_\nu(l, m)$ cannot be recovered directly: either a model or non-parametric approach must be used to estimate $I_\nu(l, m)$.

Since we are measuring discrete samples over the uv-plane , Equation 2.2 becomes:

$$\hat{V}(u, v) = \sum_{p=1}^{N_l} \sum_{q=1}^{N_m} \hat{I}(p\Delta l, q\Delta m)e^{-2\pi i(pu\Delta l + qv\Delta m)}. \tag{2.12}$$

Equation 2.12 represents a general purpose model $\hat{I}$ of the source intensity, and consists of a two-dimensional grid of δ-functions with strengths $\hat{I}(p\Delta l, q\Delta m)$, where Δl and Δm are the separations of the N_l and N_m grid elements.

Equation 2.12 can be seen to impose some limits on how the visibilities are deconvolved:

1. One can expect to estimate source features with widths ranging from $O(1/\max(u, v))$ up to $O(1/\min(u, v))$.

2. The grid spacings, Δl and Δm and the number of pixels on each axis, N_l and N_m must allow representations of all these scales.

3. The scale of the grid separations must satisfy $\Delta l \leq \frac{1}{2u_{max}}$, $\Delta m \leq \frac{1}{2v_{max}}$, where u_{max} and v_{max} are the maximum separation of the baselines in the uv-plane.

4. The cell densities must satisfy $N_l\Delta l \geq \frac{1}{u_{min}}$ and $N_m\Delta m \geq \frac{1}{v_{min}}$ where u_{min} and v_{min} are the minimum separation of the baselines in the uv-plane.

5. This model has $N_l N_m$ free parameters - the cell flux densities, $\hat{I}_{p,q}$.

To estimate the true sky brightness, image deconvolution is essentially a process of producing a plausible likeness to the true sky intensity, using a process which in the uv-plane can be thought of as an interpolation process to estimate intensities between measured values. There are two main algorithms with which to do this: CLEAN and maximum entropy methods (MEM) which are discussed below. In each case the algorithm is presented and followed with a discussion on the strengths and weaknesses of each.

2.4.2   The CLEAN algorithm

The CLEAN algorithm was first developed in 1974 by Högbom, and solves the deconvolution equation using the assumption that the true sky brightness can be represented by a number of point sources in an otherwise empty field. The final image, known as the CLEAN image, is the product of these point sources convolved with a beam (usually Gaussian). There are several variants of the initial (Hogbom) algorithm, of which the most widely used is the Clarke algorithm is set out below. The Clarke algorithm has a *major* and *minor* cycle, and makes best use of the relatively computationally inexpensive cost of the fast Fourier transform (FFT). A minor cycle consists of the following steps:

1. A beam patch (a segment of the discrete representation of the beam) is selected to include the highest exterior sidelobe. The synthesized beam can, in most cases, be

closely approximated by the Fourier transform of a circular disk function, known as an Airy disk (errors introduced because of this assumption are corrected in the major cycle). The first null is the synthesized beam, and the highest exterior sidelobe will be a subsequent peak.

2. Points are selected from the dirty image if they have an intensity, as a fraction of the image peak, which is greater than the highest exterior sidelobe of the beam.

3. A list-based Högbom CLEAN (see below) is performed using the beam patch and the selected points of the dirty image, which is ceased only if the point would not have been selected in step (2).

The major cycle is then instigated, which consists of the following steps:

1. The model of point sources found in the minor cycle undergoes an FFT.

2. This map is then multiplied by the weighted sampling function (which is derived from the inverse Fourier transform of the dirty beam).

3. Finally, the map (point source model multiplied by the sampling function) is transformed back and subtracted from the dirty map.

The list-based Högbom CLEAN in step (3) of the minor cycle consists of searching through the dirty map, pixel by pixel, and listing the strength and position of the peaks. At the position of each peak in the dirty map, the beam patch, multiplied by the peak strength and *loop gain* is subtracted (a typical loop gain is ∼ 0.1). The subtracted point source is then placed in the model image.

The CLEAN algorithm is the most popular algorithm because it is computationally inexpensive, however theoretical understanding of the algorithm is poor: no one has yet succeeded in producing a noise analysis of the CLEAN algorithm. Additionally, the major instability of the CLEAN algorithm is its tendency to introduce modulations at spatial frequencies corresponding to the unsampled parts of the uv-plane, known as ripples. These ripples show up as (clearly unphysical in total intensity maps) negative bowls in the image after the residuals are convolved with the CLEAN beam.

2.4.3   The maximum entropy method

Whilst the use of one of the CLEAN algorithms, such as the Clarke algorithm is procedural, the Maximum Entropy Method (MEM) is not. Essentially the image is selected by fitting to the data, within an acceptable noise limit, whilst having maximum *entropy*. Entropy in this case, is defined (See TCP99, Lecture 8) as 'something which when maximised, produces a positive image with a compressed range in pixel values.' One of the most general forms of this 'entropy' constraint is:

$$H = -\sum_k I_k \ln \frac{I_k}{M_k e}, \tag{2.13}$$

where I_k is the model source intensity, M_k is a "default" image incorporated to allow *a priori* knowledge to be used and e is the peak amplitude of the default image. Since the enforcement of positivity is usually incompatible with fitting the measured visibility exactly, it is common practice to fit the predicted visibility to observed, is close to the expected

value (in a χ^2 sense):

$$\chi^2 = \sum_k \frac{|V(u_k, v_k - \widehat{V(u_k, v_k)}|^2}{\sigma^2_{V(u_k, v_k)}}.$$

(2.14)

This system has its drawbacks too: it tends to lead to an image which fits the long spacings too well, and the short spacings very poorly. It is thought that the reason is related to the fact that the entropy condition is insensitive to spatial information. It can be overcome to some degree by providing an estimate of the zero-spacing flux density (c.f. Section 2.5.3).

As was seen above, each of the respective methods good and bad points, both have drawbacks in certain imaging situations. CLEAN is unsuited to extended emission, and may introduce coherent (and false) structure, such as striping, or rings. MEM on the other hand, deals poorly with point sources within extended structure (due to the smoothing which is built into the method). Both, however, are excellent for simple and isolated sources.

2.4.4 Image restoration

Both methods produce what is known as a *clean component model* (also known as a clean table) having units of Jy/pixel. To make a "cleaned" image, a residual map is created by subtracting the clean component model convolved with the dirty beam from the original dirty image. The clean, or *restored* image is then the residual map plus the clean component model convolved with the clean beam.

2.5 Use of ATCA for flux density mapping of large areas

TheATCA is an earth-rotation aperture synthesis interferometer, consisting of six 22-m antennae on an east-west track, with a maximum baseline of 6 km. The ATCA operates in seven frequency ranges: 1.2-1.7, 2.2-2.6, 4.2-6.7, 8.0-9.1, 16.0-25.0, 30.0-50.0 and 84.0-105.0 GHz. The ATCA has a number of advantages for the mapping of large areas and for sensitive flux density measurements.

2.5.1 Sensitivity

Being an interferometer, the ATCA enables very high signal-to-noise flux density measurements. The rms flux sensitivity of the ATCA, ΔS_{rms} is given by:

$$\Delta S_{rms} = \frac{0.0195 S_{sys}}{\sqrt{tB}} \text{ mJy},$$

(2.15)

where t is the integration time in minutes, B is the bandwidth in MHz, and S_{sys} is the system sensitivity. S_{sys} is defined as the signal which doubles the system temperature at an elevation of $40°$ and is dependent on observing frequency, but at centimeter wavelengths is ~ 400 Jy. Equation 2.15 shows that using a typical correlator setup of 128 MHz bandwidth, a 1 minute "snapshot" observation gives a theoretical rms noise of < 1 mJy.

2.5.2 Mosaicing

Traditionally it was thought that interferometry was best applied to sensitive, high resolution of smaller sources, and single dish observations best for large sources. However *mosaic* observations, where an interferometer is pointed at many different pointing centers can

provide sensitive, high resolution images of large objects. This thesis focuses on one such example: a mosaic of the Galactic Centre region.

Mosaic imaging (mosaicing) is best used when the source size is larger than the primary beam (i.e., $\theta > \lambda/D$, where D is the diameter of the telescope in meters). Mosaicing can also be used when the source is large, compared to the reciprocal size of the shortest baseline (i.e., when $\theta > \lambda/b_{min}$, where b_{min} is the shortest baseline in meters), however the following discussion will focus on the first type.

The measurement equation can be written as:

$$V(\vec{u}) = \iint (A(\vec{x} - \vec{x}_p)I(\vec{x}))e^{-2\pi i(\vec{u}\cdot\vec{x})}d\vec{x}, \tag{2.16}$$

where $\vec{x}$ and $\vec{u}$ are two-dimensional vectors representing the sky and Fourier plane coordinates, and $\vec{x}_p$ is the pointing centre (note that the pointing centre is different from the phase centre and tracking center).

If the source is larger than the extent of $A(\vec{x} - \vec{x}_p)$, known as the *primary beam,* then flux density will be filtered out of the image in a process known as *spatial filtering.* More disastrously, the flux density outside will corrupt the visibilities *inside* the primary beam and degrade the image quality. Additionally, when dividing by the primary beam (known as *primary beam correction,* performed in order to negate the effect of the diminishing sensitivity of the telescope towards the edge of the FoV), the noise across the image becomes non-uniform, and can lead to an increase of a factor of 10 near the edge of the field.

The primary reason that mosaicing works, is that although "snapshot" observations produce poor images, a number of snapshots, regularly spaced over a large range of parallactic angles, will produce a good image. The reason is that what is important in high resolution and sensitivity observations is not large amounts of time (Equation 2.15 indicates that time only increases the rms noise as the inverse of the square-root of time), but rather coverage of the *uv*-plane. This result is born out of the sampling function, $S(u, v)$ in Equation 2.1: the more complete the sampling function, the more closely the dirty image represents the true sky visibility. Hence mosaicing, where pointing centers are cycled through during the observations provides high sensitivity, low noise images of large and complex structures.

Deconvolution of mosaic observations can proceed in several different ways. Firstly, the different pointings can be deconvolved (using the techniques outline above), and combined in a linear fashion:

$$I(\vec{x}) = \frac{\sum_p A(\vec{x} - \vec{x}_p)I_p(\vec{x})}{\sum_p A^2(\vec{x} - \vec{x}_p)}, \tag{2.17}$$

where the summation over p is over the pointings. If the number of pointings is equal to one, then Equation 2.17 is simply a division by the primary beam.

Alternatively Sault, Staverly-Smith and Brouw (1996) have developed an alternative mosaic algorithm, which is of a type known as joint deconvolution, since it attempts to deconvolve using information from every pointing. Since this algorithm is implemented in MIRIAD it is described here in some detail.

1. A linear combination of the dirty images from each pointing are linearly mosaiced, almost according to Equation 2.17. The difference is the use of an image plane weighting scheme which results in constant thermal noise across the image. The dirty beams from each pointing are kept in a cube for use in a deconvolution algorithm.

2. All the (u, v) data is used to find an image which is consistent with all the data, and (in a fashion similar to MEM deconvolution) optimises a global χ^2 goodness of fit:

$$\chi^2 = \sum_p \sum_i \frac{|V(\vec{u}_i, \vec{x}_p) - \hat{V}(\vec{u}_i, \vec{x}_p)|^2}{\sigma_V^2(\vec{u}_i, \vec{x}_p)}, \qquad (2.18)$$

where the summation is over all visibilities, i, in each pointing p and $\hat{V}$ is the model visibility calculated from Equation 2.12.

3. The gradient of χ^2 is then used with the non-linear deconvolution algorithm, MEM, in a joint fashion. The gradient has the form:

$$\nabla_{\hat{I}} \chi^2(\vec{x}) = -2 \sum_p A(\vec{x} - \vec{x}_p) \left(I_p^D(\vec{x}) - B_p(\vec{x}) * (A(\vec{x} - \vec{x}_p \hat{I}(\vec{x}))) \right), \qquad (2.19)$$

where $\hat{I}$ is the model image, the summation is over pointings p, $I_p^D(\vec{x})$ is the dirty map for the pth pointing, and $B_p(\vec{x})$ is the beam for that pointing. Equation 2.19 is simply an un-normalised version of Equation 2.17, and can be thought of as a mosaic of the residual images (which is the expression between the large parentheses) for each pointing.

4. The residual image is formed by multiplying the global model image by the primary beam, convolving with the dirty beam and then subtracting this from the dirty image. This is done iteratively, where the gradient should get smaller the closer to reality the image becomes (until it is simply a noise factor).

2.5.3 Including total power in mosaic observations

One important short-coming of radio interferometers is that they do not measure total power. This is simply because the largest scale an interferometer can measure is inversely proportional to the length of the shortest baseline, which is always longer than the diameter of the dish. A way to overcome this is to include the so-called *zero-spacing flux* by combining the interferometric data with a single dish map.

The best way to combine the data is to do so before deconvolution, so as to increase the amount of information about a source. Usually, the size of the single dish and interferometer dishes are different – as will be the case throughout this thesis – so that the relative sensitivities overlap. This is illustrated in Figure 2.4, where the relative sensitivities of the ATCA interferometer and Parkes radio telescope is shown as a function of *uv*-distance. *uv*-distance is the angular distance on the sky expressed as a function of the separation vector of the telescopes in an array – the greater the spatial frequency, the smaller the angular scale in the sky. Figure 2.4 shows that data from an interferometer and a single-dish observation can be combined in a way that gives sensitivity to all angular scales down to the resolution of the interferometer.

Given a mosaic of dirty interferometer images I_{int}^D, and a dirty beam B_{int}^D, and single dish image, I_{sd}^D with beam B_{sd}^D, the composite dirty images and beams are formed as:

$$I_{comp}^D = \frac{I_{int}^D + \alpha I_{sd}^D}{(1 + \alpha)} \qquad (2.20)$$

$$B_{comp}^D = \frac{B_{int}^D + \alpha B_{sd}^D}{(1 + \alpha)}, \qquad (2.21)$$

where α is a constant which will be discussed below. Combined in this way provides a convolution relationship between the true sky brightness distribution I and the composite dirty image and beam:

$$I^D_{comp} = I * B^D_{comp}. \tag{2.22}$$

The use of α in Equations 2.20 and 2.21 is of some debate, however, there are two schools of thought: that α be equal to the ratio of the beam areas of the two telescopes, or that α be the ratio of the two sensitivities of the two dishes.
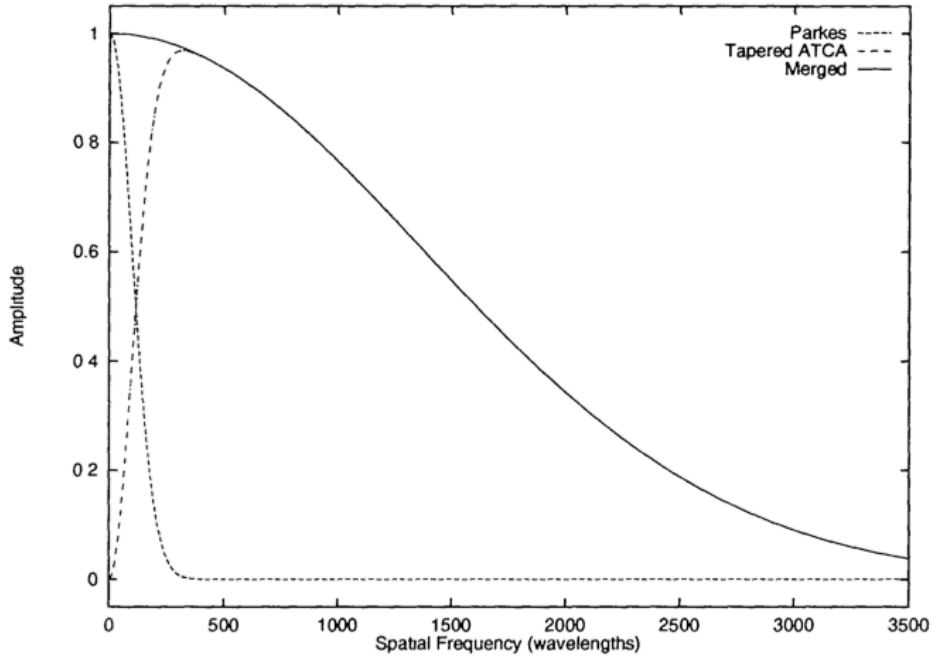
Figure 2.4: The tapering of spatial frequencies by a single-dish (dashed), by an interferometer (dot-dash) and merged (solid) using the ATCA and Parkes as the interferometer and single-dish respectively. From Sault & Kileen (1998) after Stanimirovic (2002).

In MIRIAD, α is the keyword *factor*, and is described as 'the factor to scale the low resolution image to put it on the same flux scale as the high resolution image'. This is done in the Fourier plane for data which is well represented by both images (i.e., where the dish sizes overlap - for the case of ATCA and Parkes data, this would be somewhere in between 22 meters of the ATCA dishes and 64 meters of the Parkes dish, as represented in the Fourier plane). It should be noted then, that α depends on the absolute calibration accuracy of *both* data sets.

2.5.4 Polarisation

The ATCA uses on-axis orthogonally polarised linear feeds, allowing a complete description of the polarised state of the incident radiation. It is convention in astronomy to describe the state of a radiation field in terms the Stokes parameters. There are four Stokes parameters; I, Q, U and V, where I represents the total intensity, the sum of all polarisation states. Q and U describe the linear polarisation component, and V the circular component. Linear polarisation is usually described in terms of the polarised flux density, p, and the position

angle of the electric vector of linear polarisation, ψ, such that:

$$p = \sqrt{Q^2 + U^2} \tag{2.23}$$

$$\psi = \frac{1}{2}\arctan\left(\frac{U}{Q}\right) \tag{2.24}$$

Operationally, telescopes with altitude-azimuth (*alt-az*) mounts, four ideally linearly polarised products, (X, Y), corresponding to the cross-correlations between the feeds on two antennae, can be converted to Stokes parameters using the following equations (see, for example, Sault, et al. 1991):

$$I = \frac{1}{2}(XX + YY) \tag{2.25}$$

$$Q = \frac{1}{2}[(XX - YY)\cos(2\chi) - (XY + YX)\sin(2\chi)] \tag{2.26}$$

$$U = \frac{1}{2}[(XX - YY)\sin(2\chi) - (XY + YX)\cos(2\chi)] \tag{2.27}$$

$$V = \frac{1}{2}i(YX - XY) \tag{2.28}$$

where χ is the parallactic angle. The parallactic angle is defined as:

$$\chi = \arctan\left(\frac{\cos(L)\sin(h)}{\sin(L)\cos(\delta) - \cos(L)\sin(\delta)\cos(h)}\right) \tag{2.29}$$

where δ is the source declination, L is the geodetic latitude of the antenna, and h is the source hour angle. As the Earth rotates, the feed also rotates with respect to the source, which for the ATCA, the X feed is offset by $45°$ from Celestial North at transit, so that the parallactic angle has to be offset by that amount.

There are two reasons why linear polarisation feeds are an advantage for alt-az telescopes, such as the ATCA. Firstly, observing a single calibration source across the sky and several different parallactic angles, it is possible to to decouple the leakages and the calibrator's linear polarisation, meaning that the polarisation characteristics of the calibrator need not be known *a priori*. Secondly, polarimetric calibration requires solving the time-dependent complex antenna gains, and to know the phase difference between X and Y polarisation channels. These can both be performed using the on-line ATCA noise-diode system.

2.6 Summary

This section has provided an overview of the major concepts in the imaging of sources with radio telescopes and interferometers in particular. Careful attention has been paid to issues of image deconvolution algorithms, mosaicing and the addition of total power measurements to images, upon which much of the data presented in this thesis is based.

3

Fundamentals of ground-based γ-ray astronomy

3.1 Introduction

As alluded to in Chapter 1, much of this thesis investigates regions in which γ-rays have been observed or, through the observation of radio emission, could potentially be a source of γ-rays . Recent developments in instrumentation of γ-ray telescopes in the past ten-or-so years, has revealed these sources at arcminute resolution and propelled γ-ray astronomy into a mature observational science. Here we outline the basic principles of VHE γ-ray telescopes ($E \gtrsim 0.1$ TeV), paying particular attention to the imaging atmospheric Cherenkov telescope (IACT) method which is by far the most successful way of observing VHE γ-ray sources. A more detailed discussion of the topic – and from where most of this discussion is derived – can be found in Chapters 4, 5 and 7 of Longair (1994). The excellent article by Völk & Bernlör (2008) contains a discussion of IACT astronomy issues on which some of this discussion is based.

3.1.1 Electromagnetic and hadronic air showers

When a cosmic or γ-ray intersects the atmosphere of the earth, it sets off a shower of secondary particles, as the primary (and all subsequently produced) particles interact with the nuclei in the atmosphere, in what is known as an *air-shower*. An air-shower can have two different components, an electromagnetic and a hadronic component. γ-rays will initiate an electromagnetic shower, whereas a cosmic ray will initiate both electromagnetic and hadronic showers.

Electromagnetic showers

An electromagnetic shower develops because of two processes: bremsstrahlung and pair production. When a γ-ray impinges on the earth's atmosphere, it can pair produce in the Coulomb field of atomic nuclei. These electrons and positrons are then deflected by the nuclei (in opposite directions), producing photons via bremsstrahlung. These photons then pair produce, and a cascading effect results. This is shown diagrammatically in Figure 3.1 in a simple model first developed by Heitler (1954).

Figure 3.1 shows that an incoming particle of energy E_0, interacts at an atmospheric depth of $x = X_0$, where X_0 is the mean free path of the γ-ray in the atmosphere. The simplifying assumption is made that producing an electron/positron pair, each particle will have equal energy, i.e., $E_0/2$. Because the radiation lengths of pair production and bremsstrahlung are equal in the ultra-relativistic limit, the electron/positron pair will each create a photon of energy $E_0/4$ at an atmospheric depth of $x = 2X_0$. The number
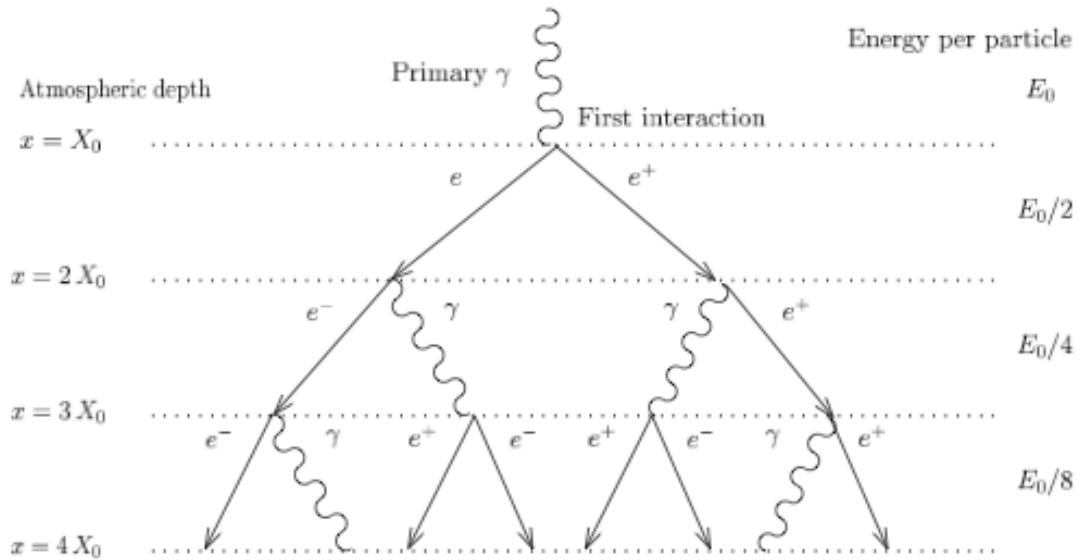
Figure 3.1: A simple model describing the development of an electromagnetic air shower, according to Heitler.

of particles (electrons + positrons + photons) in the shower increases until it reaches a maximum when the mean particle energy drops below the critical energy, $E_c \approx 80$ MeV in air. This corresponds to the energy at which for electrons, ionization losses becomes the dominant loss process. For γ-rays created below the critical energy, Compton scattering and photoelectric absorption becomes the dominant loss process.

It can easily be seen that after $n = x/X_0$ branchings (where x is the distance traveled along the shower axis, in units of g cm^{-2}), the shower consists of $N(x) = 2^n = 2^{x/X_0}$ particles. These particles each have energy $E(x) = E_0 2^{-x/X_0}$, from which we can obtain the depth, in the atmosphere, of the shower maximum, known as X_{max}:

$$E_0 2^{-X_{max}/X_0} = E_c \tag{3.1}$$

$$\Rightarrow X_{max} = \frac{\ln(E_0/E_c)}{\ln 2} X_0 \tag{3.2}$$

Hence the maximum number of particles produced in an electromagnetic shower is:

$$N_{max} = 2^{X_{max}/X_0} = \frac{E_0}{E_c}. \tag{3.3}$$

This shows that the number of particles in the shower is proportional to the initial energy of the primary γ-ray . A 1 TeV shower will create an air shower of $\sim 1.25 \times 10^4$ particles and attain a maximum at about 300 g cm^{-2}, which is approximately 10 km above sea level. Comparing the model presented above in Figure 3.1 with Figure 3.2, which shows showers derived from Monte Carlo simulations which take into account more complicated physics, it is obvious that the Heitler model is quite a simple model.

Hadronic showers

Hadronic showers are similar to electromagnetic showers. However, since hadronic showers are initiated by protons, or heavier nuclei, they produce particles such as nucleons, pions and kaons, which are absent in electromagnetic showers. Thus hadronic showers have two components: an electromagnetic component derived from γ-rays , electrons and positrons

naturally produced in the shower; and a hadronic component, where nuclei spallate (i.e., expel protons and neutrons). Figure 3.2 illustrates that hadronic showers are less regular than electromagnetic ones, and due to different interaction mechanisms and mean free path lengths, develop later and are wider than electromagnetic showers.
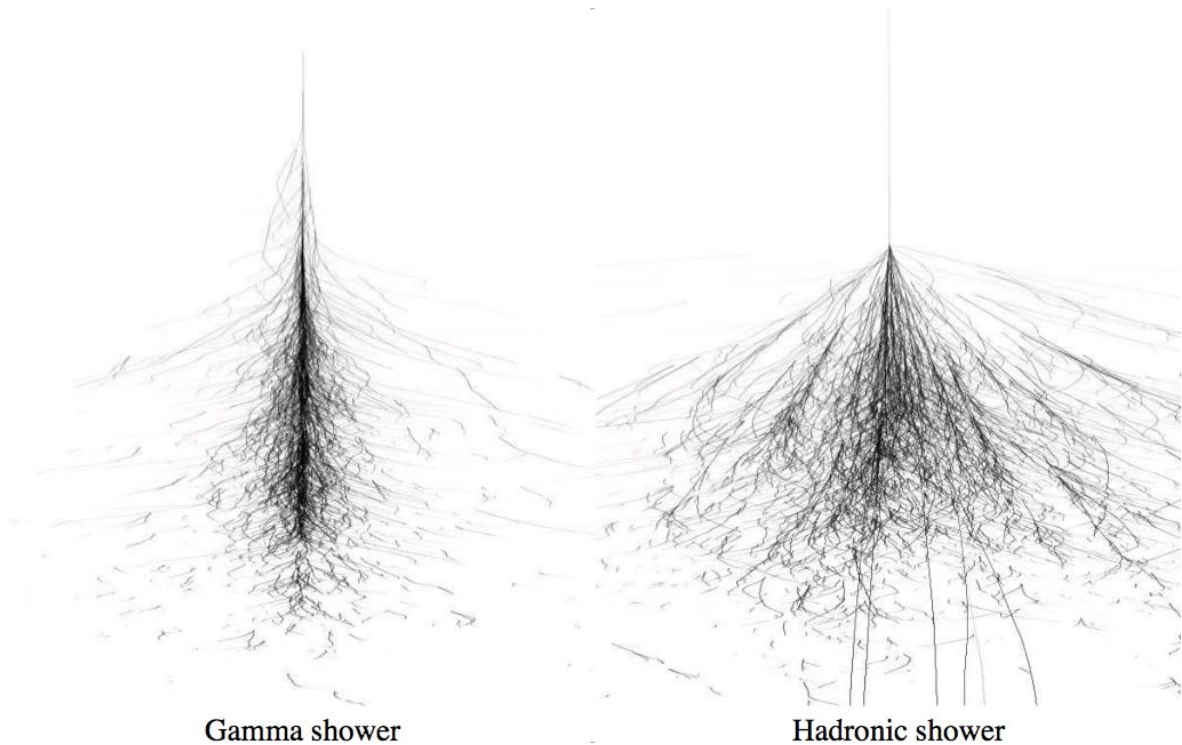

Gamma shower   Hadronic shower

Figure 3.2: Illustration of the difference between an electromagnetic air shower (left) and hadronic air showers (right). From Völk & Bernlör (2008).

3.2 Cherenkov Radiation

When a particle, traveling through a medium, possesses a velocity which is greater than the speed-of-light of the medium, the particle will emit *Cherenkov* radiation. In this section, we briefly outline the main characteristics of this phenomenon as is important to the detection of VHE γ-rays with IACT detectors such as HESS.

Figure 3.3 sets out a simple geometric picture of the production of Cherenkov photons, which is described, by analogy, as the particle creating a "shock-wave" as it moves through the medium with a velocity of $v > c/n$, where c is the speed of light in a vacuum and n is the refractive index of the ambient medium. Thus the majority of Cherenkov radiation is emitted at an angle of $\cos \alpha = c/nv$, where – as defined in Figure 3.3 – α is the angle between the wave vector and the direction of motion of the particle (denoted by the red arrow in Figure 3.3).

The fact that Cherenkov radiation is only emitted if $v > c/n$ allows this phenomenon to be used in threshold detectors by which different energies can be probed using different detector materials. The most important relationship however, is that the intensity of Cherenkov radiation is proportional to the frequency, ω of the emitted photons (Longair, 1994):

$$I(\omega) = \frac{\omega e^2 v}{4\pi\epsilon_0 c^3} \left(1 - \frac{c^2}{n^2 v^2}\right), \tag{3.4}$$
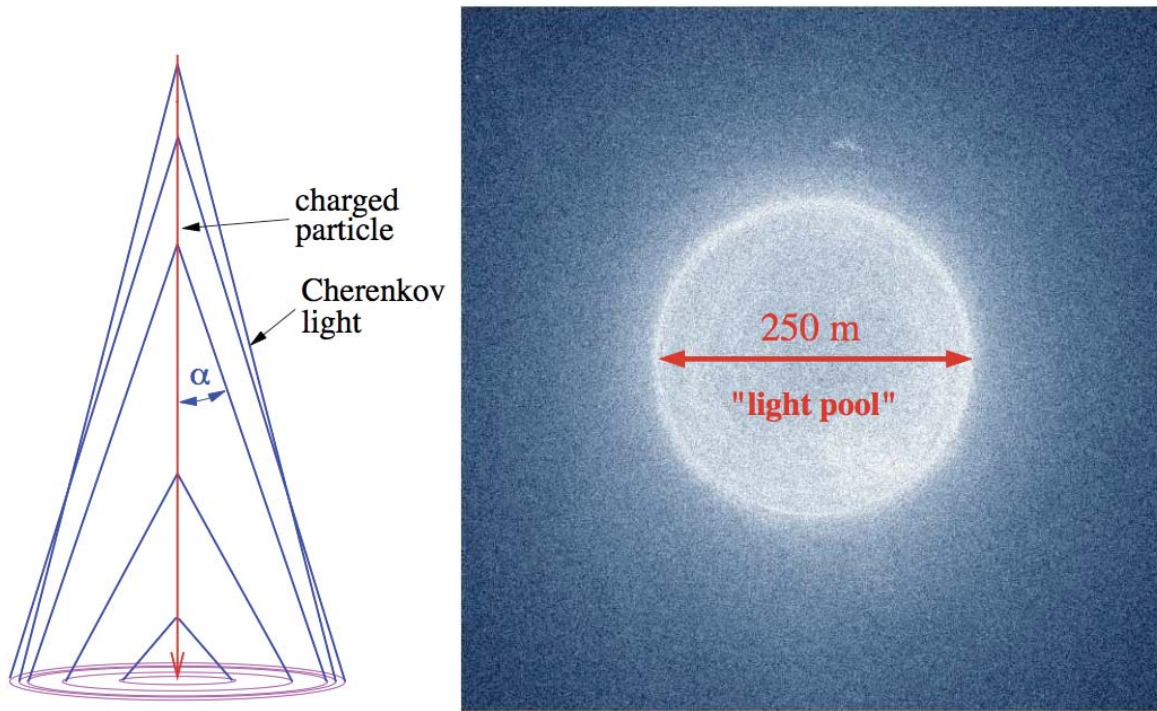
Figure 3.3: (*Left*): The geometry of Cherenkov radiation illustrates the geometry of Cherenkov radiation from a single charged particle. (*Right*): Shows the observation of Cherenkov light from a shower induced by a γ-ray of 1 TeV (Völk & Bernlör, 2008).

where e is the charge of the electron, and ϵ_0 is the permittivity of free-space. Thus, if the index of refraction in the absorbing medium is known (say, in the atmosphere), then by counting the number of Cherenkov photons from an electromagnetic shower, information about the energy of the initial photon energy can be obtained.

3.3   Imaging atmospheric Cherenkov technique (IACT)

Whilst direct detection by space borne detection at energies up to 10 GeV is possible (EGRET for example; c.f. Figure 3.6), the limited size of the collecting area has necessarily led to the development of earth based, indirect measurement techniques for higher energies. In the previous section, we outlined the process by which Cherenkov photons are created. This can be used to search the atmosphere for Cherenkov photons which are produced when electromagnetic showers are created from γ-rays intersecting the top of the earth's atmosphere. This technique is known as the Imaging Atmospheric Cherenkov Technique (IACT) and has been developed to great effect in the past 20 years to the state where high sensitivity, arcminute resolution VHE γ-ray astronomy is now routine.

The general properties of electromagnetic showers and Cherenkov radiation presented above for a 300 GeV γ-ray lead to several million photons creating a short-duration pulse of $\sim$ 10 ns duration at sea-level about a cone of opening angle of $1 - 2°$. IACT telescopes are then used to search for these Cherenkov photons, emitted at a wavelength of $\sim$ 300 nm extending over an area of $\sim$ 100 m.

3.3.1 Basic IACT Geometry

In contrast to the Fourier relationship between the sky and *uv*-plane in radio astronomy presented in Chapter 2, the geometry of the collection of Cherenkov light is relatively straighforward. Figure 3.4 shows that points 1, 2 and 3 fall in a line of an EM shower initiated by a γ-ray . These are then represented in the plane of the telescope, using sky coordinates (x, y, z) according to the relationship:

$$\begin{pmatrix} u \\ v \end{pmatrix} = -\frac{f}{z} \begin{pmatrix} x \\ y \end{pmatrix},$$
(3.5)

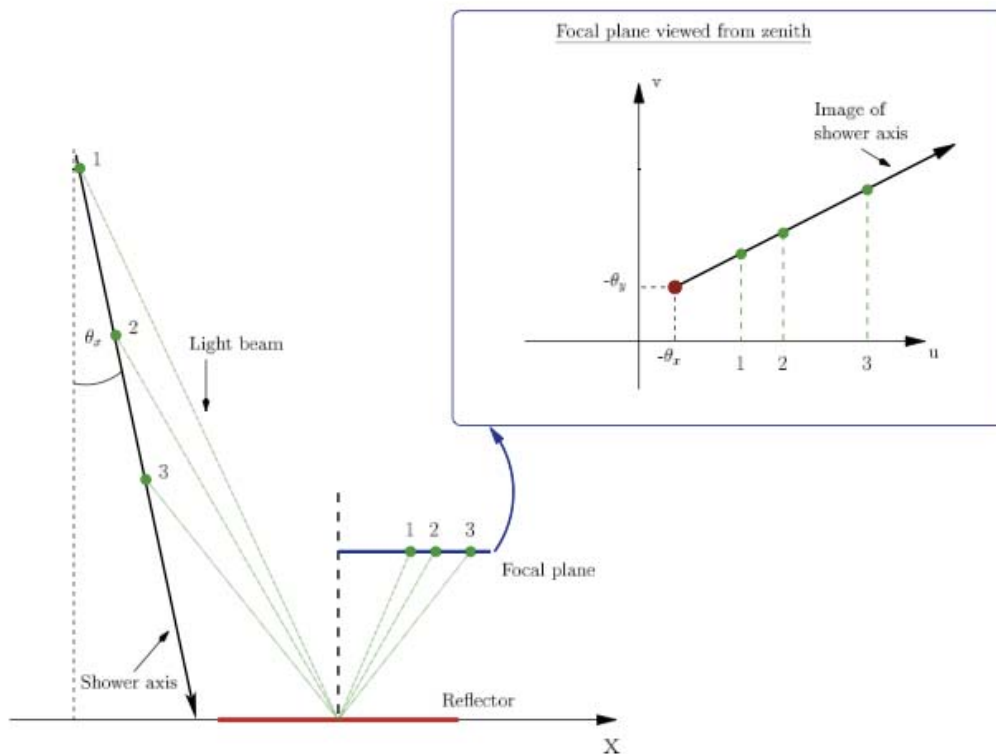where f is the focal length of the camera (and for HESS is 15m).

Figure 3.4: The geometry of Cherenkov light collection. This illustrates the simple mapping of the light from the sky plane onto the camera plane. It can be seen from this geometry that the orientation of the image in the camera plane is dependent on the inclination of the shower with respect to the telescope optical axis.

Given the simple geometry of the telescope system, and the properties of the Cherenkov pulse, the use of a number of telescopes, spread out over ~ 100 m can be used to generate images of astrophysical γ-ray sources with arcminute resolution.

3.3.2 Sources of systematic uncertainty in IACT telescopes

The atmosphere

Whilst the atmosphere essentially acts as a calorimeter where the incoming γ-ray deposits its energy, the flux of Cherenkov photons at sea level is affected by the conditions of the atmosphere. The main effects are the change in density of the atmosphere as a function of height, scattering of Cherenkov photons, absorption by molecules of Ozone, and the background due to night sky photons and we briefly discuss each in turn.

1. The changing density of the atmosphere will affect the intensity and opening angle of the Cherenkov light cone by changing the refractive index of the air. This is overcome by the development of sophisticated models of how the density of the atmosphere changes as a function of height.

2. Scattering processes in the atmosphere work to decrease the intensity of the Cherenkov light. The main types are the usual Mie and Rayleigh scattering, which result in the scattering of (Cherenkov) photons on particles whose dimensions are similar to (Mie), and smaller than (Rayleigh), the wavelength of the photon.

3. Cherenkov light can be absorbed by Ozone in the atmosphere according to $O_3 + \gamma \rightarrow O_2 + O$, so that the intensity of photons at ground level may be reduced.

4. The sky on a moonless night is not completely dark, and so the flux of Cherenkov photons has to be distinguished above background night sky photons at a level of 7×10^{11} photons m^{-2} s^{-1} sr^{-1} (Longair, 1994). However, the fact that most light from an air shower pulse is of $\sim$ 10 ns duration, the night sky background can be effectively suppressed (Völk & Bernlör, 2008).

CR background

As was discussed in Section 3.1.1, protons and heavier nuclei from CRs can also induce electromagnetic showers in the upper atmosphere. Hence, any ground based γ-ray detector must be able to distinguish between the electromagnetic showers initiated by γ-rays and those due to CRs. In practice, CR induced Cherenkov profiles are distinguished because of the production of pions and other particles at large angles to the core of the shower, which produce a Cherenkov profile that is wider than that generated by γ-rays , as evidenced in Figure 3.2.

3.3.3   Single dish IACTs: The Whipple Observatory

In the middle of the 1980s, the Whipple Observatory provided the first unambiguous (9σ after about 60 hours of observation; Weekes, et al 1989) detection of an astrophysical VHE γ-ray source. The Whipple observatory consisted of a single 10 m optical reflector and so suffered a number of problems which prevented the detection of more sources, as we now explain. Figure 3.5 shows an image in the camera plane for a 1 TeV γ-ray shower, and illustrates the long, almost elliptical shape of the shower in the telescope plane, which can be $\sim$ 1° (Völk & Bernlör, 2008). Thus the field-of-view of the telescope is critically important, and because single dish IACTs at this time had large pixel sizes and a relatively smaller collecting area, the sensitivity was necessarily lower (than for modern IACTs; c.f. Figure 3.6). Furthermore, single telescopes have only one projection of the shower, making the shower direction lie somewhere on the line delineating the major axis of the shower image (Völk & Bernlör, 2008) and confining the analysis of any events to a 2-dimensional plane.

     Perhaps the biggest problem for single dish IACTs such as Whipple however, is the rejection at low energies (i.e. near the threshold energy of the detector) of muons produced in hadronic showers that reach the telescope. For a muon that is produced in a (hadronic) shower directly overhead of a telescope, the resulting image is a circular distribution. However, if the muon is produced by a shower on the periphery of the telescope, then just a segment of this circle is observed, resulting in an image in the telescope plane, which can
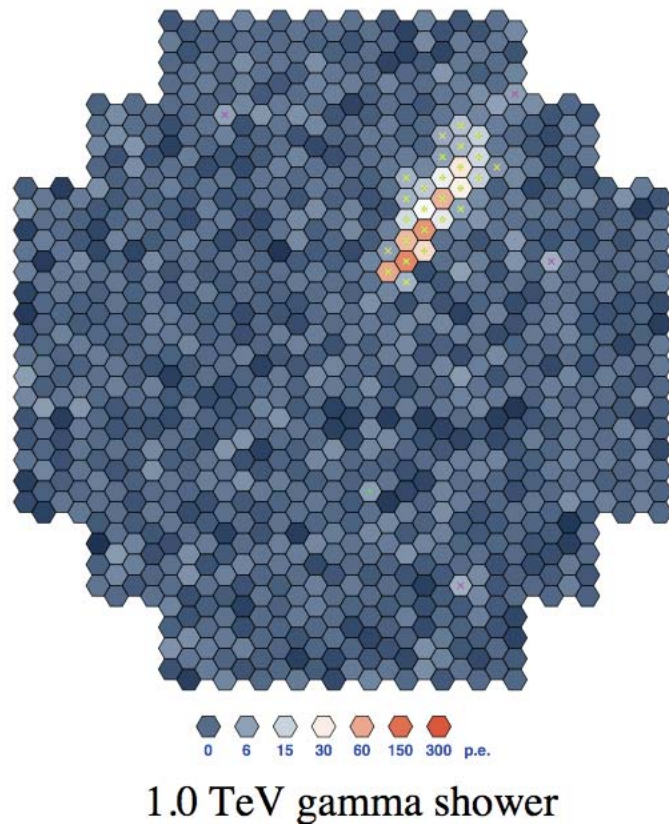
Figure 3.5: Camera plane image of a 1 TeV γ-ray shower (from Völk & Bernlör 2008).

be similar to a γ-ray shower. This makes the rejection of muon events difficult for single dish IACTs: the solution is to have multiple dishes, or stereoscopic IACTs.

3.3.4 Stereoscopic IACTs

As prefaced above, VHE γ-ray astronomy matured when a number (e.g., HESS, CANGAROO, HEGRA, VERITAS) of stereoscopic IACTs began operation just over a decade ago. These instruments are the culmination of a number of improvements over the early, single dish IACTs such as Whipple, described above. Specifically (and not directly due to the stereo-scopic method), these instruments contain a greater number of photo-multipliers in the cameras and a wider field-of-view so that great improvements in sensitivity, background rejection, angular and energy resolution have been achieved with the stereoscopic method.

Figure 3.6 shows the sensitivities for most VHE γ-ray experiments, including Whipple and HESS and shows that the latter is almost two orders-of-magnitude more sensitive at ~ 1 TeV. This is due to the stereoscopic nature of the telescopes and an example of a image reconstruction is shown in Figure 3.7. Stereoscopic IACTs locate the position of the primary γ-ray by the intersection of the major axes of the individual showers in each camera. This allows a greater rejection of the background because events such as the muons described in the previous section are localised in a single telescope. Thus if a trigger system is implemented (i.e., an event is only recorded if it is observed by more than a single telescope), then a greater number of background events can be filtered out than for a single telescope system. Additionally, because the shower is observed in more than one camera, then a 3-dimensional reconstruction of the show can be undertaken, leading to a greater accuracy in the reconstruction of the initial energy of the γ-ray (since the atmosphere is

NOTE:
This figure is included on page 40 of the print copy of
the thesis held in the University of Adelaide Library.

Figure 3.6: Integral flux sensitivity for various γ-ray detectors as a function of energy.
Note the large gain in sensitivity between the Whipple and HESS insruments. Sourced
from `http://statistics.roma2.infn.it/~agile/sensitivities01_07.jpg`

acting as a calorimeter).

The HESS telescope system

The High Energy Stereoscopic System (HESS), shown in Figure 3.8, is an array of telescopes located in Namibia in Africa (23°16′ S 16°30′ E at an altitude of 1800 m), which employs the IACT system to make high accuracy and resolution images of VHE γ-ray sources. It consists of four 13.6 m diameter altitude-aziumuth (alt-az) mount Davies-Cotton reflector telescopes arranged in a (static) square of length 120 m.

The Cherenkov light is collected using 382 mirror segments mounted on the 13.6 m hexagonal dish. The light is then focused onto an array of 960 individual photo-multiplier tube (PMTs) pixels, which subtend 0°.16 each. The PMTs sample at 1 GHz, and the signal is integrated for 16 nanoseconds. Upon receiving a trigger, the signal is stored and sent to a central trigger system. This allows the system to trigger only when two or more individual telescopes are triggered and improves the accuracy of both the estimate of the original energy of the particle, but also the positional accuracy of the detector (which is accurate to about 30″).

3.4   Summary

This chapter has summarized the main aspects of electromagnetic shows and Cherenkov radiation. Particular attention has been paid to the case where electromagnetic showers are instigated by γ-rays or CR impinging on the earth's atmosphere leading to a short-duration
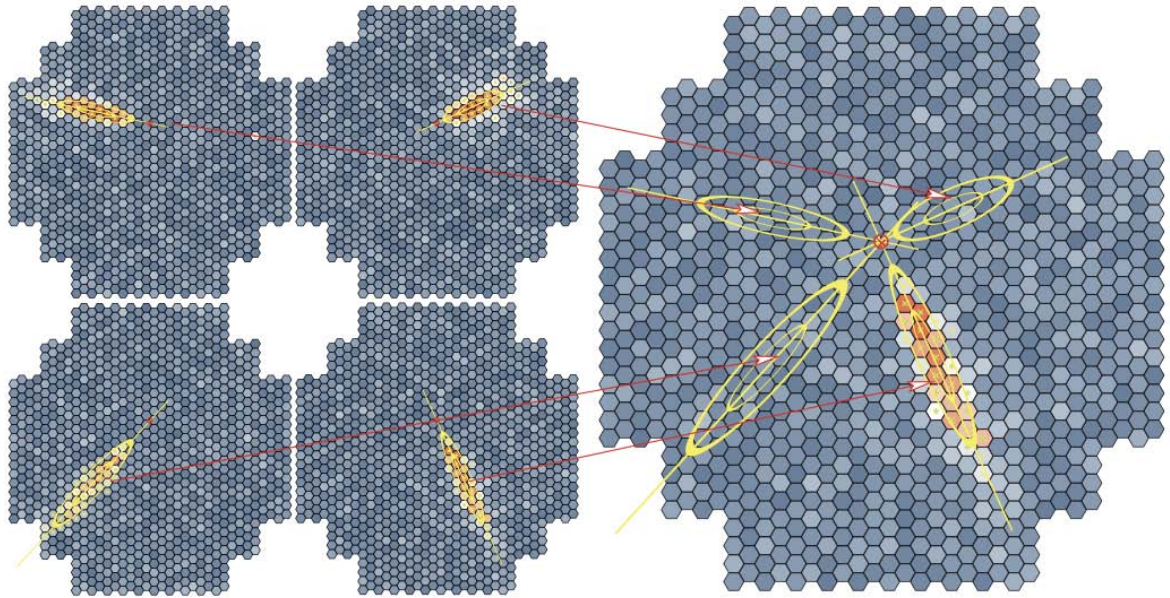
Figure 3.7: The projection of γ-ray showers as seen by four telescopes in a stereoscopic IACT, such as HESS onto a single camera plane providing greater event localisation; (Völk & Bernlör, 2008).

Figure 3.8: The HESS γ-ray telescope

pulse of Cherenkov photons. This chapter has also outlined the most successful method by which VHE γ-ray astronomy can be carried out: IACTs. The two types of IACTs, single-dish and stereoscopic telescopes were presented and their advantages and disadvantages were discussed. The specific case of HESS whose data were employed in this thesis, was presented.

Particle acceleration and cooling mechanisms

<div style="text-align: right">4</div>

4.1 Introduction

This thesis uses a simple model of the production of secondary electrons (and positrons) due to CR interactions with ambient matter. In this chapter, we present the details of this model along with the theory of particle acceleration and loss processes which are important for particles at GeV–TeV energies. This chapter is based on chapters 1 and 5 of Rybicki & Lightman (1979), Chapters 18 and 19 of Longair (1994) and from notes from an honours level subject taught at the University of Adelaide by R.J. Protheroe.

This chapter is set out as follows. Firstly we describe the two main acceleration mechanisms which are widely believed to be operating within particle accelerators such as SNRs (c.f. Chapter 1): first and second order Fermi acceleration. Secondly, we describe the main pathways for these particles to lose energy: ionization, bremsstrahlung, blackbody emission, inverse Compton scattering and synchrotron cooling. Synchrotron losses from electrons can be either from primarily accelerated electrons or – as is lastly presented in this chapter – from secondary electrons and positrons which are created by nucleonic interactions with ambient matter. This secondary model is presented in terms of a one-zone static model, which is then applied throughout the remainder of this thesis.

4.2 Particle acceleration

There has been a considerable body of work built up concerning particle acceleration and it is beyond the scope of this thesis to go into much detail here. However, here we give a brief outline of the two major types of particle acceleration which are collectively known as Fermi acceleration.

4.2.1 2nd order Fermi acceleration

Enrico Fermi (Fermi, 1949) originally proposed that CRs are accelerated via the movement of the magnetic field in regions such as molecular clouds. It is thought that the ionization fraction of clouds is high enough so that the magnetic field lines are tied to the molecular matter. Particles will gain energy by scattering off (magnetic) irregularities in the cloud under the assumption that the cloud is 'collisionless' (because the densities ($\sim 10^4$ cm^{-3}) are small and so the cross-section for direct particle interaction is small; in this sense, the collisions within the cloud are said to be elastic). The scattering of the CRs, then, is by the magnetic field, which is tied to the (partly) ionised cloud, and thus to the cloud as a whole.

For an ultra-relativistic particle of energy E_1 entering a cloud, its energy in the cloud frame (primed) is:

$$E_1' = \gamma_c E_1 (1 - \beta_c \cos \theta_1), \qquad (4.1)$$

where $\beta_c = V/c$, $\gamma_c = 1/\sqrt{1 - \beta_c^2}$ is the Lorentz factor and $\cos \theta_1$ is the angle between the particle and the direction of the velocity of the cloud. After the particle is scattered within the cloud and leaves, its energy in the laboratory frame, E_2 is given by:

$$E_2 = \gamma_c E_2' (1 + \beta_c \cos \theta_2'), \qquad (4.2)$$

where θ_2' is the angle between the particle and the direction of the velocity of the cloud in the cloud frame and E_2' is the energy of the particle after leaving the cloud in the cloud frame and is simply the Lorentz transform of E_2. Averaging over all possible angles for an isotropic distribution of CRs, one finds that $\langle \cos \theta_1 \rangle = -\beta_c/3$ so that the average energy change, $(E_2 - E_1)/E$, is given by $\langle \Delta E \rangle / E \sim 4\beta_c^2/3$, since the CR direction within the cloud is randomized so that $\langle \cos \theta_2' \rangle = 0$. This gives an average energy gain within the cloud which is positive, but only *second order*, and given that the matter has random motions of $V \sim 15 \text{ km s}^{-1}$, second-order Fermi acceleration is not very efficient.

4.2.2 Diffusive Shock Acceleration: 1st order Fermi Acceleration

The second-order nature of Fermi's original theory provided motivation for the modification in the 1970s to model particle acceleration in SNRs such that it is possible to get acceleration which is a first-order process. Fermi acceleration is based upon a simplified schematic of a supernova exploding into the surrounding ISM which is illustrated in Figure 4.1, and is known as *diffusive shock acceleration* (DSA).

NOTE:
This figure is included on page 44 of the print copy of
the thesis held in the University of Adelaide Library.

Figure 4.1: Idealized schematic for a supernova shock wave exploding into the surrounding ISM. Figure due to R.J. Protheroe, unpublished lecture notes.

Physically, SNRs are known to eject material (typically 1–2 $M_\odot$) at a speed of $\sim 10^4 \text{ km s}^{-1}$. The shock travels outward and since the sound speed of the ISM is much lower, the magnetic field before the shock is magnified. If the ISM is clumpy, it can be shown that for an average velocity of the shocked material, V_p; shock speed, V_s; and an isotropic distribution of CRs, $\langle \cos \theta_1 \rangle = -2/3$ and $\langle \cos \theta_2 \rangle = 2/3$ results in an average energy gain of $\langle \Delta E \rangle / E \sim 4\beta_p/3$. This gives an acceleration of particles which is *first order* in β_p and of greater magnitude (viz. 15 km s^{-1} for the average cloud velocity).

Energy spectrum for Fermi acceleration

The energy spectrum of particles can be derived by considering the probability of a CR encountering the shock more than once. It can be shown that the probability of a particle encountering the shock again is simply the difference of the total probability (i.e., 1) and the probability of a particle escaping to infinity (at which the probability of encountering the shock again is zero), which is $1 - V_S/c$. This results in an energy spectrum after k crossings of:

$$E = E_0 \left(1 + \frac{\Delta E}{E}\right)^k,$$
(4.3)

where E_0 is the initial energy of the CR. Transposing the above relation for k gives an integral spectrum for energies above E of:

$$\ln Q(> E) = A + \frac{\ln[1 - P(\text{esc.})]}{\ln(1 + \Delta E/E)} \ln(E/E_0) = B - \Gamma \ln E,$$
(4.4)

where $Q(> E)$ is the integral energy spectrum of particles above energy, E; $P(\text{esc.})$ is the probability of a particle escaping the shock; and A and B are constants. Γ is (after expanding the natural logarithms and taking the first order approximation, i.e., $\ln(1 + x) \approx x$) defined as:

$$\Gamma \sim \frac{P(\text{esc.})}{\Delta E/E} = \frac{V_S/c}{V_S/c} = 1,$$
(4.5)

and is only valid for "strong shocks". This gives the familiar differential spectral index of $Q(E) \propto E^{-2}$. It can immediately be seen that the CR spectral index for DSA does not match that observed at the top of Earth's atmosphere (viz. $Q(E) \propto E^{-2.75}$). This is expected, however, due to the energy dependence of CR diffusion in the Galaxy steepening the spectrum at higher energy.

4.3 Particle loss processes

4.3.1 Definition of terms and the equation of radiative transfer

Here we define the key terms used in radiative processes and the equation of radiative transfer, both of which are used extensively in this thesis. Throughout this discussion, we refer to the 'specific' measure of a quantity (i.e. flux), which has units of *per unit frequency*; the integral quantity can be derived by the integration of the specific quantity over a frequency range. Typical units are described in the square brackets where appropriate.

The specific intensity of radiation is defined as the amount of energy, dE over the frequency range $d\nu$, passing from an area dA through a solid angle $d\Omega$ in time dt:

$$I_\nu \equiv \frac{dE}{dA dt d\Omega d\nu} \ [\text{erg s}^{-1} \text{ cm}^{-2} \text{ sr}^{-1} \text{ Hz}^{-1}].$$
(4.6)

It can immediately be seen that because of energy conservation, the change in intensity along a ray in a vacuum is zero (i.e., $dI_\nu/ds = 0$). The specific intensity is related to the specific flux by integration over the appropriate solid angle:

$$F_\nu \equiv \int I_\nu \cos\theta d\Omega \ [\text{erg s}^{-1} \text{ cm}^{-2} \text{ Hz}^{-1}].$$
(4.7)

It is important to note that throughout this thesis, the unit of *flux density* is a Jansky and is defined as 10^{-23} erg s^{-1} cm^{-2} Hz^{-1}. Additionally, throughout this thesis, we refer to the

intensity in non-standard units of *Jy beam*$^{-1}$, where the solid angle $d\Omega$ is that subtended by the *beam* of a telescope, where the beam was defined in Chapter 2.

Although conservation of energy implies that the intensity along a ray does not change, it can interact with the surrounding environment so that energy is added or subtracted from it. To describe the addition of energy to a source of radiation traveling through matter, we define a *specific emission coefficient, j_ν*:

$$j_\nu \equiv \frac{dE}{dV d\Omega dt d\nu} \ [\text{erg s}^{-1} \ \text{cm}^{-3} \ \text{sr}^{-1} \ \text{Hz}^{-1}], \tag{4.8}$$

such that if the mass density of the matter is ρ then the *spontaneous emissivity, ϵ_ν* per unit mass, is:

$$j_\nu = \frac{\epsilon_\nu \rho}{4\pi} = \frac{dI_\nu}{ds} \tag{4.9}$$

for a ray of radiation cross section dA traveling through volume $dV = dAds$. It should be noted that the *specific emission coefficient* is generally – and will be throughout this thesis – simply referred to as the *emissivity*.

Alternatively, radiation traveling through matter can be absorbed, which is described as:

$$dI_\nu = -\alpha_\nu I_\nu ds, \tag{4.10}$$

where α_ν [cm^{-1}] is the absorption coefficient and is generally proportional to the product of the matter density and the area, dA, that the matter occupies. More information can be obtained by changing the variable of the absorption coefficient to the *optical depth, τ_ν* which is defined as the integral of the absorption coefficient over the line-of-sight:

$$\tau_\nu = \int_{s_0}^{s} \alpha_\nu(s')ds'. \tag{4.11}$$

It is important to note that a medium is *optically thick* if $\tau_\nu \gg 1$ and *optically thin* when $\tau_\nu \ll 1$. The physical interpretation of this is that for optically thick media, the average path length of a photon is much less than the size of the medium.

Thus the intensity of radiation as it travels through matter can be written as the sum of the emission and absorption of radiation, and is known as the equation of radiative transfer:

$$\frac{dI_\nu}{ds} = -\alpha_\nu I_\nu + j_\nu. \tag{4.12}$$

The important results from examining the solutions to this equation are:

1. If there is only emission ($\alpha_\nu = 0$), then the equation implies that the increase in brightness is just the integral of the emission coefficient over the line-of-sight.

2. If there is absorption only (i.e., $j_\nu = 0$), then the brightness decreases along the path as the exponential of the absorption coefficient integrated along the line-of-sight.

These are important results for radio and γ-ray astronomy since, if we do not posses any other information (such as about the relative velocities of the emission regions as can be obtained with spectral line observations), then all we can say is that the intensity of radiation observed is simply the emissivity integrated over the line of sight (i.e., we have no information about where the emission originated).

4.3.2 Thermal processes: thermal bremsstrahlung and blackbody emission

Blackbody emission

Blackbody emission occurs when particles at temperature T are in equilibrium. It is important to note a distinction between *blackbody emission*, and *thermal emission*: thermal emission occurs at any optical depth, blackbody emission, however, occurs when $\tau_\nu \gg 1$ at all frequencies and is described by the function $B_\nu(T)$ known as the *Planck Function*:

$$B_\nu(T) = \frac{2h\nu^3/c^2}{\exp(h\nu/kT) - 1}, \tag{4.13}$$

where h is Planck's constant, k is Boltzmann's constant, c is the speed of light, and T is the *brightness temperature*. There are two important results from Equation 4.13:

1. For frequencies where $h\nu << kT$, an expansion of the exponential gives a regime where $I_\nu \propto \nu^2$ and is known as the *Rayleigh-Jeans* part of the spectrum and is almost always true at radio frequencies. The Rayleigh-Jeans law also gives a simple expression for the brightness temperature of $T_b \equiv I_\nu \lambda^2/2k$, where λ is the wavelength.

2. For frequencies where $h\nu >> kT$, we have that $\exp(h\nu/kT) >> 1$ so that:

$$I_\nu = \frac{2h\nu^3}{c^2} \exp\left(\frac{-h\nu}{kT}\right). \tag{4.14}$$

   This regime is known as Wein's Law and is characterized by a steep drop in the intensity of emission.

Thermal bremsstrahlung emission

When, in the Coulomb field of a ion with charge Ze, an electron of charge e moves past an ion, the electron will be deflected and in the process, emit photons. If there is a continuous distribution of electrons with a thermal distribution of speeds, then photons with a continuous distribution will be emitted. The energies of these photons will, however, be governed by the fact that a photon cannot be created which has an energy greater than the electron energy (i.e., $h\nu \leq 1/2mv^2$). The spectrum of this emission will be determined by the charge of the ion, the temperature of the plasma, T, and the density of the ions, n_i and the electrons, n_e:

$$j_\nu = 6.8 \times 10^{-38} Z^2 n_i n_e T^{-1/2} e^{h\nu/kT} \bar{g}_{ff}, \tag{4.15}$$

where $\bar{g}_{ff}$ is known as the velocity-averaged Gaunt factor and takes into account various scattering properties of the medium. This emission gives rise, at sufficiently high frequency, to what is called 'optically thin' (thermal bremsstrahlung) emission, which turns over at low frequencies when the optical depth becomes greater than unity.

4.3.3 Energy losses of relativistic electrons

Ionization losses

Ionization losses occur when electrons have enough energy to ionize molecular material and are very important at lower energies energies (c.f. Figures 4.2 and 4.3). The loss rate for this process is:

$$\left(\frac{dE}{dt}\right)_i = 7.64 \times 10^{-15} \rho (3\ln(\gamma) + 19.8) \text{ [GeV s}^{-1}\text{]}, \tag{4.16}$$

where γ is the Lorentz factor and ρ is the particle mass density (in g cm^{-3}). As is explored in Chapter 8, the loss time determines, for a particular energy, which process is dominant, and is simply the energy divided by the loss rate:

$$t_l^i = \frac{E}{(dE/dt)_i} \propto \frac{E}{\rho \times \ln(\gamma)} \ [\text{s}]. \tag{4.17}$$

Thus, as is shown by the (solid) lines in Figures 4.2 the loss rate for ionization is independent of energy. Figure 4.3, on the other hand, shows that the loss time for ionization are proportional to $\ln(\gamma) \propto \ln(E)$ and becomes important at lower energies.
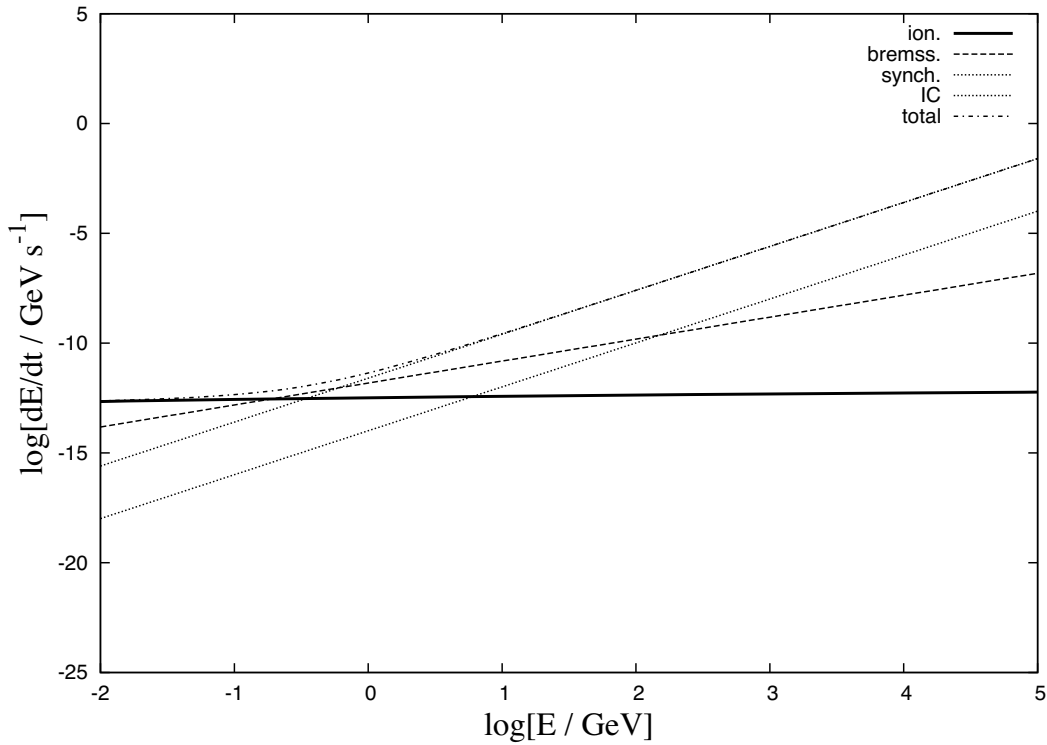

Figure 4.2: Loss rates (dE/dt) as a function of energy for ionization, bremsstrahlung, synchrotron and inverse Compton scattering as labelled and discussed in the text. The loss rates are for a density of $n_H = 10^3$ cm^{-3} , a magnetic field of (total) amplitude of $B = 1$ mG in a photon field energy density of $U_r = 1$ eV cm^{-3} .

Bremsstrahlung losses

Chapters 5 and 9 show that bremsstrahlung losses can play an important role in the separation from and spectral shape of synchrotron emission. These factors rely on the fact that the loss time for a relativistic electron of a photon due to a deflection by an ion is given by the density, n_H and the energy, E such that:

$$\left(\frac{dE}{dt}\right)_b = 3.66 \times 10^{-22} n_H E \ [\text{GeV s}^{-1}]. \tag{4.18}$$

This is shown in Figure 4.2 as the (dashed) line and shows that the loss rate is proportional to the energy. The loss time for Bremsstrahlung losses are then:

$$t_l^b = \left(\frac{E}{dE/dt}\right)_b \propto \frac{E}{n_H E} \propto n_H \text{ [s]},\tag{4.19}$$

which shows that – and is illustrated by the flat (dotted) line in Figure 4.3 – that the loss time for bremsstrahlung emission is independent of energy.

Synchrotron losses

Synchrotron losses occur when charged particles, subject to the Lorentz force, gyrate around the magnetic field lines. The gyration will be in the form of helical motion around and along the field lines and, as the electron executes this motion, it will lose energy in the form of synchrotron radiation. The loss time and rate is predictably a function of the energy and the magnetic field (Longair, 1994):

$$\left(\frac{dE}{dt}\right)_s = 2\sigma_T c\gamma^2 U_b \sin^2\theta = 9.9 \times 10^4 \gamma^2 B_\perp^2 \text{ [GeV s}^{-1}],\tag{4.20}$$

where $U_b = \vec{B}^2/8\pi$ is the energy density in the magnetic field measured in Gauss, $B_\perp = B\sin\theta$ is the magnetic field component perpendicular to the line-of-sight and is measured in Tesla (T), γ is the Lorentz factor, and σ_T is the Thompson cross-section.

It is common practice in astrophysics to use for the magnetic field amplitude units of Gauss, for which the conversion from Gauss to Tesla is $1\text{G} = 10^{-4}$ T. Thus, for easy reference $1\,\mu\text{G} = 10^{-6}$ G $= 10^{-10}$ T.

The above loss rate for synchrotron emission, gives a loss time which is also inversely proportional to the square of the magnetic field:

$$t_l^s = \frac{E}{dE/dt} \propto \frac{E}{B_\perp^2 \gamma^2} \propto \frac{1}{B_\perp^2 \gamma} \text{ [s]}.\tag{4.21}$$

Synchrotron emission from electrons radiating at an energy E, will radiate most of its energy at a frequency of (Crocker et al., 2007):

$$\nu = \left(\frac{E}{10\,\text{GeV}}\right)^2 \left(\frac{B}{\mu\text{G}}\right) \text{ GHz}.\tag{4.22}$$

Inverse Compton scattering

Electrons can also up-scatter low energy photons in a process called inverse Compton (IC) scattering. Here, the electron loses energy (to the photon) at a rate proportional to the energy density of the photon field, U_r:

$$\left(\frac{dE}{dt}\right)_{IC} = \frac{4}{3}\sigma_T c\gamma U_r.\tag{4.23}$$

Hence, the resulting loss times is dependent only on the energy density of the photon field:

$$t_l^{IC} = \frac{E}{dE/dt} \propto \frac{E}{\gamma^2} \propto \frac{1}{\gamma}.\tag{4.24}$$

Just like synchrotron emission, IC photons are emitted, for scattering of an electron of energy E, at a frequency corresponding to an energy:

$$E_\gamma^{IC} \sim 2\,\text{TeV}\left(\frac{T}{50\,\text{K}}\right)\left(\frac{E_e}{10\,\text{TeV}}\right)^2.\tag{4.25}$$
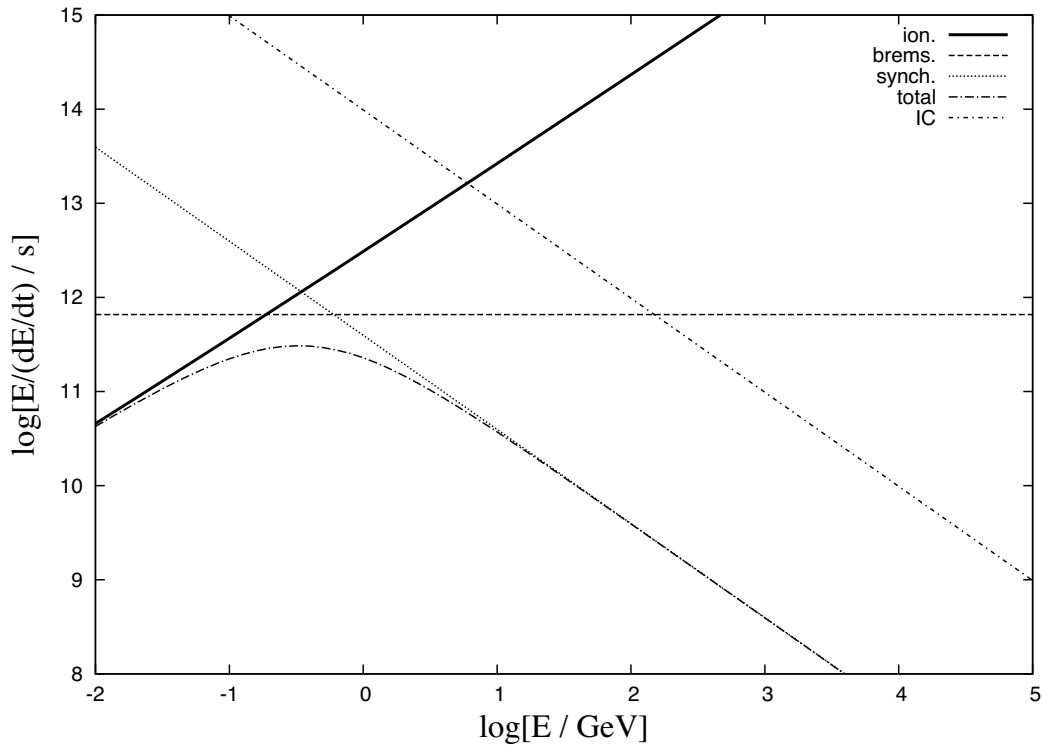
Figure 4.3: Loss times ($E/(dE/dt)$) for the same processes and values as describes the curves in Figure 4.2.

The above equation shows that IC emission is most important at TeV energies and can be an alternative to a nucleonic explanation for a variety of Galactic HESS sources (c.f. Chapter 1). In all cases presented in this thesis however, IC losses are sub-dominant to synchrotron losses at radio frequencies.

4.4 Production of secondary particles

The primary theme of this thesis are the means by which we can use the observed radio and/or γ-ray emission to explore the possible acceleration mechanisms of particles. Section 4.2 illustrated two ways by which particles can be accelerated. This section details the theory about the production of secondary electrons and positrons from the interaction of nucleonic CRs with ambient molecular matter. This section also contains an expanded discussion of the production of synchrotron emission from secondary particles as found in Chapter 5 (Jones et al., 2008). The material presented in this section is based on an unpublished research note by R.J. Protheroe (21/5/2006).

4.4.1 Production of secondary electrons, positrons and neutrinos

In contrast to synchrotron photons emitted by primarily accelerated electrons, synchrotron photons emitted by secondary electrons and positrons are dependent on the ambient molecular matter density. Thus, since the ambient molecular matter should primarily contain hydrogen and helium nuclei, the rate of interaction of CR hadrons with the ambient

molecular matter as a function of energy, $r_{int}^i(E)$, can be written as:

$$r_{int}^i(E) = \beta(E)c[n_H\sigma_{iH}(E) + n_{He}\sigma_{iHe}(E)], \qquad (4.26)$$

where n_H and n_{He} are the number density of hydrogen and helium respectively, $\sigma_{iH}(E)$ and $\sigma_{iHe}(E)$ are the respective cross-sections and $\beta(E)c$ is the Lorentz factor multiplied by the speed of light.

The production rate then, is proportional to the product of the interaction rate and the production spectrum of secondary particles, which is given by:

$$q_m(E, \vec{r}) = \sum_i \int n_i(E', \vec{r})r_{int}(E')p_{sec}^i(E, E')dE' \; [\text{cm}^{-3} \; \text{GeV}^{-1} \; \text{s}^{-1}], \qquad (4.27)$$

where $n_i(E, \vec{r}) = 4\pi J_i(E)/\beta(E')$ is the number density of CR hadrons using a CR spectrum of $J_i(E)$, and $p_{sec}^i(E, E')$ is the production rate of secondary particles. The production rate for the production of secondary particles as a function of energy for electrons and positrons is taken from Figure 4 of Moskalenko & Strong (1998).

The production spectrum of secondary particles per unit interstellar mass can then be found by dividing the production rate by the density, $\rho = n_H m_H(1 + 4n_H/n_{He})$, so that:

$$q(E, \vec{r}) = \frac{q_m(E, \vec{r})}{\rho} = \frac{c}{n_H m_H} \sum_i \int n_p(E')\epsilon(E')n_H\sigma_{pH}(E')p_{sec}^p(E, E')dE' \; [\text{g}^{-1} \; \text{cm}^{-3} \; \text{GeV}^{-1} \; \text{s}^{-1}],$$

$$(4.28)$$

where $\epsilon(E')$ is a correction factor due to elements heavier than hydrogen in the CR spectrum due to Mori (1997).

4.4.2 Synchrotron emission from secondary electrons and positrons

We now turn our attention to specifically obtaining the expressions for the emissivity of synchrotron photons created by secondary electrons and positrons. The production spectrum obtained in Equation 4.28 can be used to obtain the ambient number density of electrons and positrons by the integration from infinity to energy, E':

$$N(E, \vec{r}) = \frac{\int_{E'}^{\infty} q(E, \vec{r})dE'}{dE/dt} \; [\text{e}^{\pm} \; \text{cm}^{-3} \; \text{GeV}^{-1}], \qquad (4.29)$$

where dE/dt is the sum of the important loss processes (ionization, bremsstrahlung, and synchrotron) presented in Sections 4.3.2 and 4.3.3. Equation 4.29 assumes that the production occurs in the limit that the secondary electrons and positrons lose all their energy in situ.

The emissivity of synchrotron photons produced by secondary electrons and positrons can then be obtained by integration the ambient electron spectrum down to vanishing energies:

$$j_\nu(\vec{r}) = \frac{\sqrt{3}q^3}{4\pi m_e c^2}\left(\frac{B_\perp}{1\,\text{Gauss}}\right)_s \int_0^{\infty} N(E, \vec{r})F(\nu/\nu_c)dE \; [\text{erg cm}^{-3} \; \text{s}^{-1} \; \text{sr}^{-1} \; \text{Hz}^{-1}], \qquad (4.30)$$

where $F(\nu/\nu_c)$ is the first synchrotron function and is dependent on the Bessel function of fractional order, $K_{5/3}(z)$, q is the charge of the particle, m_e is the mass of the electron and $\nu_c = 4.19 \times 10^6(B_\perp/1\,\text{G})(E/m_e c^2)^2$ is the critical frequency. Thus, the flux density of synchrotron photons in Jansky (Jy; c.f. Section 4.3.1 above) is obtained through a simple unit conversion over the solid angle subtended by the emission region.

4.4.3 Total loss times and expected synchrotron flux density from secondary electrons and positrons

As has been shown above, the synchrotron emissivity is dependent on the density and mass (because the production rate of secondaries increases as the target density increases; c.f. Equation 4.28) and the magnetic field (because the synchrotron cooling rate is a strong function of magnetic field; c.f. Equation 4.20). On this basis, massive regions of medium density molecular matter ($\sim 10^4$ cm^{-3}), such as (giant) molecular clouds could provide a passive target for CRs to produce secondary electrons and positrons at a level which is detectable with sensitive radio continuum observations.

Figure 4.4 shows the total loss times for nominal molecular cloud parameters of mass 10^5 M$_\odot$ at a distance of 3 kpc assuming a CR spectrum the same as that observed at the top of the earth's atmosphere. Figure 4.4 (*Top*) shows that increasing the density actually increases the energy at which synchrotron losses become dominant, it leads to a decrease in the total loss time. This is because although more secondary particles are created (i.e., because for a fixed volume, increasing the density increases the number of target nuclei), bremsstrahlung losses are proportional to the ambient hydrogen density so that at lower energies, bremsstrahlung losses become dominant. Figure 4.4 (*Bottom*) shows that for a constant density and mass, then the energy at which synchrotron losses dominate decreases, and is accompanied *with* a decrease in total loss time once synchrotron losses dominate.

Figure 4.5 shows the expected synchrotron flux density for the same nominal cloud parameters as used in Figure 4.4. It is important to note that the flattening of the spectrum of synchrotron emission flattens towards lower energies as the dominant loss process changes from synchrotron to bremsstrahlung losses. Furthermore, Figure 4.5 (*Top*) illustrates that increasing the density does not change the frequency at which this transition occurs. However, increasing the magnetic field as illustrated in Figure 4.5 (*Bottom*), *increases* the frequency at which this transition occurs, and that for the nominal cloud parameters presented here, for the strongest magnetic field values, this flattening behaviour can occur at GHz frequencies.

The flux densities observed in Figure 4.5 show that molecular clouds which have high magnetic fields and moderate ambient hydrogen densities could be a source of synchrotron emission from secondary electrons and positrons. Furthermore, if synchrotron emission which is attributable to secondary electrons and positrons is not observed and given that the relativistic particle density is known, then limits to the magnetic field amplitude, $B_\perp$, can be obtained.

4.5 Summary

This chapter builds on the content which was introduced in Chapter 1 in that it explores the theory behind particle acceleration and cooling. Specifically, we have introduced the two main mechanisms by which CRs are believed to be accelerated and come under the umbrella of diffusive particle acceleration: first- and second-order Fermi acceleration.

Once particles have been accelerated in sources such as SNRs, they are subject to losses due to interactions with electromagnetic fields and/or ambient matter. The loss processes which are important in this thesis are ionisation losses, blackbody radiation, thermal bremsstrahlung, inverse Compton and synchrotron emission. We have discussed each in turn, highlighting the most important relationships, such as cooling rates and times.

Finally, we have explored secondary particle production in terms of a static, one-zone
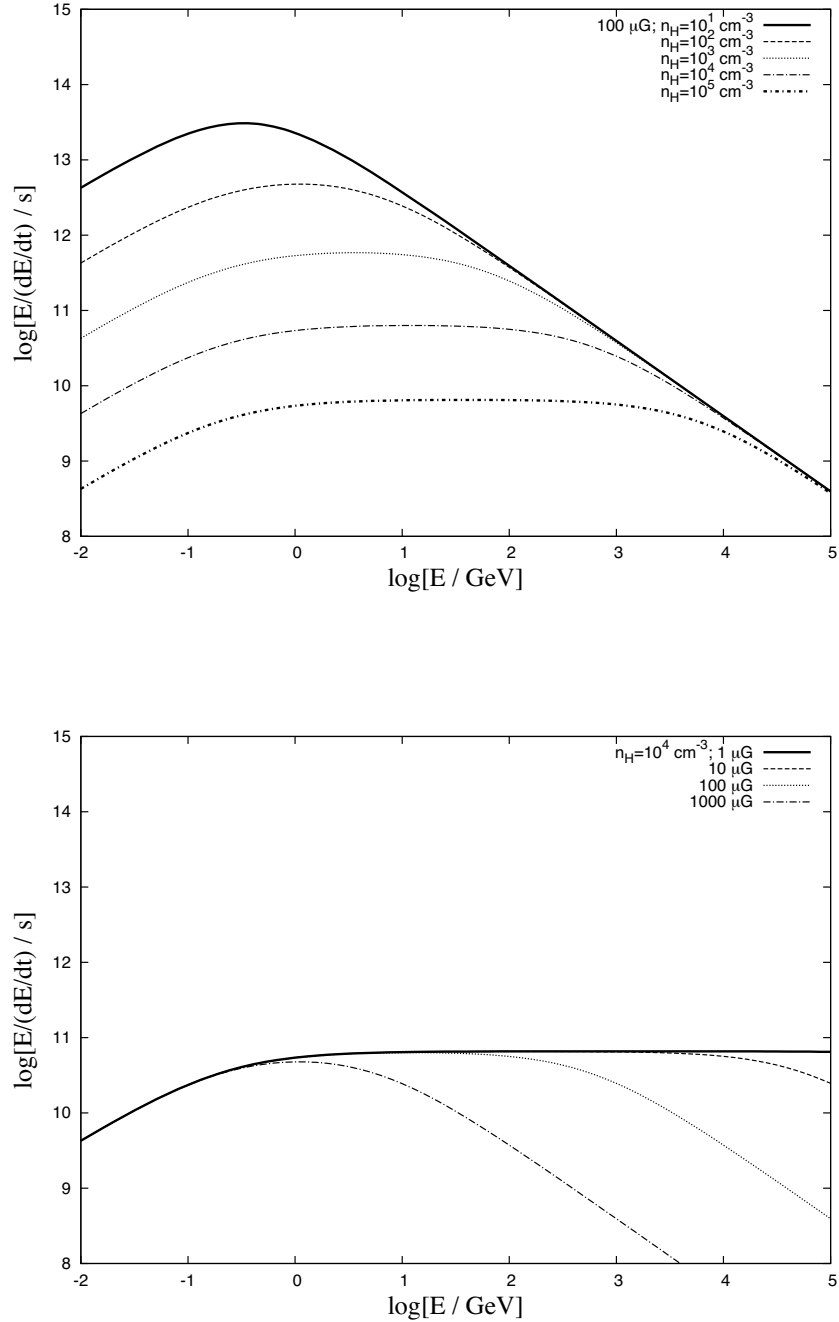
Figure 4.4: Total loss times as a function of energy for the nominal cloud parameters listed in the text, for (*Top*) $B_\perp = 100 \, \mu$G and ambient cloud densities of 10^1 (bottom curve), 10^2, 10^3, 10^4, and 10^5 cm^{-3} (top curve) and (*Bottom*), an ambient density of 10^4 cm^{-3} with $B_\perp = 1$ (top curve), $10, 100,$ and $1000 \, \mu$G (bottom curve).

model for the production of secondary electrons and positrons, which then produce synchrotron emission from their interaction with ambient magnetic fields. The secondary electrons and positrons are created in the interactions of CR nucleons with ambient matter density, and represent a part of non-thermal emission which has been seldom discussed in the literature, but may be a dominant contribution (in respect to synchrotron emission from primarily accelerated electrons and positrons) under certain conditions.
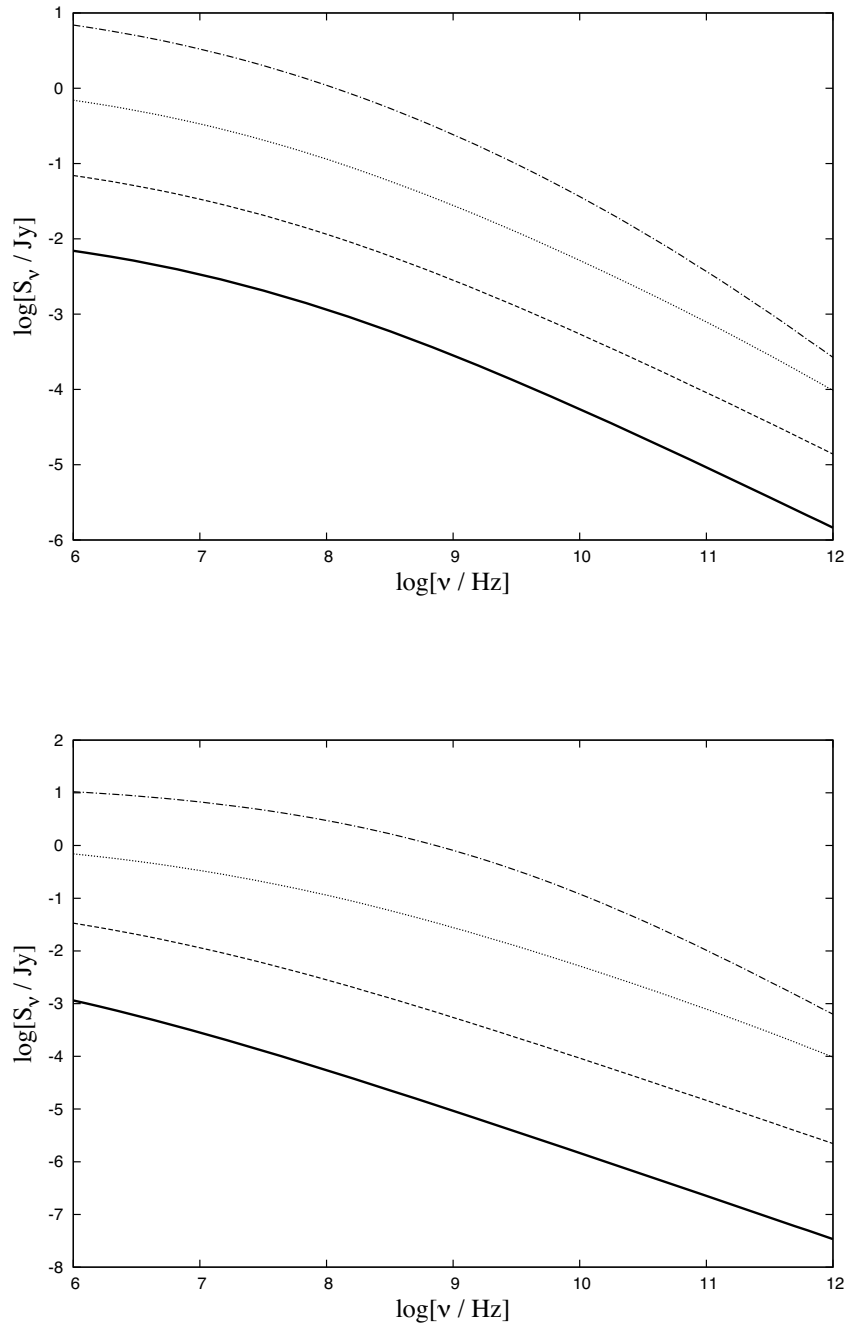
Figure 4.5: (*Top*): Expected flux density (in Jy) using nominal cloud values for differing density values, starting at (lowest) $n_H = 10^2$, to $n_H = 10^5$ (highest) with the same values as in Figure 4.4 (*Top*). (*Bottom*): Expected flux density for the same cloud using a nominal density of 10^3 cm^{-3} and magnetic field values of 1 μG (lowest), 10 μG, 100 μG, and 1 mG (highest).

Upper limits on the magnetic field of two cold dark dense cores

<div style="text-align: right">5</div>

This chapter is the paper which has been published in the journal, Publications of the Astronomical Society of Australia. It details the search for synchrotron emission due to secondary electrons and positrons created in interactions with CRs and the molecular material in cold dark dense clouds.

Australia Telescope Compact Array radio continuum 1384 and 2368 MHz Observations of Sgr B

6

This chapter is the paper which has been submitted for publication in the Astronomical Journal.

6.1 Abstract

We present images of the Sagittarius (Sgr) B giant molecular cloud at 2368 and 1384 MHz obtained with the Australia Telescope Compact Array (ATCA) with a resolution of $47'' \times 18''$ and $27'' \times 8''$ at 1384 and 2368 MHz respectively. All images were produced with ATCA data in multiple array-configurations and have been combined with archival single dish data, resulting in images which are sensitive to emission from the resolution of the images to 2 degrees at both 1384 and 2368 MHz.

We use our images, together with archival 74 and 330 MHz VLA, 843 MHz SUMSS, 23 GHz ATCA and higher frequency VLA data to create the most detailed radio continuum spectrum of the Sgr B2 molecular cloud complex ever assembled. The motivation for producing this spectrum is our theoretical work investigating the possibility that synchrotron emission from secondary electrons and positrons created in cosmic ray (CR) collisions with the ambient matter of the Sgr B2 cloud could provide a detectable, non-thermal radio signal.

We have produced linear polarization images of Sgr B2 at 1384 and 2368 MHz. We find no statistically significant polarization from Sgr B2 and that any polarized emission should be completely depolarized within the cloud.

Our modeling also indicates that there could be a relative dimming of the center of the cloud due to the probable exclusion of the $\sim 1 - 10$ GeV CRs from densest parts of the cloud (leading to a 'limb-brightened' morphology). We do not, however, find any spectral or morphological evidence for synchrotron radio emission from secondaries from the main complex of Sgr B2.

We find a strong source to the south of Sgr B2 is non-thermal in nature between 1384 and 2368 MHz. We find integrated flux densities of 3.7 ± 0.2 Jy at 1384 MHz and 2.3 ± 0.1 Jy at 2368 MHz for a source of FWHM size at 1384 MHz of $\sim 54''$ but that this emission cannot be attributed to secondary electrons.

6.2 Introduction

The Sagittarius B (Sgr B) cloud, is one of the largest and most complex star forming regions in the Galaxy. Assuming a distance to the Galactic center of 8.5 kpc, Sgr B lies at a projected distance of ~100 pc from the Galactic center and consists of the massive star forming regions

Sgr B1 and B2. Both Sgr B1 and B2 have been well studied at all wavelengths, including centimeter radio continuum. Sgr B1 possesses many more lager, diffuse HII regions than Sgr B2 and a different structure of Hα lines – signs of relatively more advanced star formation. Sgr B1 appears to be older than Sgr B2 (Mehringer et al, 1995). In contrast, Sgr B2 has many (upwards of 60; Gaume & Claussen 1990; Mehringer, et al 1992) ultra-compact HII (UCHII) regions, signs of ongoing massive star formation.

There have been surveys of Sgr B with high resolution at 0.3, 1.4, 4.8 and 8.6 GHz using the Very Large Array (VLA) (see Lang, Palmer & Goss (2008) for an excellent review on the observational history of the Sgr B region). Indeed, this paper provides an opportunity to compare our 1.4 GHz image with Lang, Palmer & Goss (2008), and present the first 2.4 GHz image of this region. The 2.4 GHz image presented here fills a gap at a important position in the spectrum aiding in the separation of thermal and non-thermal emission from sources from within the Sgr B complex. The Australia Telescope Compact Array (ATCA)[1] is the only aperture synthesis radio telescope capable of observing Sgr B with arcsecond resolution at 2.4 GHz (λ13 cm). Yet there are no sensitive, sub-arcminute resolution images of Sgr B at this frequency.

The motivation for the current study comes from our theoretical work (Protheroe et al., 2008). This work showed that synchrotron emission from secondary electrons created in cosmic ray (CR) collisions with the ambient matter of the Sgr B2 cloud could possibly provide a detectable, non-thermal radio signal (throughout this paper we refer to electrons as electrons and positrons). Our modeling also indicates that there could be a relative dimming of the center of the cloud due to the probable exclusion of the $\sim 1 - 10$ GeV CRs from densest parts of the cloud (leading to a 'limb-brightened' morphology).

To test the hypothesis that appreciable non-thermal emission is present in the low frequency radio continuum spectrum of Sgr B2, we have assembled new multi-array-configuration 1384 and 2368 MHz ATCA data (combined with archival single-dish data), archival VLA 74 and 330 MHz and SUMSS 843 MHz data. These data are described in Section 6.3 along with details of the data reduction of the new 1384 and 2368 MHz images. New images of the Sgr B region at 1384 and 2368 MHz are then presented in Section 6.4 in addition to a detailed discussion of the morphology of sources observed and a comparison to published work. Section 6.5 details our analysis of the data to explore the hypothesis of possible synchrotron emission from Sgr B2 due to the production of secondary electrons. Our conclusions are presented in section 6.6.

6.3   Radio Continuum Observations: New and Old

In order to best characterize the radio emission of Sgr B2 on a range of scales, we have assembled a catalog of radio images covering the Sgr B2 region at frequencies from 74 MHz to 230 GHz; the details of which are listed in Table 6.1. From the three different 330 GHz VLA images, we have selected the data of LaRosa et al. (2000) as being most suitable to explore the possibility of synchrotron emission from secondary electrons. This is because the combination of VLA configurations gives enough resolution to separate the different components of Sgr B2, without filtering out the large scale structure.

Figure 6.1 shows contours of the Sgr B region at 1384 MHz and labels the sources referred to in the text. To match the 330 MHz VLA data of LaRosa et al. (2000), we embarked on a

---

[1]The Australia Telescope Compact Array is part of the Australia Telescope which is funded by the Commonwealth of Australia for operation as a National Facility managed by CSIRO.
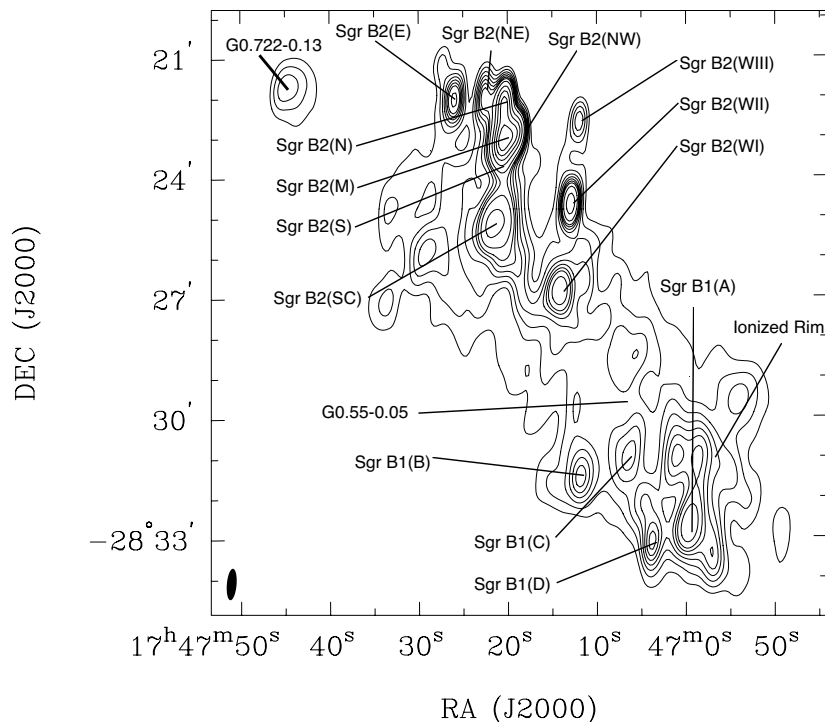
Figure 6.1: Image of 1384 MHz total intensity contours of the Sgr B region showing the sources as labeled in Table 6.3. Contours are at 200, 250, 300, 350, 400, 450, 500, 600, 800, 1000, and 1600 mJy beam^{-1} . The image has a resolution of $47'' \times 14''$, which is illustrated by the beam in the lower left-hand corner.

program of observations with the ATCA at 1384 and 2368 MHz which would compliment the (u,v)-range of the archival 330 MHz VLA image from LaRosa et al. (2000) shown in Figure 6.2.

Table 6.1: Observational parameters of the entire dataset.

ν (MHz)	FoV (°)	Beam size ('')	Ref.
74	11	114×60	Brogan et al. (2003)
330	4	7×12	Nord et al (2004)
330	—	41×22	LaRosa et al. (2000)
330	—	120×60	Brogan et al. (2003)
843	0.5	90×43	Mauch et al (2003)
1384	0.3	47×14	This Paper
1408	—	~ 600	Reich & Reich (1986)
2368	0.2	27×8	This Paper
2417	—	~ 246	Duncan et al. (1995)
23,000	0.1	26×17	Ott et al. (2006)
230,000	0.01	5×3	Qin et al. (2006)

6.3.1 New ATCA Observations

Table 6.2 lists the details of the observations taken with the ATCA, which are described in detail below.
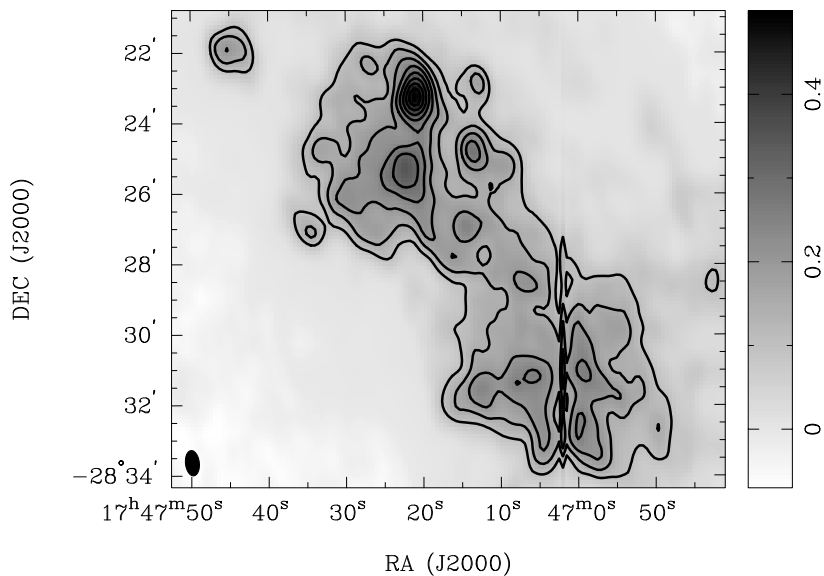
Figure 6.2: 330 MHz total intensity medium resolution image of Sgr B2 with a beam of $41'' \times 22''$ (located in the lower left corner: (LaRosa et al., 2000)). The contours are 330 MHz total intensity contours at 0.1, 0.15, 0.2, 0.25, 0.3, 0.35, 0.4 and 0.45 Jy beam^{-1}. The intensity scale on the right is in units of Jy beam^{-1} and is set from -0.07 to 0.5 Jy. The line in the image in Sgr B1 is an image artifact due to the download from `http://rsd-www.nrl.navy.mil/7213/lazio/GC/`.

Table 6.2: Observational parameters of the entire dataset.

ν (MHz)	$\Delta\nu$ (MHz)	Array	Time (hours)	Date
1384	128	1.5C	10	2005 Dec
		750A	10	2007 Jan
		750D	8	2007 Mar
2368	128	1.5C	10	2005 Dec
		750A	10	2007 Jan
		750D	8	2007 Mar

1.5C configuration

Single pointing ATCA radio continuum observations were conducted on 2005 December 4th and 5th using the 1.5 C array-configuration utilizing five of a possible six antennae and covering baselines on an east-west track from 76.5 m to 1.4 km. Observations were conducted simultaneously at 1384 MHz ($\lambda20$ cm) and 2368 MHz ($\lambda13$ cm), each spanning 128 MHz in bandwidth and recording all four polarization products. At these frequencies, the FWHM primary beam (FoV) of ATCA is $34'$ at 1384 MHz and $20'$ at 2368 MHz. The total integration time was 600 minutes obtained in 15 minute cycles on the 4th for approximately 10 hours. Flux density and phase calibrations were undertaken with PKS 1934-638 (we assume flux densities of 14.95 and 11.59 Jy at 1384 and 2368 MHz for PKS 1934-638 throughout this paper) and PKS 1740-517 from the ATCA calibrator catalog.

750m array-configurations

We have performed a 7-pointing mosaic observation of the entire Sgr B region using the 750A and 750D array-configurations of the ATCA. The purpose of the mosaic was to cover the Galactic center region at 2.4 GHz and the full data set will be described in a future

paper. However, the addition of the mosaic data gives the images sensitivity to larger scale emission. The combination of the two 750 array-configurations (750A and 750D) has east-west baselines from 30m to 750m in 20m increments. We used the same 128 MHz bandwidth with frequencies centered at 1384 and 2368 MHz recording all four polarization products as the 1.5C configuration observations. We followed a fully-sampled hexagonal pointing mosaic providing uniform sensitivity over the entire Sgr B region. The primary and phase calibrators were PKS 1934-638 and PKS 1740-517 respectively.

6.3.2 Single-dish data

In order to fill in the missing short-spacing information for the new ATCA images, we have obtained archival single dish data at 1408 and 2400 MHz from wide-field surveys obtained using the Effelsberg (EBG; Reich & Reich 1986) and Parkes (PKS; Duncan et al. 1995) telescopes respectively.

The 1.4 GHz data comes from the EBG wide field survey at 1420 MHz, covering the sky from $-19° < \delta < 90°$, with a resolution of $9'.1$. The RMS noise is 125 mJy beam^{-1} with an estimated calibration error of $\sim 5\%$.

The 2.4 GHz PKS Galactic plane survey covered $\sim 40°$ in Galactic longitude, and $\pm 5°$ in Galactic latitude and includes the GC at a resolution of $\sim 10'$. The RMS noise of the survey is ~ 12 mJy beam^{-1} with a bandwidth of 145 MHz.

6.3.3 Image deconvolution

To produce the images presented in this paper, each set of interferometer data was calibrated separately using standard calibration procedures of the MIRIAD software package. Imaging was then performed by Fourier transforming the entirety of the interferometer data using the MIRAD task *invert*, and deconvolved using the MIRIAD task *mosmem*.

The single dish data at 1.4 and 2.4 GHz from Duncan et al. (1995) and Reich & Reich (1986) described in Section 6.3.2 were combined with the interferometer data using the MIRIAD task *immerge*. The data were combined after image deconvolution of the interferometer data (Stanimirovic, 2002). This 'linear' method works on the assumption that the single-dish image is a good representation of the object at low spatial frequencies, whereas the interferometer data better represents the high spatial frequencies. The image is created by tapering (in the Fourier domain) the low spatial frequencies of the interferometer data so that the sum of the single-dish and interferometer (tapered) data is a gaussian beam equal to the beam of the interferometric data.

6.4 Results & discussion

In this section we present images of the Sgr B region produced using the data described in the previous section. We then discuss the spectral and morphological features of the region. Figure 6.3 (*Top*) and (*Bottom*) shows the Sgr B region at 1384 and 2368 MHz at a resolution of $47'' \times 14''$ at 1384 MHz and $27'' \times 8''$ at 2368 MHz and represents the highest resolution image of the GC region at 2.4 GHz ever produced. The images have an RMS noise limit of 10 mJy beam^{-1} at 1384 MHz and 5 mJy beam^{-1} at 2368 MHz. For reference, the positional accuracy of the ATCA at centimeter wavelengths is $\sim 5''$[2].

---

[2]http://www.narrabri.atnf.csiro.au/observing/pointing/

6.4.1   Sgr B morphology

At radio continuum frequencies, the Sgr B complex is the second-brightest source in the
Galactic center region, with only Sgr A being brighter. Figure 6.3 (*Top*) and (*Bottom*) shows
the entire Sgr B region at 1384 and 2368 MHz respectively which is composed of two sub-
regions: Sgr B1 (G0.5-0.0) and Sgr B2 (G0.7-0.0). We measure a flux density from the entire
region of ∼ 70 Jy at 1384 MHz and ∼ 80 Jy at 2368 MHz.

We note here that the 1384 MHz flux density agrees well with the 1.4 GHz flux density
of 83 ± 7 Jy stated in Lang, Palmer & Goss (2008). It is also consistent with the integrated
spectral index obtained between 4.8 and 8.5 GHz using the GBT by Law et al (2007). We
conclude that the 2.4 GHz flux density stated above from a similar solid angle reinforces the
conclusions of Lang, Palmer & Goss (2008) that the integrated flux from the Sgr B region is
thermal in nature.

This result does not contradict the previous claim of non-thermal emission from this
region by Crocker et al. (2007) who measured the spectrum over the region used for analysis
by the HESS γ-ray telescope by Aharonian et al (2006), which is an area of ∼ 1 square degree
- a much larger region than that being integrated here.

The main complexes (Sgr B1 and B2) also lie upon a broad region of emission which
is particularly evident in Figure 6.3 (*Top*) at 1384 MHz, but largely absent in Figure 6.3
(*Bottom*) at 2368 MHz.

Table 6.3 lists the sources, as labeled in Figure 6.1 within Sgr B which are observed at
the resolution of the 1384 MHz synthesized beam. The columns 1 to 8 are: source name
(for which standard names are used where possible); (Epoch J2000) Right Ascension and
Declination of the sources; the peak intensity of the source at 1384 and 2368 MHz at the
resolution of the synthesized beam (in Jy beam^{-1}); the integrated flux density of the source
at 1384 and 2368 MHz integrated using images re-gridded and convolved to the resolution
of the 1384 MHz image; the spectral index and associated error taken from the integrated
flux densities given in the previous columns.

Sgr B1

Sgr B1 is a star forming region which is situated to the southwest of – and possibly in front
of (Bieging et al., 1980) – Sgr B2. Because the region is dominated by sources which are
extended and emit radio recombination lines over a large velocity range, it is thought that
Sgr B1 is at an advanced stage of evolution compared to Sgr B2 (Mehringer, et al, 1992).
Table 6.3 shows that the spectral index between 1384 and 2368 MHz is different between
the regions: Sgr B2 has several optically thick HII regions (such as Sgr B2(M) and (N)),
whereas Sgr B1 is devoid of such regions. This distinction continues to high resolutions,
where Sgr B2 is known to consist of at least 60 individual HII, ultra-compact HII (UCHII)
and hyper-compact HII (HCHII) regions (Gaume & Claussen, 1990; Mehringer, et al, 1992),
whereas there are ∼ 10 sources found in Sgr B1 (Mehringer et al, 1995). This may be evidence
in favour of the hypothesis that Sgr B1 is older than Sgr B2 because at radio continuum
frequencies, an observational manifestation of recent star formation is the formation of
HCHII and UCHII. A lack of these regions within Sgr B1 suggests that star formation is not
occurring at present however, the larger size of these optically thin regions suggests that
star formation has occurred in Sgr B1 in the past (Mehringer, et al (1992) and references
therein).

Figure 6.3 shows that Sgr B1 consists of ∼ 5 sources which are labeled as Sgr B1(A-D)
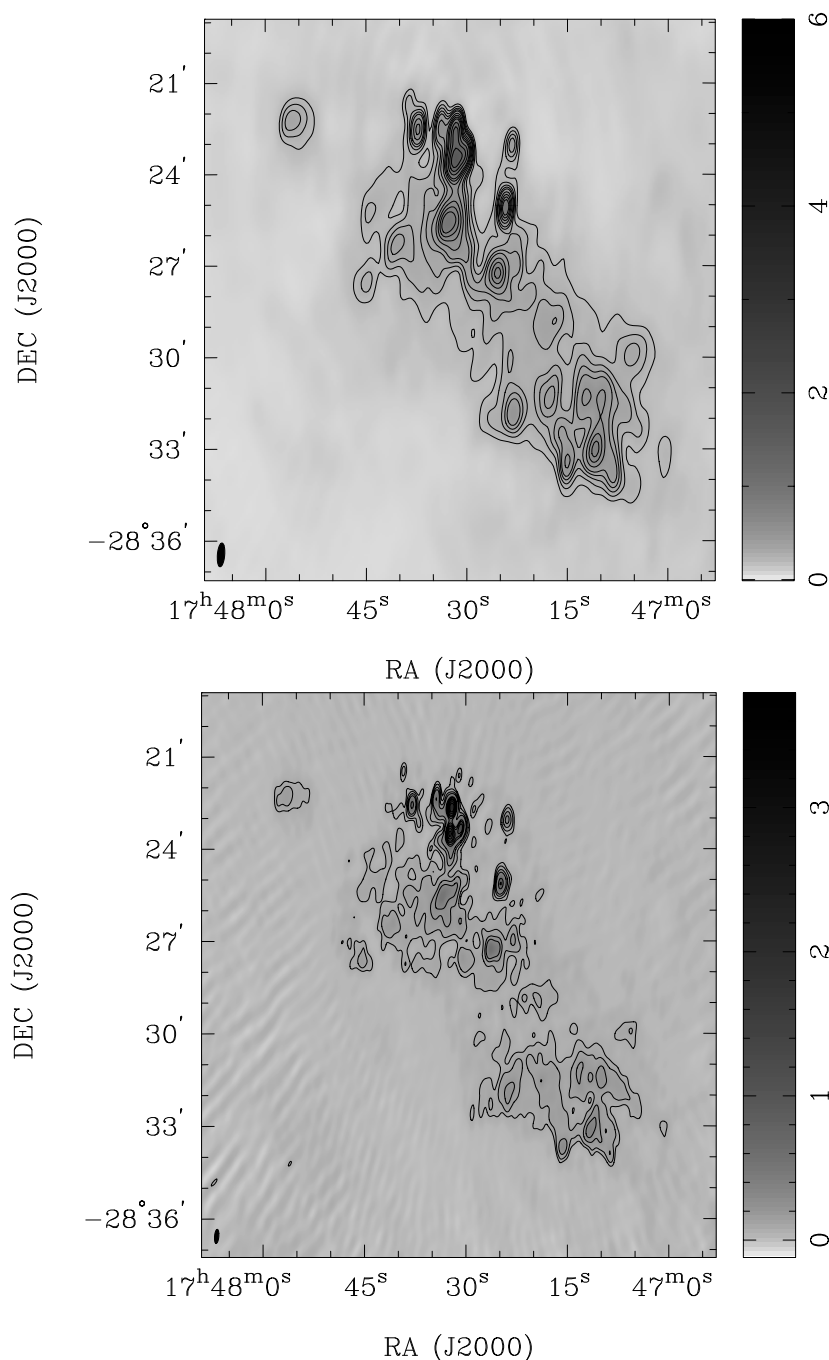
Figure 6.3: Closeup of the Sgr B region at 1384 MHz (*Top*) and 2368 MHz (*Bottom*). The 1384 MHz image has contours at: 0.2, 0.25, 0.3, 0.35, 0.4, 0.5, 0.6, 0.7, 0.8, 1.0, 1.2, and 1.4 Jy beam^{-1} and a resolution of $47'' \times 14''$ with the beam located in the lower left hand corner. The 2368 MHz image has contours at: 0.08, 0.12, 0.2, 0.3, 0.64, 0.8, 1.0, 1.2, 1.5, and 1.8 Jy beam^{-1} . Jy beam^{-1} and a resolution of $27'' \times 8''$ with the beam located in the lower left hand corner. The RMS noise level of the images are 10 mJy beam^{-1} at 1384 MHz and 5 mJy beam^{-1} at 2368 MHz, matching the sensitivity at 1384 MHz of similar resolution images.

and the Ionized bar in Table 6.3 and Figure 6.1. Sources A, B and D correspond to the sources described in Mehringer, et al (1992) and Mehringer et al (1995) as the Ionized Bar and Sources E and I[3]. The Ionized Bar is the source to the northwest of Sgr B1 in Figure 6.3 at 2368 MHz, which is not fully resolved at 1384 MHz. To the south of this is the Ionized

---

[3]Due to the difference in resolution, we do not follow the naming convention of Mehringer et al (1995), since discrepencies in flux density may lead to anomalous attributions of flux densities

Rim and Source E – which shows an extension to the north consistent with Ridge 2 from Mehringer, et al (1992). The source to the northeast is Source I. Source confusion means that the flux densities presented in Table 6.3 should be taken as a rough guide only – higher resolution images at 2368 MHz are needed to properly categorize the emission from these regions at these frequencies.

We find a total flux density of 27 ± 1.4 Jy at 1384 MHz, which is consistent with the 1.4 GHz flux density found in Mehringer, et al (1992). Due to the addition of the low spatial frequencies contained in the single-dish data, a component of this flux density will be due to foreground/background diffuse emission. This contribution to the total flux density at both frequencies was derived in the following way: the average total flux density of a number of similar-sized regions was calculated and subtracted from the total flux density stated above. Thus, for the entire Sgr B1 region *only*, we find a flux density of 14.8 ± 0.8 Jy at 1384 MHz and 12.8 ± 0.6 Jy at 2368 MHz, broadly consistent with optically thin emission from HII regions.

Name	R.A. (J2000)	Dec. (2000) (J2000)	$I_{1.4}$ (Jy beam^{-1})^a	$I_{2.4}$ (Jy beam^{-1})^a	$S_{1.4}$ (Jy)	$S_{2.4}$ (Jy)	$\alpha_{2368}^{1384,b}$
(1)	(2)	(3)	(4)	(5)	(6)	(7)	(8)
Sgr B2(M)	17:47:20.5	-28:22:53.7	2.0	1.2	3.4	3.8	1.0 ± 0.3
Sgr B2(N)	17:47:20.1	-28:22:18.3	1.8	1.3	2.5	3.5	1.4 ± 0.3
Sgr B2(S)^c	17:47:20.5	-28:23:34.3	1.5	0.8	1.5	2.5	1.1 ± 0.3
Sgr B2(NE)^c	17:47:22.4	-28:21:57.8	0.5	0.3	1.2	1.1	1.2±0.3
Sgr B2(NW)^c	17:47:18.6	-28:22:54.0	1.0	0.5	1.6	1.8	0.4 ± 0.3
Sgr B2(E)	17:47:25.8	-28:22:05.4	0.6	1.0	1.4	1.7	0.4 ± 0.3
Sgr B2(SC)	17:47:21.7	-28:25:20.4	1.0	0.5	3.7	2.3	−0.9 ± 0.3
Sgr B2(WI)	17:47:14.1	-28:26:52.3	0.7	0.4	1.2	1.1	−0.2 ± 0.3
Sgr B2(WII)	17:47:12.9	-28:24:35.9	0.8	0.6	1.1	1.2	0.2 ± 0.3
Sgr B2(WIII)^d	17:47:11.8	-28:22:4.54	0.4	0.5	0.4	0.5	0.4 ± 0.4
Sgr B1(A)^d	17:46:59.5	-28:32:43.0	0.8	0.9	0.8	0.9	0.3 ± 0.3
Sgr B1(B)	17:47:11.9	-28:31:29.3	0.5	0.6	2.4	2.7	0.2 ± 0.3
Sgr B1(C)	17:47:06.2	-28:31:01.6	0.4	0.5	1.6	1.7	−0.1 ± 0.3
Sgr B1(D)	17:47:03.8	-28:33:06.9	0.5	0.6	1.8	2.1	0.3 ± 0.3
Ionized bar^c	17:46:58.6	-28:30:58.2	0.5	0.6	5.6	5.3	−0.1 ± 0.3

Table 6.3: Discrete sources within Sgr B. ^{a} Peak intensity of the source in units of Jy beam^{-1}. ^{b} The spectral index error is a 5-σ error. ^{c}At the resolution of the 1384 MHz images these sources are confused by other sources. ^{d} Denotes point sources, where the integrated flux densities are the peak flux densities.

Sgr B2

Figure 6.3 (*Top*) and (*Bottom*) shows that the compact core of Sgr B2 is the brightest part of the Sgr B region. Whilst at 1384 MHz this is unresolved, at 2368 MHz the compact core is resolved into two parts, main (M) and north (N). These are known to be very active star-forming regions and emit optically thick HII emission. Again at 2368 MHz, there is an extension to Sgr B2(M) in the south, which is the southern part of the cloud, Sgr B2(S), mentioned earlier. This extension is resolved out at 1384 MHz due to the larger beam-size.

At 2368 MHz, the smaller beam size also partially resolves two sources: one to the east and the other to the west of Sgr B2(N). Both sources are known HII regions, Sgr B2(NW) (G0.666-0.03) and Sgr B2(NE) (G0.689-0.03). These are located to the west and east, respec-

tively, of Sgr B2(M) and (N), and are associated with Sgr B2 (Mehringer et al, 1995; Gaume et al., 1995).

Further to the south is another source which is resolved at both 1384 and 2368 MHz, which we term Sgr B2 southern complex – Sgr B2(SC) (G0.637-0.06) and is referred to as the non-thermal source in Protheroe et al. (2008). Though only just resolved at 1384 MHz, this source is of similar extent at 2368 MHz, where it is fully resolved. The possibility of non-thermal emission from this source has been remarked upon in Gray (1994a). The nature of this source will be more fully explored in a future paper (Jones et al, 2008b).

Sgr B2(WI), (WII) and (WIII)

Here we discuss three sources, denoted Sgr B2(WI), Sgr B2(WII) and Sgr B2(WIII), and compare the morphology and spectral information illustrated in Table 6.3 with previous observations.

Sgr B2(WI) is coincident with the IRAS source IRAS17440-2825, located 1.5″ away from the peak of the radio emission (Val'tts et al., 1999), and contains a Class II methanol maser source (Slysh et al., 1999). At a distance of 4.32″ from the radio continuum peak presented here is the radio source DGSW 60 (Downes et al., 1979). This source has a flux density of 0.8 Jy at 5 GHz, consistent with our detection of an optically thin HII region and the flux densities presented in Table 6.3.

Table 6.3 shows that Sgr B2(WII) is another optically thin HII region. This source is listed as MD72(62) by Downes et al. (1979), 2.3″ distant from the peak in our images. They find flux densities of 1.4 and 1.1 Jy at 5 and 10.4 GHz respectively – consistent with the present observations.

Sgr B2(WIII) is also detected in Downes et al. (1979). With a flux density of 0.6 Jy at 5 GHz it is also consistent with an optically thin HII region. Although the Downes et al. (1979) source is 5.41″ away, the spectral index given in Table 6.3 is thermal source, thus we argue that the low flux density of this source at 1384 and 2368 MHz, together with the 5 GHz flux density datum from Downes et al. (1979), implies that this source should be classified as an optically thin HII source.

Sgr B2(SC) (G0.637-0.06)

We find a strong source to the south of the main Sgr B2 complex which has previously been described as a possible non-thermal source (Gray, 1994a) and is referred to as the non-thermal source in Protheroe et al. (2008). The NH_3 data (Ott et al., 2006) – shown in Figure 6.4 – exhibits a molecular extension to the south of Sgr B2 which is not coincident with the peak intensity of Sgr B2(SC) at 1384 and 2368 MHz as labeled in Figure 6.1. We also, however, find a strongly non-thermal spectral index for this source ($\alpha = -0.9 \pm 0.3$) between 1384 and 2368 MHz. LaRosa et al. (2000) list a source close to this in Table 2 of their paper with a flux of 660 mJy beam^{-1} for a source size (angular FWHM) of 54″, agreeing well with the source size observed in Figure 6.3. It is significantly stronger at 1384 MHz (~ 3.7 Jy beam^{-1}), suggesting that this source could be self-absorbed at 330 MHz.

At this resolution (47″ × 14) we are unable to clearly identify the source of the non-thermal emission due to the morphology and spectral index alone. Using the spectral line data of the NH_3 emission (shown in Figure 6.4 and discussed in detail below), we estimate an average density of $10^3 \lesssim n_H \lesssim 10^5$ cm^{-3}. Using these parameters, a source of the (linear) size of Sgr B2(SC) – FWHM at 8.5 kpc ~ 2.5 pc – the emissivity of the radio continuum flux

due to synchrotron emission from secondary electrons is independent of the density and total mass. Instead, for a high enough density the emissivity is a function of the *volume*, since for a fixed magnetic field and volume, the increased injection rate of secondary particles by increasing the density is almost exactly cancelled by the increased efficiency of the bremsstrahlung cooling, leaving the steady state distribution unchanged. Such a regime results in at most ~ 1 mJy of radio continuum flux due to synchrotron emission from secondary electrons at 1 GHz. This can be increased to 10 mJy by over-normalizing of the CR spectrum in this region by a factor of 10 as per the finding for the CR spectrum at TeV energies by HESS (Aharonian et al, 2006), even though there is no direct evidence for such an enhancement (see Protheroe et al. (2008) for a more detailed discussion).

6.4.2   Polarization

Standard synchrotron theory suggests that synchrotron emission (whether from primary or secondary electrons) should be ~ 70 − 80% polarized (Rybicki & Lightman, 1979). Indeed, the GC region is also known to contain sources of strong polarized intensity, such as the non-thermal radio filaments (NTFs), which are thought to be due to synchrotron emission from relativistic electrons (Yusef-Zadeh, Hewitt & Cotton (2004) and references therein). The NTFs (which are not observed elsewhere in the Galaxy) exhibit a large fractional polarized intensity (up to 65% at radio continuum wavelengths; LaRosa, et al 2003).

Polarized emission from Sgr B2 has been observed at far-infrared (FIR) wavelengths at 60 μm (Dowell, 1997) and 115 μm (Novak et al., 1997) and perhaps also due to spinning dust grains (with a charge asymmetry) in the WMAP cosmic microwave background maps. Novak et al. (1997) and Dowell (1997) argue that the FIR polarization in the core of Sgr B2 is due to *absorption* by magnetically aligned dust grains whereas the FIR polarization in the envelope is due to *emission* from magnetically aligned dust grains. These observations also show that the magnetic field structure in Sgr B2 is not turbulent at size scales greater than that corresponding to the beam size, which was, serendipitously, ~ 35″ Novak et al. (1997). Hence because the magnetic field is not turbulent on size-scales corresponding to those that we are investigating, we do not expect our images to suffer from beam or depth depolarization.

As will be investigated in the following section, Protheroe et al. (2008) showed that non-thermal emission from secondary electrons in the Sgr B2 cloud may exhibit a morphology which follows the distribution of molecular gas and may possibly be 'limb-brightened'. We thus seek to find any polarised emission which also follows such a distribution from the Sgr B2 cloud.

We have produced images of the Stokes Q, U and V parameters at both 1384 and 2368 MHz. The data was calibrated using the standard MIRIAD data calibration described in Section 3.3. To produce the images, we have used the MIRIAD task *pmosmem*, which performs a joint maximum entropy deconvolution of the total and polarized intensities for mosaic observations simultaneously (Sault et al., 1999). A maximum entropy was preferred (to a CLEAN-based method) because it recovers large scale structures measured by the mosaiking process (Ekers & Rots, 1979) and allows the Stokes Q, U and V images to have negative values. Following deconvolution, each image was smoothed with a Gaussian restoring beam of FWHM of 47″ × 17″ and 27″ × 8″ at 1384 and 2368 MHz respectively. Images of linearly polarized intensity, $L = (Q^2 + U^2)^{1/2}$ and linearly polarized position angle, $\theta = 1/2 \tan(U/Q)$ were produced using the standard MIRIAD task, *impol*, blanking the output

below a level of 5σ.

Sources of error in polarisation observations

Each antenna of the ATCA measures the incoming radiation using two orthogonal linearly polarised feeds (as opposed to a telescope, such as the VLA, which uses circular polarized feeds), and so measures the correlation between four polarization spectra, XX, YY, XY and YX. The main source of errors in the polarized flux density images for data taken with the ATCA is (i) the leakage of polarised flux both to and from polarized intensity to total intensity, and (ii) the on and off-axis polarization purity.

In its section on polarisation observations, the ATCA Users Guide[4] suggests that properly calibrated polarimetric observations with the ATCA can reduce on-axis polarimetric errors to ~ 0.3%. Additionally, the ATCA Users Guide suggests that the off-axis polarisation purity (that is, the leakage of the total intensity into the polarised intensity as a function of position in the primary beam) at 1384 and 2368 MHz is about 1.6% and 9% respectively at the half-power point of the primary beam. However, Sault et al. (1999) points out that the process of mosaicing will tend to reduce this effect (since at each point, there are more samples over which to average), though the amount is not quantified. Lazendic et al. (2000) however, in a study of the supernova remnant N157B found beam polarization levels of up to 10% (with a corresponding electric vector orientation presented radially towards the beam centre) at the half-power point of the beam. This is because the mosaicing process does not manage to suppress the noise and instrumental polarisation at the edge of the field. This could be suppressed by using a linear imaging process (i.e., treat every pointing separately).

Furthermore, since we do not average the bandwidth before deconvolution and imaging, our observations will suffer from Faraday rotation across the bandwidth (which is particularly bad at 1384 MHz), this will lead to a decrease in sensitivity.

We also produced the fractional polarization maps, I_p/I, where I_p is the linearly polarized intensity and I is the total intensity. We find an average value through the Sgr B2 region to be ~ 2.2 ± 1.0%. Since the polarized intensity has a Ricean distribution where the mean is equal to the root-mean-square, we conclude that this is a null detection (and not a 2σ result). Though we also produced rotation measure (RM) maps of the region, the handling of polarization distributions is very difficult because of non-Gaussian statistics, and ambiguities in RM due to gaps in frequency coverage. Derived quantities such as position angles and RM images are very hard to interpret, often wrong, and well beyond the scope of this paper. Thus we use the noise statistics from the Stokes V images to place upper limits on the polarised emission from Sgr B2.

Upper limits on the polarized intensity from Sgr B2

Given that we do not find any significant levels of linearly polarized flux density coincident with the Sgr B2 cloud, we used the Stokes V images at 1384 and 2368 MHz to place a 5σ limit on polarized intensity from Sgr B2 of 3.5 and 3 mJy beam^{-1} respectively. In contrast to the upper limits on the polarized intensity above, the 5σ RMS error estimate in the total intensity images presented are 50 mJy beam^{-1} and 25 mJy beam^{-1} at 1384 and 2368 MHz respectively. The total intensity upper limits are much higher than the expected thermal noise errors due to the strong and complex structure in the region. That the upper limits for the polarized intensity are 14 and 8 times better than the total intensity images shows that

---

[4]available at: `http://www.narrabri.atnf.csiro.au/observing/users_guide/users_guide.html`

this provides a stronger constraint in the search for non-thermal emission from secondary electrons.

6.5   Search for synchrotron emission from secondary electrons

Protheroe et al. (2008) predicted that Sgr B2 could be a source of synchrotron radiation from secondary electrons and positrons created when CR nuclei interact with ambient molecular matter. The inability of the lower energy CRs ($\lesssim 100\,\text{GeV}$) to penetrate the densest regions of the cloud leads to a relative deficit of synchrotron emission from the dense core of Sgr B2. To test this, we use the radio images presented in Section 6.4 to search for synchrotron emission from secondary electrons in the Sgr B2 cloud. Using velocity-integrated images of the NH_3 emission (Ott et al., 2006) we compare the morphology of the radio emission and the molecular gas. We then search for non-thermal emission from the outer parts of the Sgr B2 cloud and attempt to separate this from the thermal emission in the region.

6.5.1   Morphology of the dense molecular gas

Figure 6.4 shows the velocity-integrated intensity image of the (1,1) line of NH_3 at 23 GHz for the Sgr B2 region. The emission observed in this image is consistent with the morphology of the region presented in Section 6.4.1 given that Sgr B2(M) and (N) are seen to be severely attenuated due to thermal bremsstrahlung absorption. This is consistent with the NH_3 line emission tracing the high resolution radio continuum emission from numerous HII regions in the dense cores of Sgr B2(M) and (N).

The NH_3 emission in this region also traces the larger outer envelope of emission in Sgr B2 which – as presented in Protheroe et al. (2008) – shows that the column density profile is consistent with a two-dimensional Gaussian with a standard deviation of $\sigma = 2.75 \pm 0.1$ pc (assuming a distance of 8.5 kpc) centered midway between Sgr B2(N) and Sgr B2(M). Comparing the NH_3 image with the 330 MHz image in Figure 6.2, there is some evidence of a similar morphology: both images reveal low-level emission surrounding Sgr B2, but not the thermal sources to the west of Sgr B2. Although we cannot rule out non-thermal emission due to sources along the line of sight (such as the Galactic synchrotron background), we decided to search for evidence of extended non-thermal emission from this region. We document in the following sections the use of the images described in Table 6.1 to derive flux densities within the Sgr B2 cloud and explore the possibility of limb-brightened emission from the outer envelope of Sgr B2.

6.5.2   Flux determination

Here we describe the determination of Sgr B2 flux densities for each frequency. We pay particular attention to the 330, 1384 and 2368 MHz flux densities, since these data are the lowest frequency available and therefore most likely to separate non-thermal emission from the overwhelming thermal emission in the region.

In general, the images that were available to us – other than our own data – could only be manipulated in the image plane since we did not possess all the raw data. Hence to obtain accurate flux density measurments, we have smeared the images to the lowest common resolution of $50'' \times 25''$ using the MIRIAD task *convol*. In the case of total flux densities within the entire cloud, each image was smeared to a resolution representing the 14 pc projected linear size of the cloud (assuming a distance to Sgr B2 of 8.5 kpc). The total flux
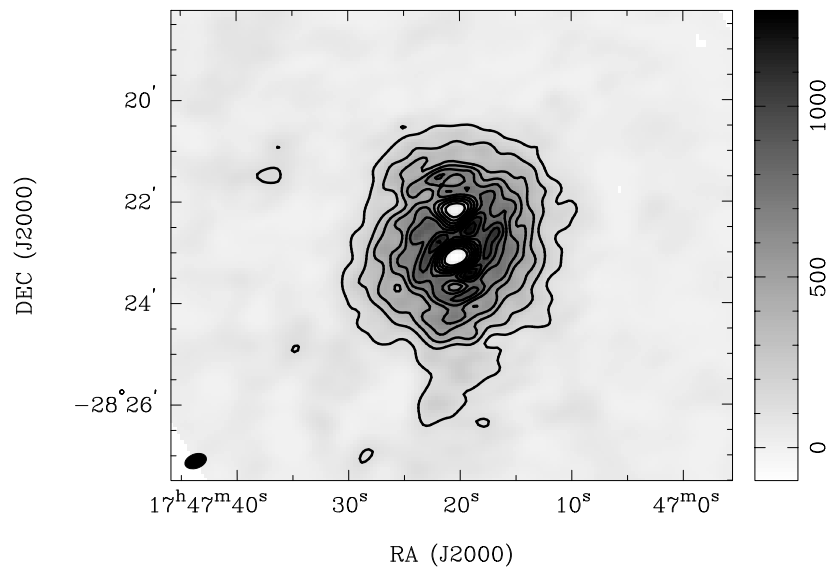
Figure 6.4: Image and contours showing the velocity-integrated intensity of the (1,1) line of NH_3 for the region around Sgr B2. Contours from 10% peak intensity until 90% peak intensity in increments of 10%. Note that around the Sgr B2(M) and Sgr B(N) HII regions, the NH_3 line emission is strongly attenuated due to thermal bremsstrahlung absorption. The beam is located in the lower left-hand corner of the image, and is $26 \times 17''$ at a position angle of $-70°$. The intensity scale, located on the right of the image is from -96 to 1280 K km s^{-1}.

density could then simply be read off as the peak flux density per beam. It must be noted that at 1384 and 2368 MHz, the flux densities derived in this section were calculated using the images *before* the addition of the single-dish data thereby providing an approximate correction for the baseline level of the flux density.

There are, however, two complicating factors here:

1. Sgr B2 is a complicated structure and, when deriving flux densities from such a large area, the nearby source Sgr B2(SC) will contribute to the total flux density. To produce an unbiased flux density, the flux density of Sgr B2 SC at every frequency (with the exception of 230 GHz, where the smaller primary beam does not include the SC) must be subtracted. Flux densities of the SC have been calculated at every frequency where the SC lies within the FoV, and are listed in Table 6.4. Thus the fluxes densities for main complex (MC), also listed in Table 6.4, have had the corresponding flux density due to the SC subtracted.

2. There are also complications from only dealing with images that have already been de-convolved. The analysis of errors and noise in the images is limited by that described in the literature, so that latent errors in the (u,v)-data and processing can affect the images without our knowledge and affect flux density determinations. The reader should bear this in mind.

The 230 GHz flux density determination was made from the summation of the individual components given in the paper describing the observations (Qin et al., 2006). The error given is also from that paper, and was not the result of our own analysis.

74 MHz flux density

In the 74 MHz VLA data there appears to be a slightly extended source located about 88″ to the north and 15″ to the east of the Sgr B2 cloud, with a peak flux density of 2.2 Jy. This does not appear at any other frequency. However, inspection of a cross cut of the region, reveals that this source is perched on top of a broad ridge of emission at the ~ 1.76 Jy beam^{-1} level. From a flux density of ~ 2.8 Jy, we estimate the source to be of extent ~ 1.29 beams, and subtracting off underlying emission from this, we calculate a corrected flux density of 1.1 Jy.

The extended source may be associated with Sgr B2, however intervening HII regions will absorb emission from Sgr B2. We have integrated the flux density over ~ 12 pc coincident with the Sgr B2 main cloud resulting in a flux density of ~ 14 Jy. Subtracting off the compact source, we place an upper limit on the flux density at 74 MHz of ~ 13 Jy from the Sgr B2 cloud within 12 pc. We stress again that at these low frequencies, since we can only derive a flux density limit we cannot provide a tight constraint of the possible non-thermal emission from Sgr B2.

ν (MHz)	$S_\nu^{<11pc}$ (Jy)	S_ν^{SC} (Jy)
74	< 13	—
330	—	0.8±0.4
—	4.1±2.0	0.8±0.4
—	4.1±2.0	2.6±0.5
843	8.3±4	—
1384	16.6±3.3	1.2±0.05
2368	20.3±1.0	0.73±0.02
23,000	46±1.0	—
230,000	49.5±0.1	

Table 6.4: Sgr B2 flux densities of the entire dataset. The 1384 and 2368 MHz observations were chosen to match the archival 330 MHz data available at the lower two resolutions. The 843 MHz datum is from the MOST Galactic Plane survey, and contains significant artifacts, primarily due to the Sgr A complex. The 23 GHz observations is the continuum component from the NH$_3$ data described in Protheroe et al. (2008), and the 230 GHz datum is from observations which do not cover the whole complex and miss large scale emission due to the smaller primary beam at the higher frequency. The error is the RMS noise error in the image, added, in quadrature, to (where possible) the systematic error.

Search for limb-brightening

For the reasons set out in Section 6.2, we searched the Sgr B2 molecular cloud complex for non-thermal synchrotron emission due to secondary electrons. Inspection of Figure 6.3 shows that Sgr B2 is surrounded by a number of extended sources at ~ 11 pc projected distance from Sgr B2(M) and (N). There are three sources in a line to the west of the main complex, and at least one to the east, possibly hinting at a ring-like structure. However, in section 6.4.1 we found that these sources are thermal in nature.

To explore possible extended non-thermal emission throughout the Sgr B2 region, we compared radial profiles of radio emission at different frequencies, as well as that of radio continuum and molecular emission.

Figure 6.5 (*Top*) shows a representative cross-section through Sgr B2. Figure 6.5 (*Bottom left*) shows log-linear plot along this cross section of the Sgr B2 cloud at 330 MHz (dot; medium resolution image) and 1384 MHz (dash) compared to the velocity integrated NH$_3$
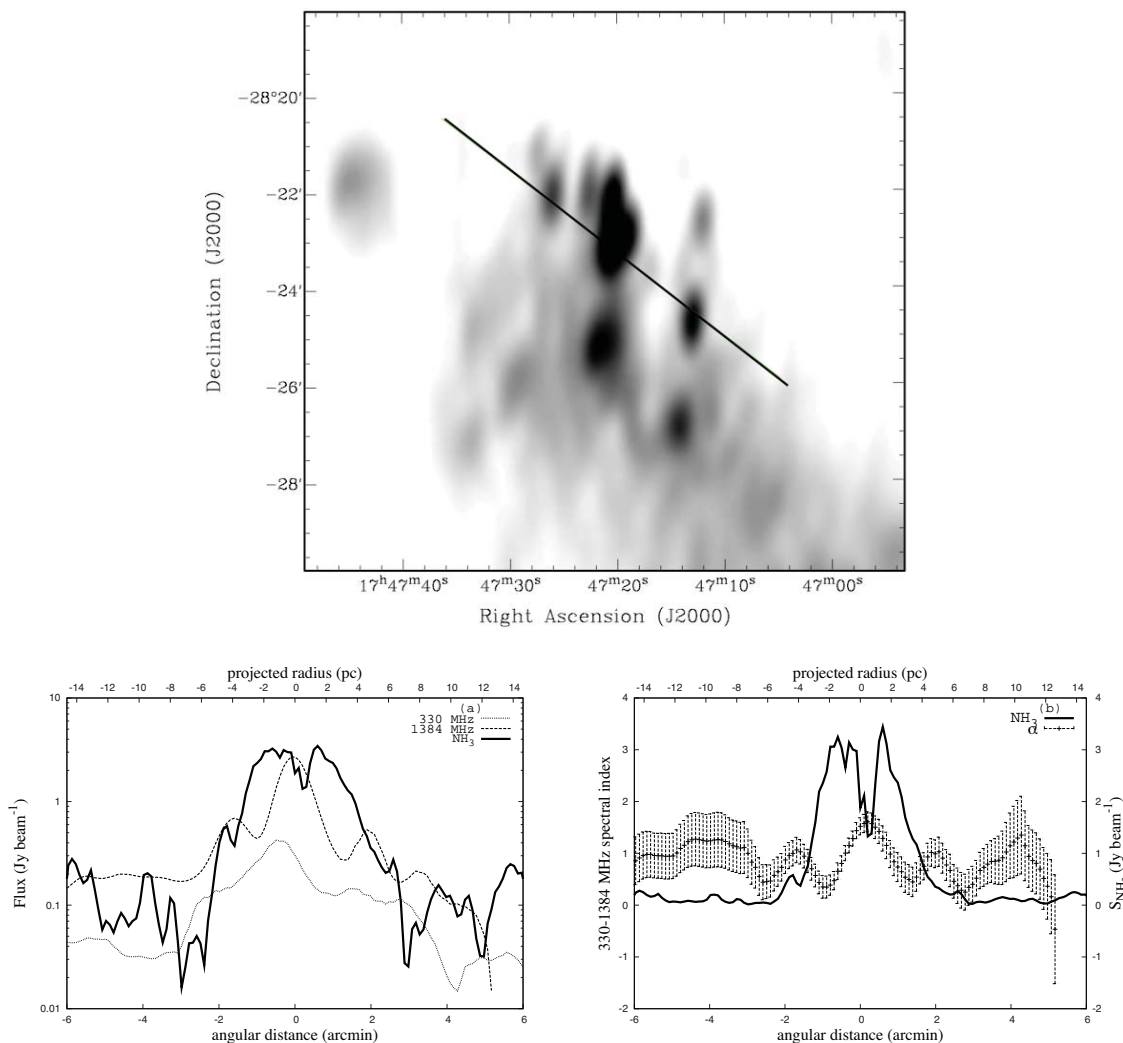
Figure 6.5: (*Top*): Total intensity 1384 MHz image of Sgr B2 showing the position of a typical cross section. The beam is $47'' \times 18''$. (*Bottom left*): Linear-log plot of the flux density cross section as a function of angular distance from the center of Sgr B2. The solid line is the NH_3 velocity integrated emission, whilst the dashed line is the 1384 MHz total intensity emission, and the dotted line is the 330 MHz medium resolution VLA emission. (*Bottom right*): Plot of the spectral index of total intensity emission between 330 and 1384 MHz images at a common resolution of $50'' \times 25''$, plotted with the NH_3 emission (solid line), as a function of angular position from the center of Sgr B2. Errors are calculated using standard error propagation of the spectral index. Note that the position of the NH_3 absorption corresponds to a peak in the spectral index between 330 and 1384 MHz emission.

emission (solid). Figure 6.5 (*Bottom right*) shows the spectral index between 330 MHz and 1384 MHz of the cross section on the left-hand axis, and the flux density of the NH_3 velocity-integrated intensity emission on the right-hand axis.

Figure 6.5 (*Bottom left*) shows that the emission at all frequencies plotted here is peaked at the center of the Sgr B2 cloud (the dip in the NH_3 is due to thermal bremsstrahlung absorption of the NH_3 line). The peak in the radio continuum emission is due to the large number of H II regions within Sgr B2(M) and (N). Morphologically, the ammonia emission is broad, having a flux density of at least a couple of hundred mJy beam^{-1} out to angular (linear) scales of $2'$ (~ 5 pc). The 330 and 1384 MHz emission seems to match this well, with a broad bed of radio continuum emission present in both images out to about $2'$ from the center of Sgr B2. This implies that the radio continuum emission broadly follows the

molecular emission. Figure 6.5 (*Bottom left*) also shows that at an angular (linear) distance from the center of Sgr B2 of $\sim 4'$ (11 pc), there appears to be an increase in the ammonia density of a factor of ~ 10 on either side. The modeling discussed in (Protheroe et al., 2008) indicates that possibility of non-thermal emission from secondary electrons could be greater in these regions. However, the increase in ammonia density is not matched by either: (i) an increase in radio continuum emission and (ii) non-thermal spectral indices as shown in Figure 6.5 (*Bottom right*).

Figure 6.5 (*Bottom right*) shows the same NH_3 flux density cross-section (solid line), this time plotted against the spectral index between 330 and 1384 MHz. This image was created using 330 and 1384 MHz images convolved to a common resolution of $50'' \times 25''$ and each resulting spectral index point with associated errors were calculated.

We note that the emission between 330 and 1384 MHz is thermal across the entire Sgr B2 region. The Sgr B2(SC) source in Table 6.3 has a non-thermal spectral indices between 1384 and 2368 MHz so that any cross-section taken with this source will exhibit non-thermal emission. No other cross-section taken gave a negative spectral index within the Sgr B2 main complex.

The above analysis shows that the radio continuum emission as a function of angular distance from the center of the Sgr B2 cloud is thermal. We can further this analysis by using the distribution of radio continuum emission to constrain the models of diffusive transport of CRs into the cloud, as presented in Protheroe et al. (2008).

Figure 6.6 (a) shows the average intensity of emission as a function of angular distance from the center of Sgr B2 at (a) 330 MHz and (b) 1384 MHz. The observational data in these plots was obtained using the MIRIAD task *ellint* and plotting the average intensity from the output of this task against the intensity as a function of angular distance from Figure 9 of Protheroe et al. (2008). The intensity (in Jy beam^{-1}) was then converted to intensity in the usual *cgs* units using the solid angle of the beam for the appropriate image.

Whilst Figure 6.6 (b) shows that the intensity distribution at 1384 MHz does not constrain the expected emission as a function of angle, the 330 MHz intensity does. Figure 6.6 (a) shows that the average intensity at 330 MHz implies, given reasonable assumptions about the CR spectrum at these energies, that the diffusive transport suppression factor as defined in Gabici et al. (2007) cannot be greater than $\chi \sim 0.01$ for a $B_\perp = 0.8$ mG. This reinforces limit found in Figure 10 of Protheroe et al. (2008) who, on the basis of the integrated flux density, found the the total flux from this region implies that for Sgr B2, $\chi < 0.02$. Figure 6.6 shows that, because of the highly peaked intensity distribution at 330 MHz, for a high (perpendicular component of the) magnetic field amplitude, cosmic-ray diffusion suppression factors larger than ~ 0.01 are excluded.

Altogether we conclude from the spectral analysis, that with the exception of Sgr B2(SC) there is (i) no evidence for any non-thermal emission from Sgr B2 and, therefore, (ii) no evidence of synchrotron emission from secondary electrons in Sgr B2. Using the average intensity from this region which shows that because of the highly peaked distribution at 330 MHz, we find evidence that the diffusive transport suppression factor, as defined in Gabici et al. (2007) cannot be greater than $\chi \sim 0.01$, lest a significant component of the average intensity be non-thermal. We note that in such as case, the spectral indices would be significantly lower (i.e. towards negative values) that that observed in Figure 6.5 (bottom).
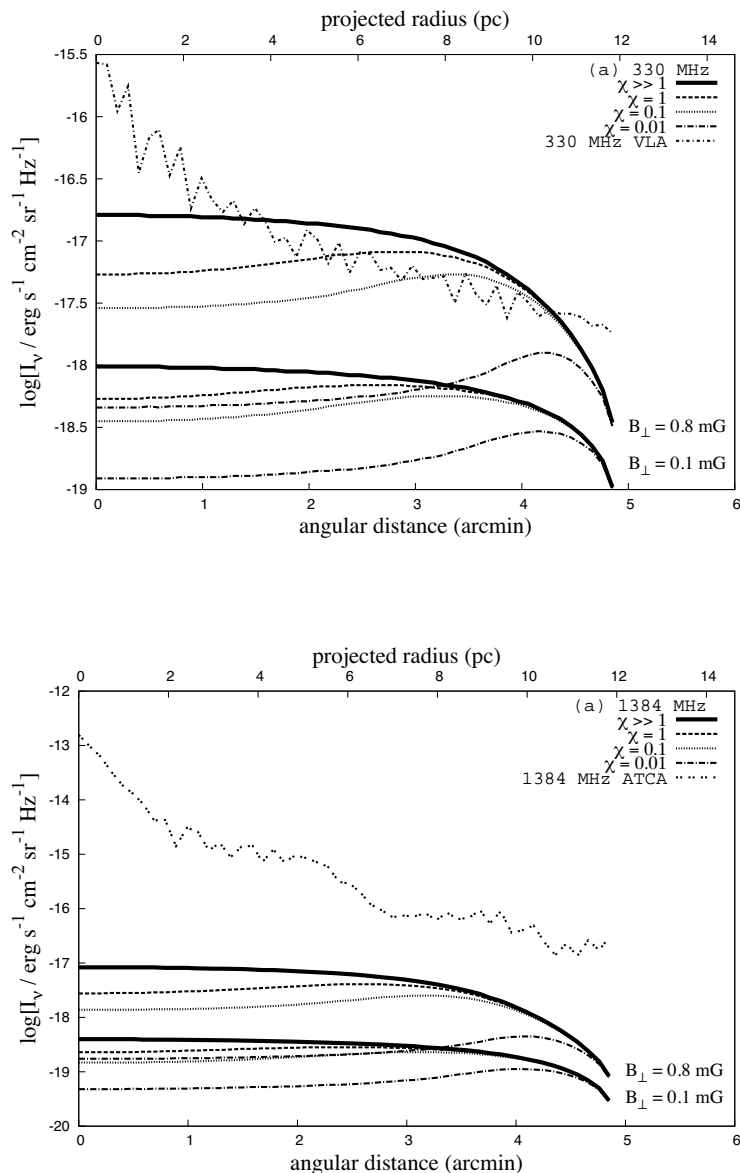
Figure 6.6: Comparison of the actual emission intensity as a function of angular distance from the center of Sgr B2 and that expected from models of synchrotron emission from secondary electrons at (a) 330 MHz and (b) 1384 MHz. The curves are for the parameters labelled and match those of Figure 9 of Protheroe et al. (2008).

6.6 Summary and conclusions

With an RMS sensitivity of 16 mJy beam^{-1} and a resolution of $27'' \times 8''$, we have presented sensitive, high resolution images of Sgr B region at 2.4 GHz. We have produced 1384 MHz images with the ATCA which match previously published images in sensitivity and resolution at an RMS sensitivity of 20 mJy beam^{-1} and a resolution of $47'' \times 18''$.

We have explored the spectral and morphological structures within Sgr B. We find that Sgr B1 is dominated by a small number (compared to Sgr B2) of extended structures, which are optically thin HII regions at 1.4 and 2.4 GHz. In contrast, Sgr B2 is dominated by a comparatively larger number of optically thick HII regions, such as Sgr B2(M) and (N), when compared to Sgr B1.

Motivated by our recent theoretical work presented in Protheroe et al. (2008) investigating the possibility of detecting significant synchrotron emission due to secondary electrons produced by interactions of ambient CRs with the nucleonic matter in Sgr B2, we combined new observations of the GC region with existing radio data of the region to characterise the emission in Sgr B2 from arcsecond to arcminute scales. We also chose frequencies which sample the spectral energy distribution of the region well, so that the spectral turnover of thermal emission, and any possible extended non-thermal emission could be well determined.

Our analysis employed archival 74/330 MHz VLA data at (in the case of the 330 MHz images) several different resolutions, matching the new ATCA 1384 and 2368 MHz observations, and archival MOST 843 MHz, ATCA 23 GHz and 230 GHz images and flux densities. Using these images, we have searched for extended non-thermal emission on several size scales (from the arcsecond scales of the images, up to the size of the entire cloud as suggested by NH_3 emission), finding no evidence for extended non-thermal emission (outside the Sgr B2(SC) source). Integration of emission over the angular scales suggested by the NH_3 observations and predictions from Protheroe et al. (2008) show that Sgr B2 exhibits optically thin and thick thermal emission due to the known UCHII regions at high frequencies ($\gtrsim$10 GHz) and thermal emission arising from one or more HII envelopes or winds with density gradients at all radio continuum frequencies.

We also produced polarized intensity images of Sgr B2, from which we were able to place 5σ limits on the polarized flux density of 3 and 3.5 mJy beam^{-1} respectively. Analysis of the RM image suggests that – provided that the polarized emission is not uniform over the beam and frequency band – any polarized emission will be depolarized due to Faraday rotation.

We have also searched for 'limb brightened' non-thermal emission expected given the probable exclusion of low energy ($\lesssim$ 100 GeV) CRs from the dense core of the Sgr B2 cloud. We looked for both morphological and spectral evidence of non-thermal emission using the lowest frequency, highest resolution images available using 330 MHz medium resolution VLA (LaRosa et al., 2000) and our 1384 MHz images. Every discrete source in Sgr B2 on arcsecond size scales, with the sole exception of Sgr B2(SC), including sources which appear at the correct projected distance and position suggested by our previous work, shows only thermal emission at all radio frequencies.

The only non-thermal emission observed near Sgr B2 – the Southern Complex, which because of the high densities derived from the NH_3 line-emission and small source size is not a significant source of synchrotron from secondary electrons. This is because for any suitable parameter set (i.e., magnetic field, linear size and ambient hydrogen density), an increase in the injection rate of secondaries is almost equally cancelled by the increase in efficiency of bremsstrahlung losses. Thus we place an upper limit on the synchrotron emission from secondary electrons of 1 mJy from Sgr B2(SC) at 1 GHz.

We conclude that *at these size scales* within the main complex of Sgr B2 we cannot find any morphological, spectral or polarization evidence for synchrotron emission due to any process.

7

ATCA radio continuum 1384 and 2368 MHz Observations of the Galactic Centre

7.1 Introduction

This chapter extends upon the work presented in the Chapter 6, by describing the spectral and morphological behaviour of sources in the Galactic center (GC) at 1384 and 2368 MHz at a resolution of $47'' \times 18''$ and $27'' \times 8''$ respectively. All images were produced with ATCA data in multiple array-configurations and have been combined with archival single dish data, resulting in images which are sensitive to emission from the resolution up to the scales of the size of the images at both 1384 and 2368 MHz.

As was alluded to in the previous chapter, the ATCA is the only aperture synthesis telescope capable of observing the GC with arcsecond resolution at 2.4 GHz. There have been many observations of the GC at other wavelengths (c.f. Section 6.2) however, 2.4 GHz remains underutilized in such a complex region. Thus this chapter explores the GC region at 2.4 GHz, which was observed as a part of the Sgr B observations presented in Chapter 6, but also includes archival data used to increase the sensitivity of the observations near Sgr A.

7.1.1 The Galactic Centre

The GC, by which in this chapter we mean the central ~ 200 pc in radius of our Galaxy, provides numerous complex and unusual sources such as the Radio Arc (and numerous non-thermal filaments (NTFs); Morris & Yusef-Zadeh 1985), the Sgr A complex (Pedlar et al., 1989), supernovae remnants, and many giant molecular clouds (GMCs).

There is a long-standing debate concerning the exact mechanism for particle acceleration at the GC. In particular, it is not known whether particles accelerated within SNRs can diffuse away from the parent remnant and permeate the region, or whether a stochastic acceleration mechanisms (such as first-and-second-order Fermi acceleration) are required to accelerate particles within the numerous cloud complexes, such as Sgr B, which are found in the region. Thus it is necessary to possess an accurate representation of the sources within the GC region.

7.2 Radio Continuum Observations

Table 7.1 lists the details of the observations taken with the ATCA, which are described in detail below.

ν (MHz)	$\Delta\nu$ (MHz)	Array	Time (hours)	Date
(1)	(2)	(3)	(4)	(5)
1384	128	1.5C	10	2005 December
		750A	10	2007 January
		750D	8	2007 March
		210	10	1999 November
		6A	19.95	1999 September
		6D	10.5	1999 September
2368	128	1.5C	10	2005 December
		750A	10	2007 January
		750D	8	2007 March
		210	10	1999 November
		6A	19.95	1999 September
		6D	10.5	1999 September

Table 7.1: ATCA Observational parameters

7.2.1   ATCA data

The images presented in this Chapter include data which was described in Chapter 6, and so will not be described in detail here. The data are the single pointing and mosaic mode 1384 and 2368 MHz observations in the 1.5 km and 750A/D ATCA array configurations respectively. In order to better characterize the complex emission from Sgr A at 1384 and 2368 MHz, we have obtained archival, single pointing-mode ATCA data for Sgr A[1] (Project code C802, P.I.: G. Bower). This data was taken with the 6C, 6D and 210m array-configurations of the ATCA which utilize antennae on an east-west track from 30 m to 210 m for the 210 m array-configuration and 77 m to 6 km for the 6C and 6D arrays. The primary and phase calibrators used in these observations were PKS 1934-638 and PKS 1748-253, respectively. The data were obtained using the same correlator as that described above at a frequency of 1384 and 2496 MHz.

7.2.2   Single-dish data

In order to fill in the missing short spacing information for the new ATCA images, we have obtained archival single dish data at 1408 and 2400 MHz from wide-field surveys obtained using the Effelsberg (EBG; Reich & Reich 1986) and Parkes (PKS; Duncan et al. 1995) telescopes respectively. Again, a more detailed description of this data can be found in Chapter 6 and will not be repeated here.

7.2.3   Image deconvolution

To produce the images presented in this paper, each set of interferometer data was calibrated separately using standard calibration procedures of the MIRIAD software package. Imaging was then performed by Fourier transforming the entirety of the interferometer data using the MIRAD task *invert*, and deconvolved using the MIRIAD task *mosmem*. A separate CLEAN image was produced with each single pointing data set in order to ensure that *mosmem* reconstructed the peak flux densities throughout the image correctly.

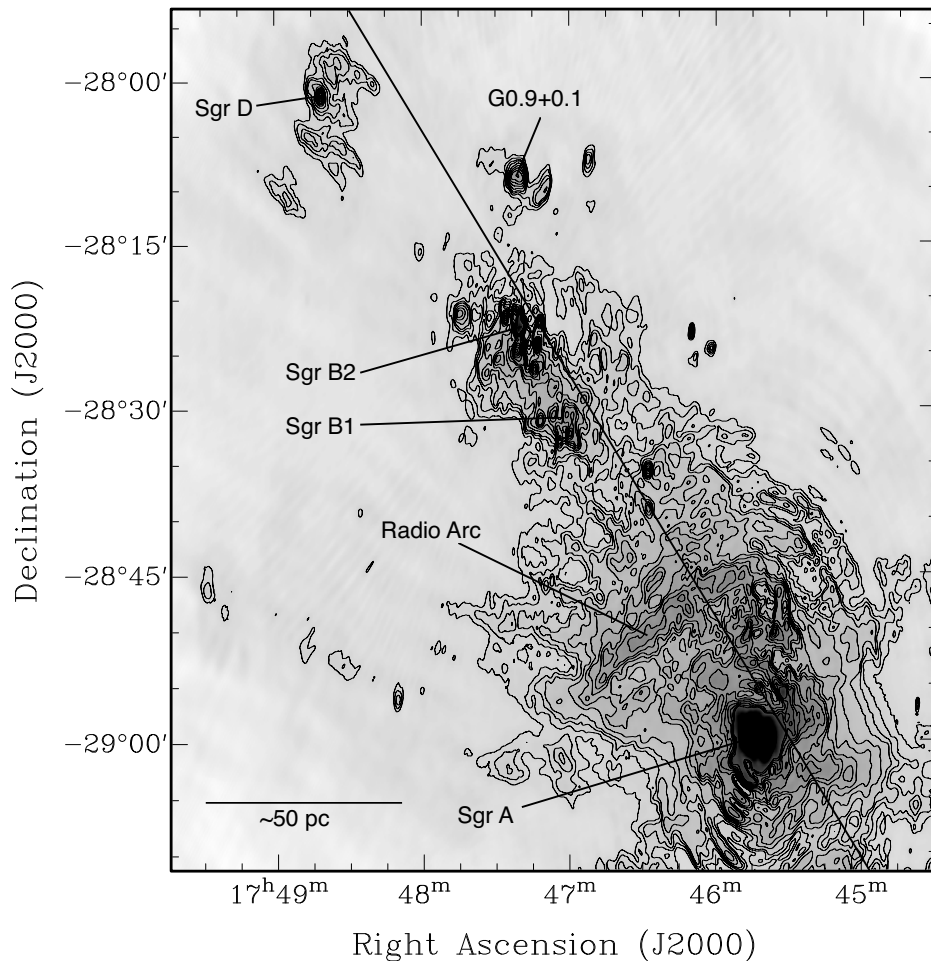[1]available at `http://atoa.atnf.csiro.au/`

Figure 7.1: ATCA+EBG total intensity image of the GC at 1.4 GHz overlaid with 1384 MHz total intensity contours at: 0.1, 0.12, 0.14, 0.18, 0.2, 0.24, 0.28, 0.3, 0.4, 0.5, 0.6, 0.7, 0.8, 0.9, 1, 2, 3, 4, 5, 6 and 7 Jy beam^{-1}. The resolution of the image is $47'' \times 18''$ with a position angle of $-4.8°$. More detailed maps of the major sources labelled here can be found in Figures 7.4 to 6.3. The solid line marks the approximate position of the Galactic plane.

Finally, the single dish data at 1.4 and 2.4 GHz from Duncan et al. (1995) and Reich & Reich (1986) described in Section 7.2.2 were combined with the interferometer data using the MIRIAD task *immerge* using the same method as described in Chapter 6.

7.3 Results & discussion

7.3.1 New ATCA/Parkes/Effelsberg images

Figures 7.1 and 7.2 show the entire region imaged using all data sets at 1384 and 2368 MHz respectively and have a resolution of $47'' \times 14''$ at 1384 MHz and $27'' \times 8''$ at 2368 MHz. The 1σ RMS noise in these images is 5 mJy beam^{-1} at 1384 MHz and 0.9 mJy beam^{-1} at 2368 MHz away from the Galactic plane, and 20 mJy beam^{-1} at 1384 MHz and 10 mJy beam^{-1} at 2368 MHz near the GC. Figure 7.2 is the highest-resolution, highest-sensitivity image of the GC at 2.4 GHz ever produced.

There have been many other images made of the GC at this wavelength (λ20 cm; Yusef-Zadeh & Morris (1987a), Pedlar et al. (1989), Yusef-Zadeh, Hewitt & Cotton (2004), for example), and we do not claim that the new ATCA+EBG 1384 MHz maps presented in Figure 7.1 are of a higher sensitivity.
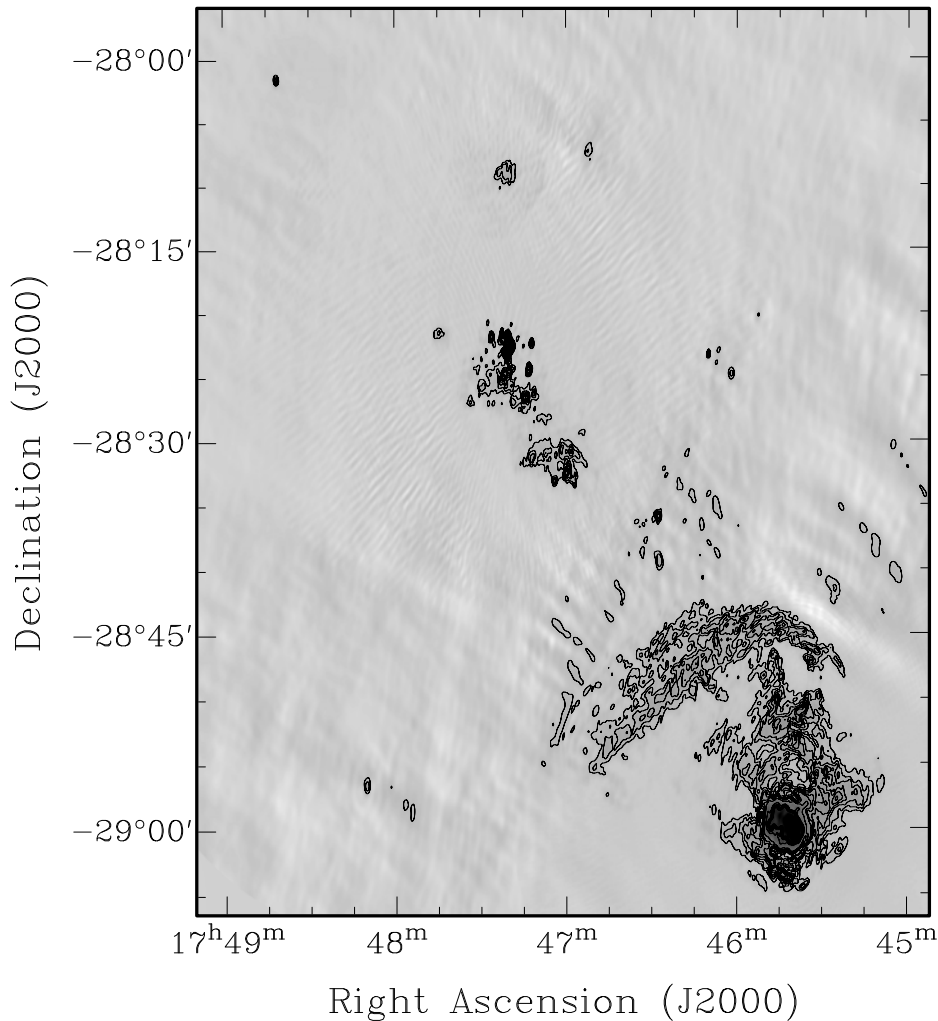
Figure 7.2: ATCA+PKS total intensity image of the GC at an average frequency of 2.4 GHz and a resolution of 27″ × 8″ with a position angle of −4.9°. The contours are the same total intensity at: 0.1, 0.15, 0.2, 0.25, 0.3, 0.35, 0.4, 0.5, 0.8, 1.0, 2.0, 3.0 and 3.5 Jy beam^{-1} .

7.4   Galactic center morphology

Figures 7.1 and 7.2 show the entire mosaic region at 1384 and 2368 MHz after combination with the single dish data. Figure 7.1 reveals significant extended emission from the Galactic plane at 1384 MHz. In contrast, Figure 7.2 demonstrates that at 2368 MHz, the GC region is dominated by strong point sources and bright extended emission regions, such as Sgr A and Sgr B, with little emission between these sources.

In this section we described the spectral and morphological aspects of the sources in the region and (where available) compare them to previous observations.

7.4.1   Sgr A (G0.0+0.0)

Sgr A is a large (∼ 7′) and extremely complex region which contains the dynamical center of our Galaxy, Sgr A* (this is believed to contain a supermassive black hole of mass M∼ $3.0 \times 10^6 M_\odot$; Melia & Falke 2001); a non-thermal shell structure, Sgr A East, believed to be a SNR; and a thermal spiral known as Sgr A West (Pedlar et al., 1989).

There is no published spectral study of Sgr A at 2368 MHz which is sensitive to structures on the same angular scales as Figure 7.2. Single dish observations show a peak of 320

Jy beam^{-1} at 2.417 GHz (Duncan et al., 1995), which matches the peak flux density obtained by convolving the ATCA+PKS data to the native resolution of the PKS data. This implies that at Sgr A the image in Figure 7.2 has the correct flux density scale.

At centimeter radio continuum wavelengths, Sgr A is extremely bright with Pedlar et al. (1989) measuring a total flux for the Sgr A region of $> 370 \pm 50$ Jy and 487 ± 30 Jy at 330 and 1400 MHz respectively (the 330 MHz flux is a lower limit due to absorption against Sgr A West). At 1384 MHz, we find 460 ± 30 Jy from Sgr A, consistent with that found from Pedlar et al. (1989). We measure an integrated flux of 468 ± 23 Jy at 2368 MHz as presented in Table 7.2. From integration of the flux density within the central $\sim 4'$ we find flux density of 220 ± 11 Jy and 160 ± 8 Jy at 1384 and 2368 MHz, respectively. This flux includes emission from Sgr A*, Sgr A West and East.
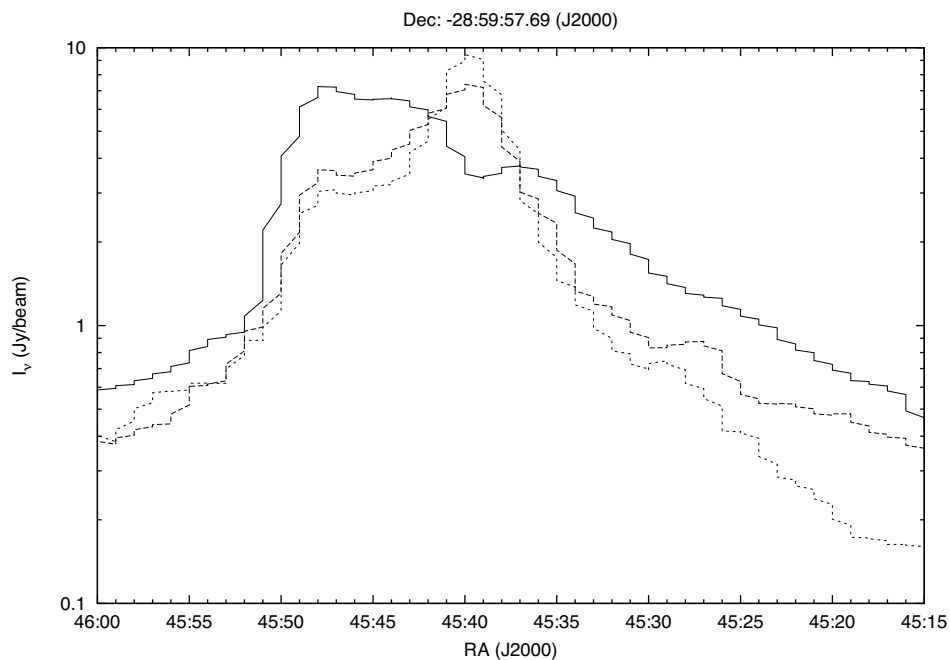

Figure 7.3: A cross-section of Sgr A at a Declination (J2000) of: -28:59:57.69 at 330 MHz (solid; LaRosa et al. (2000)), 1384 MHz (dash) and 2368 MHz (dot). This illustrates the same features as in Figure 7 of Pedlar et al. (1989), namely: the absorption of the 330 MHz emission by Sgr A West (which is observed as the peak of emission in the 1384 and 2368 MHz emission); the broad feature of the Sgr A complex; the broad feature of the halo emission; and a background emission on which the Sgr A complex sits.

Using cross-sections to subtract background emission, Pedlar et al. (1989) found the halo emission to be a mixture of thermal and non-thermal emission between 0.3 and 43 GHz. Figure 7.3 shows a similar cross-section in Right Ascension to that shown in Figure 11 of Pedlar et al. (1989), which shows the 330 MHz medium resolution image (LaRosa et al., 2000) (solid), our 1384 MHz ATCA+EBG image (dash) and our 2368 MHz ATCA+PKS image (dot). We have used this to estimate the background flux density to subtract from our 1384 and 2368 MHz images, which we have estimated to be ~ 0.4 Jy beam^{-1}, thus we find that ~ 85 Jy of flux density is required to be subtracted from the flux density derived for the halo because of background emission. The fluxes for the halo emission presented above and in Table 7.2 have had this flux density subtracted. It is important to note that the 2368 MHz emission (dotted line in Figure 7.3) has a background flux density which is lower to the west of the cross-cut, so that the amount of flux density we attribute to the background at 2368 MHz is actually an upper limit so that the inference presented above is somewhat

contrary to that presented in Pedlar et al. (1989).

The fluxes derived for the halo imply a spectral index between 1.4 and 2.4 GHz of $\alpha = 0.7 \pm 0.3$. However, the 1.4 GHz flux derived above is significantly below that found by Pedlar et al. (1989), most likely due to the complex nature of this source and the great difficulties inherent in properly assigning flux densities to each source within the region. Thus we conclude that the 1.4 GHz datum derived here is most likely a lower limit and hence the spectral index of $\alpha = 0.7 \pm 0.3$ is an upper limit. We suggest that the 2.4 GHz flux of 232 ± 12 Jy is accurate and thus consistent with the turnover of the halo spectrum at frequencies below 1.4 GHz as found in Pedlar et al. (1989).
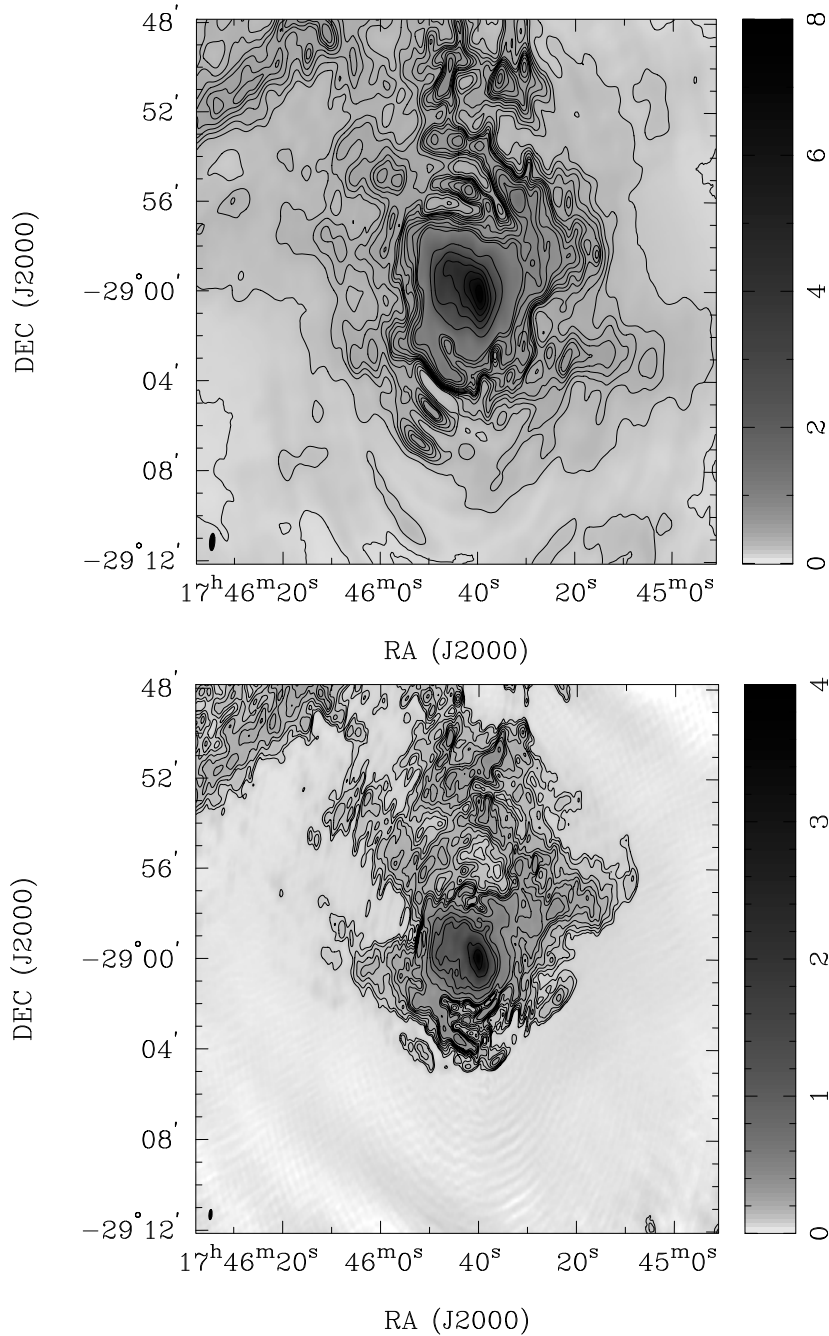

Figure 7.4: Total intensity image of the Sgr A region at 1384 MHz (*Top*) and 2368 MHz (*Bottom*). The 1384 MHz contours are at 0.2, 0.3, 0.4, 0.6, 0.8, 1.0, 1.3, 1.6, 2.0, 3.0, 4.0, 5.0, 6.0, and 7.0 Jy beam^{-1} with a resolution of $47'' \times 14''$ and an intensity scale on the right in units of Jy beam^{-1}. The 2368 MHz image has contours at 0.08, 0.1, 0.13, 0.16, 0.2, 0.23, 0.26, 0.3, 0.4, 0.6, 0.8, 1.0, 2.0, and 3.0 Jy beam^{-1} and has a resolution of $28'' \times 9''$.

Morphologically, Figure 7.4 shows a peak of emission coincident with Sgr A (though we cannot distinguish whether the peak is due to Sgr A* or Sgr A West at these resolutions for both frequencies) and an extension towards the east. The eastern extension is probably due to the non-thermal shell structure of Sgr East, which is only beginning to be resolved at 2368 MHz. At both 1348 and 2368 MHz, there is a region of extended emission known as the 'halo' (Pedlar et al., 1989).

7.4.2 Radio Arc (G0.02-0.0) & Arched Filaments (G0.07+0.04)

High resolution studies of this region at 1.4 GHz with the VLA ($12'' \times 11''$; Yusef-Zadeh, Hewitt & Cotton 2004) reveal a number of long, thin filaments known as non-thermal filaments. These NTFs, known collectively as the Radio Arc, are intersected by a number of elongated and filamentary HII regions known as the Arched Filaments (G0.07+0.04). The Arched Filaments are thought to be ionized by two clusters of hot stars known as the Arches and Quintuplet clusters (Yusef-Zadeh, Hewitt & Cotton (2004) and references therein). This region is shown in Figure 7.5 at 1384 and 2368 MHz. These images show a single, long filamentary structure running perpendicularly to the Galactic Plane which is similar to the morphology observed at 330 MHz by Pedlar et al. (1989). However, in Figure 7.5, the emission blends several filaments together, resulting in emission which is extended parallel to the plane. The Radio Arc is connected to Sgr A via the Arched filaments. There are at least three filaments present in the images presented in Figure 7.5. These are HII regions that have been elongated due to gravitational interaction with Sgr A (Yusef-Zadeh & Morris, 1987b). Spectral index maps of this region reveal the emission from these sources to be optically thick between 1.4 and 2.4 GHz, consistent with these objects being HII regions. The same maps show that the Radio Arc is dominated – especially at lower Galactic longitudes – by non-thermal emission. This picture is consistent with that found at higher frequencies (4.5 and 8 GHz) by Law et al (2007).

At lower frequencies, Figure 1 of Pedlar et al. (1989) shows 330 MHz emission which is at a similar resolution to the 1384 MHz image presented in Figure 7.5. The 1384 MHz map shows a morphology which is similar to, but consisting of more point source emission, when compared to the single filamentary structure seen in Pedlar et al. (1989); consistent with the mixture of thermal and non-thermal emission expected at 1384 MHz.

Figure 7.5 shows the Radio Arc at 1384 MHz (*Top*) and 2368 MHz (*Bottom*); a broad region of sources and large scale emission aligned perpendicularly to the Galactic plane. The Radio Arc is a complex region consisting of a combination of thermal and non-thermal emission. The non-thermal emission is mainly due to the numerous NTFs (thought to be generated by relativistic electrons emitting synchrotron radiation in the presence of strong magnetic fields (Yusef-Zadeh, Morris & Chance, 1984)), as resolved by higher resolution observations using the VLA $\sim$ 1.4 GHz ($12'' \times 11''$; Yusef-Zadeh, Hewitt & Cotton 2004). The thermal emission originates from three prominent HII regions known as the Arched filaments (G0.07+0.04), the Sickle (G0.18-0.04) and the Pistol (G0.16-0.06).

Figure 7.5 (*Top*) and (*Bottom*) shows that at 1384 MHz and 2368 MHz, the Radio Arc is resolved into a complex structure of HII regions and non-thermal filaments. The Radio Arc consists of a number of linear filaments, which due to the low resolution of the 1384 MHz map in Figure 7.5 are convolved into a single filament.

Also seen in Figure 7.5 are the Arched filaments, elongated HII regions observed within the Radio Arc structure which are thought to be ionized by two clusters of hot stars known

Name	R.A. (J2000)	Dec. (J2000)	$I_{1.4}$ (Jy beam^{-1})	$I_{2.4}$ (Jy beam^{-1})	$S_{1.4}$ (Jy)	$S_{2.4}$ (Jy)	α
(1)	(2)	(3)	(4)	(5)	(6)	(7)	(8)
Sgr A (total)	17:45:40	-29:00:28	7.5	3.8	461 ± 30	468 ± 23	0.03 ± 0.3
Sgr A (halo)	—	—	—	—	156 ± 8	232 ± 12	0.7 ± 0.3
Sgr A^a	—	—	—	—	220 ± 11	160 ± 8	−0.6 ± 0.3
G0.9+0.1 (total)	17:47:21	-28:09:05	0.6	0.4	12.1 ± 0.6	14.3 ± 0.7	0.3 ± 0.04
G0.9+0.1 (core)	—	—	—	—	6.5±0.3	6.2±0.3	−0.1 ± 0.7
G0.9+0.1 (shell)	17:47:09	-28:10:23	—	—	5.6±0.3	8.1±0.4	0.7 ± 0.5
Sgr D total^b	17:48:41	-28:01:38	2.0	0.5	19.7 ± 1.0	14.3 ± 0.7	−0.6 ± 0.3
G1.13-0.10	—	—	2.0	0.5	12.2 ± 0.6	15.1 ± 0.8	0.4 ± 0.3
G1.13-0.10(3)	17:48:41	-28:01:38	2.02	0.5	2.02 ± 0.10	2.04 ± 0.10	—
SNR G1.05-0.15	17:48:41	-28:01:38	0.7	0.1	7.5 ± 0.4	6.3 ± 0.3	−0.3 ± 0.6
SNR G1.0-0.2	1.0	-0.2	1.04	0.8	14.1	—	—

Table 7.2: Galactic center Source characteristics. ^{a} Sgr A denotes the region which includes Sgr A*, Sgr A(West), and Sgr A(East). ^{b} The total flux density for Sgr D has had a background subtracted, whereas the individual conponents have not. Thus the sum of the components does not equal the total flux.

as the Arches and Quintuplet clusters (Yusef-Zadeh, Hewitt & Cotton (2004) and references therein). These sources are Hɪɪ regions which are elongated, and due to the lower angular resolution at 1384 MHz convolved into two sources which extends from the northernmost point of the Sgr A halo. The 2368 MHz image resolves the filaments into a number of point sources, consistent with the observations at ~ 1400 MHz of Yusef-Zadeh, Hewitt & Cotton (2004).

Although at 2368 MHz there are a number of point sources and some evidence of filamentary structure (consistent with lower frequency data), we do not believe that this represents the actual structure in this region at this frequency. The evidence for this is that single dish observations, such as Reich & Reich (1986) show a strong source reminiscent of the Radio Arc at 1384 MHz shown in Figure 7.5 (*Top*) – this source does not diminish in intensity at higher frequencies either: Law et al (2007) give spectral indices between 4.85 and 8.5 GHz of -0.54, implying that the emission at these frequencies is still dominated by the same relativistic electrons which produce the emission at 330 and 1384 MHz (that is, the ~ 1 mG magnetic fields measured in these structures (Yusef-Zadeh, Morris & Chance, 1984) do not lead to catastrophic synchrotron losses, which could lead to the steep spectral indices which are observed in the images shown in Figure 7.5 between 1384 and 2368 MHz).

The similarity of the 1384 MHz emission presented here, as compared to the 330 MHz emission presented in Pedlar et al. (1989) are that of a large region of emission surrounding the GC region, extending almost to Sgr B containing a region of radio emission elongated in a direction perpendicular to the Galactic plane – thought to be generated by relativistic electrons emitting synchrotron radiation in the presence of strong magnetic fields (Yusef-Zadeh, Morris & Chance, 1984).

The images of this region presented in Yusef-Zadeh, Hewitt & Cotton (2004) show this region being comprised of numerous filaments aligned side-by-side. Due to the low resolution of the images, we do not resolve these individual sources. Figure 7.5 (*Top*) and (*Bottom*) differ from the 330 MHz image of (Pedlar et al., 1989) in the region of – however, both images presented here are consistent with the 1400 MHz observations of Yusef-Zadeh, Hewitt & Cotton (2004).
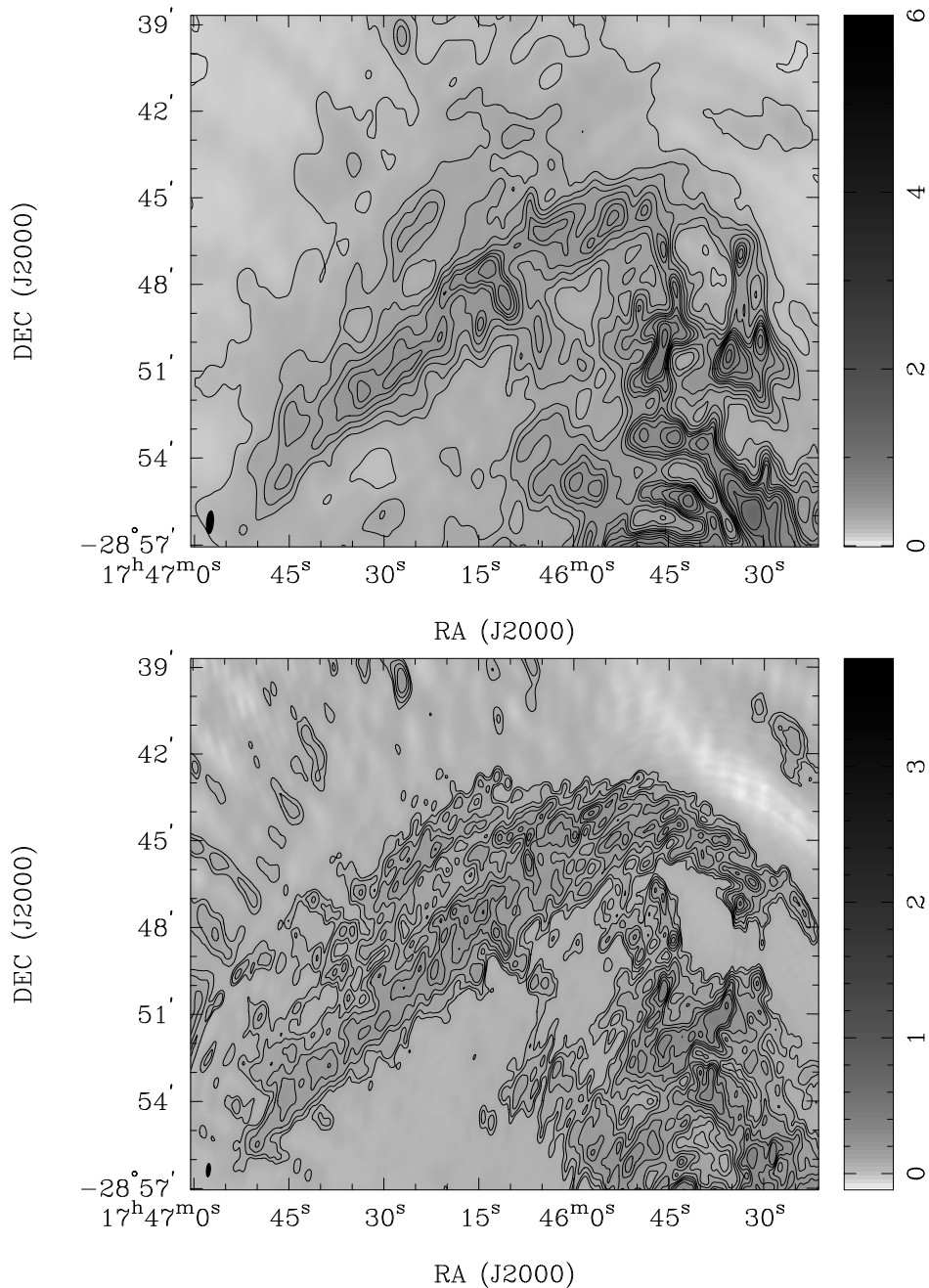
Figure 7.5: Same as Figure 7.4, but for a region including the Radio Arc and Arched Filaments

7.4.3 SNR G0.9+0.1

G0.9+0.1 is a radio composite SNR consisting of a pulsar wind nebula (PWN) surrounded by a fainter shell of emission spectrally distinct from the PWN (Dubner et al., 2008). It is characterized by a bright core, shown to have a flat radio spectrum ($\alpha \sim -0.12$; Helfand & Becker 1987) between 1.4 and 5 GHz, and $\alpha \sim +0.12$ between 0.3 and 1.4 GHz (LaRosa et al., 2000). Surrounding the bright core is a shell of radio emission which is non-thermal; $\alpha \sim -0.77$ between 0.3 and 1.4 GHz and $\alpha \sim -0.6$ between 1.4 and 5.0 GHz. The spectral and morphological structure is reproduced at high energies by X-ray and γ-ray observations (Aharonian & Neronov (2005), Dubner et al. (2008) and references therein) – although the H.E.S.S. observations do not have sufficient resolution to separate the two components of this source source at energies higher than 100 GeV. High resolution X-ray observations

of the core reveal a PWN nebula consisting of a torus and jet structure (Gaensler et al., 2001) coincident with the peak of the radio continuum emission. Lower resolution X-ray observations of the core also reveal structures which broadly follow the radio continuum emission (Dubner et al., 2008).
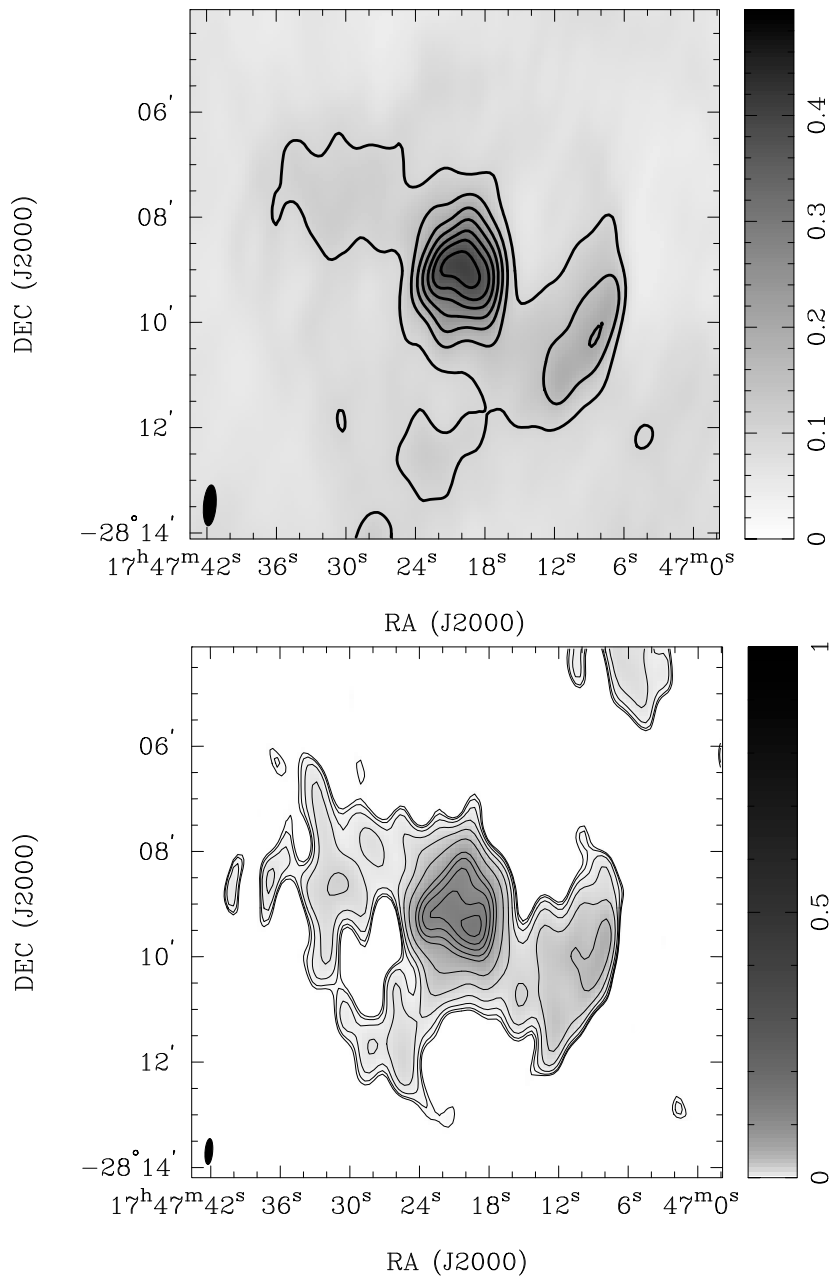

Figure 7.6: Total intensity images of the SNR G0.9+0.1 at 1384 MHz (*Top*) at a resolution of $48'' \times 17''$ and 2368 MHz (*Bottom*) at a resolution of $29'' \times 9''$. The 1384 MHz image has total intensity contours at: 100, 150, 200, 250, 300, 340, and 380 mJy beam^{-1}, whilst the 2368 MHz image has total intensity contours at: 1, 2, 4, 8, 16, 32, 64, 80, 100, 120 mJy beam^{-1}. The beam is shown in the bottom left-hand corner of each image.

Figure 7.6 shows total intensity images of G0.9+0.1 at 1384 and 2368 MHz. The morphology at both frequencies is consistent with previous observations: a bright core, corresponding to the PWN, surrounded by a faint shell of emission.

The 1384 MHz image is not of sufficient resolution to distinguish features within this overall structure. At a resolution of $27'' \times 8''$, the 2368 MHz image allows us to distinguish the larger morphological features observed in the PWN at higher resolutions, as presented

in Dubner et al. (2008). The morphology observed in Figure 7.6 (*Bottom*) shows a bar of emission, coincident with the peak of emission at 1384 MHz, running from the NE to the SW of the core. This feature is also seen and further resolved into individual components at higher resolutions in Figure 4 of Dubner et al. (2008). Figure 7.6 (*Bottom*) also exhibits a ring-like extension to the east of the core, consistent with a number of features which in Dubner et al. (2008) are resolved into two bright clumps – M1 and M2 – and a vertically aligned filament, called Filament 2. Finally, the 2368 MHz image also shows a northerly extension of the core, coincident with features observed at higher resolutions (Dubner et al., 2008).

Table 7.2 lists the fluxes derived from the images presented in Figure 7.6. We have derived these fluxes using the process described by LaRosa et al. (2000) at 330 MHz for this source. The flux density for the complete source was derived by integrating the flux density within a $7.2' \times 7.0'$ box centered on the PWN source at 1384 MHz. The 2368 MHz flux density was derived in the same manner after the image was regridded to – and convolved to the beam-size of – the 1384 MHz image presented in Figure 7.6 (*Top*). The flux density of the core was derived by integrating within a $2' \times 2'$ box centered on the peak of radio emission. The flux density within the shell is then the difference between the total and core fluxes. We note that the similar resolution and interferometric spacings of the 330 MHz data of LaRosa et al. (2000) and the images presented here make a direct comparison of fluxes more accurate than the higher resolution images of Dubner et al. (2008).

We find a total flux density of 28.6 ± 1.5 Jy for G0.9+0.1 at 1384 MHz and 26.8 ± 1.3 Jy at 2368 MHz. Since there will be a contribution from diffuse background emission to this flux, we follow a similar method to LaRosa et al. (2000) to remove this emission from the total flux density by taking the average flux density of similar size boxes close to the source (containing no obvious sources). Doing this, we find a background flux density at 1384 MHz of 16.5 ± 0.8 Jy and 12.5 ± 0.6 Jy at 2368 MHz, which places the total flux density for G0.9+0.1 at 12.1 ± 0.9 Jy at 1384 MHz and 14.3 ± 1.0 Jy at 2368 MHz. The errors were determined by adding in quadrature the systematic error of 5% in both the total and background flux. The shell is non-thermal with a spectral index of −0.7, as stated in Table 7.2. For the central source, we find 6.5 ± 0.3 Jy at 1384 MHz and 6.2 ± 0.3 Jy at 2368 MHz – consistent with the 330 MHz flux density stated in LaRosa et al. (2000) and a flat spectrum.

At 2368 MHz, we find that out of a background-subtracted total flux density of 14.3±0.8 Jy, 3.1 ± 0.16 Jy is from the central source. This is consistent with a spectral index of $\alpha \approx$ −0.2 ± 0.02 found between 330 and 2368 MHz. We find a flux density for the central core at 1384 MHz of 6.5 ± 0.3 Jy, which is as expected for a spectral index of $\alpha \sim$ −0.7 between 330, 1384 and 2368 MHz. The difference between the central core and background-subtracted fluxes – 9 ± 0.5 Jy – is the flux density due to the shell and diffuse emission

We argue that this is a lower limit to the extended flux density because of the extremely bright nature of Sgr B at 2368 MHz limiting the ATCA's ability to pick up the extended diffuse emission of the shell (similar to that found at 5 GHz in Dubner et al. 2008).

7.4.4 Sgr D (G1.1-0.1) and SNR G1.0-0.2

At the edge of the mosaic area there is a complex of radio emission collectively known as Sgr D. Molecular and absorption line studies were originally interpreted as locating the Sgr D HII region on the far side of the GC (Mehringer et al., 1998). Recent studies, however, have cast doubt on this (Sawada et al. (2008) and references therein) and place Sgr D on the

near side of the GC.

Regardless of the de-projected geometry of the region, Sgr D is thought to consist of a bright 'blister' HII region in the north and a SNR, G1.05-0.15 in the south (Odenwald, 1989). The relatively high resolution (10″) VLA images at 18 cm (~ 1.66 GHz) obtained by Mehringer et al. (1998) show that the HII region is dominated by a point source which is surrounded by low-intensity, diffuse emission thought to be created by photons escaping from the Sgr D core to ionize the surrounding matter. The SNR is shell-dominated and consists of a bright arc of radio emission just to the south of the HII region and a region of lower-intensity emission. Lower resolution MOST images at 843 MHz (Gray, 1994a,b) show that there is another shell of emission near the bright arc and a corresponding arc at the south-easterly extent of the source. The MOST images also show the object to be filled with low-intensity diffuse emission.
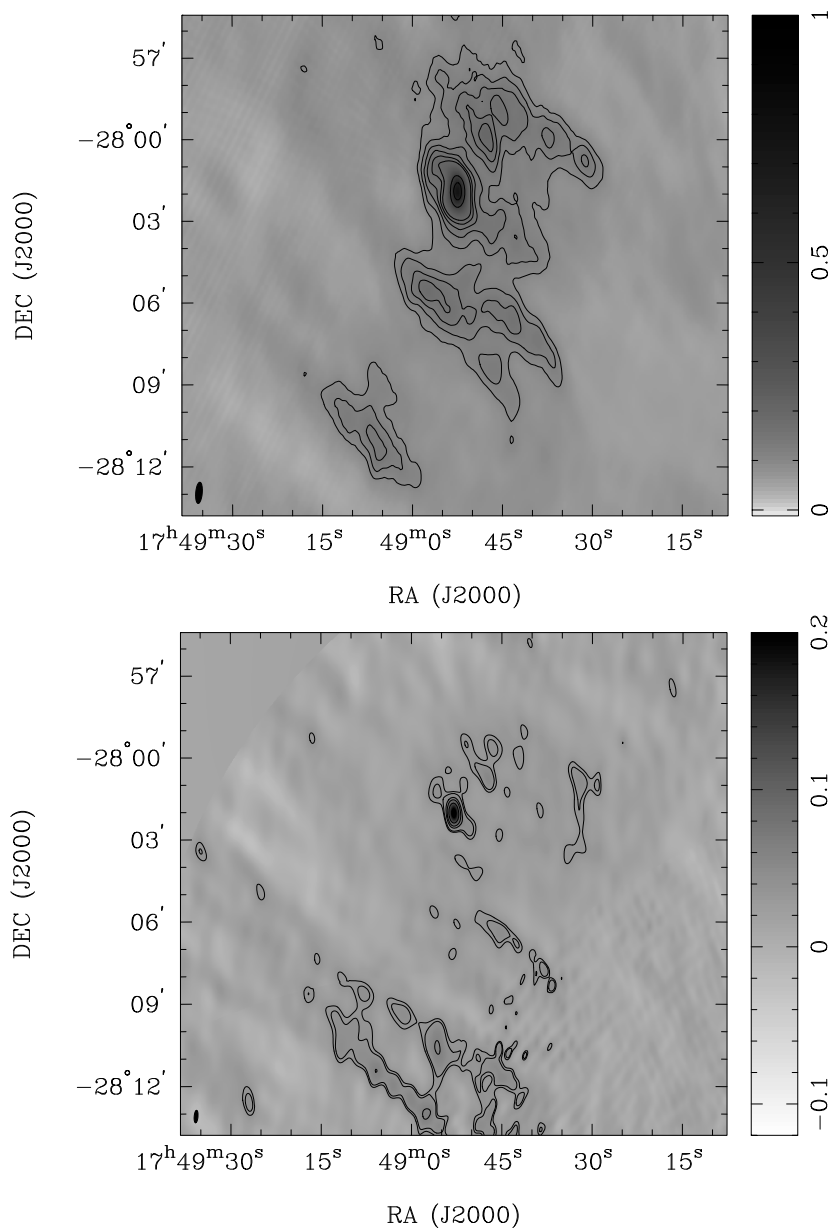

Figure 7.7: Total intensity images of Sgr D at 1384 MHz (*Top*) and 2368 MHz (*Bottom*). The 1384 MHz image has a resolution of 107″ × 67″ overlaid with contours at: 100, 120, 140, 160, 180, 200, 400, 600 mJy beam^{-1} whilst the 2368 MHz image has a resolution of 29″ × 9″ and contours at: 35, 40, 60, 80, 120, and 200 mJy beam^{-1} .

The lower resolution images presented in Figure 7.7 at 1384 MHz (*Top*) and 2368 MHz (*Bottom*) are consistent with the general morphology at 843 and 1660 MHz. At both 1384 and 2368 MHz, the whole Sgr D region is dominated by the point source (labeled as 3 in Mehringer et al. 1998), from which we measure a flux density of 2.0 ± 0.1 Jy at 1384 MHz and 2.0 ± 0.1 Jy at 2368 MHz, consistent with the fluxes presented in Mehringer et al. (1998) assuming an optically thin HII region. For the HII region, we measure a total flux density of 12.6 ± 0.6 Jy at 1384 MHz and 15.1 ± 0.8 Jy at 2368 MHz (compared to > 9.5 Jy at 5.0 GHz and 14.5 Jy at 1.667 GHz; Mehringer et al. 1998), broadly consistent with an HII region. It is important to note that the fluxes derived here are somewhat approximate given that the source is near the edge of the 2368 MHz beam.

Figure 7.7 shows that the morphology of SNR G1.05-0.15 is consistent with the image at 843 MHz of Sgr D from Gray (1994b) as described above. From this region, we find a flux density of 7.5 ± 0.4 Jy at 1384 MHz and 6.3 ± 0.3 Jy at 2368 MHz. We note again that the fluxes presented here are somewhat uncertain for the reasons presented above.

7.5   Summary and conclusions

With an RMS sensitivity of 5 mJy beam^{-1} and a resolution of $27'' \times 8''$, we have presented sensitive, high resolution images of the GC region at 2.4 GHz. Additionally, we have produced 1384 MHz images with the ATCA which match previously published images in sensitivity and resolution at an RMS sensitivity of 20 mJy beam^{-1} and a resolution of $47'' \times 18''$. We have used these observations to undertake a spectral and morphological study of the GC at positive Galactic latitudes, up to $\sim 1°$. Overall, we find that the GC at 1.4 GHz contains much extended emission, which is largely absent at 2.4 GHz, suggesting that this emission is created by synchrotron emission from free electrons within the Galaxy.

For the most part, we find that the morphological structure and spectral behavior of sources such as Sgr B, D and G0.9+0.1 in this region is consistent with published images and spectra at other frequencies. For the first time, we have attempted to separate the flux density from the Sgr A complex at 2.4 GHz. We find that Sgr A (which includes emission from Sgr A*, Sgr A West and East) is consistent with published fluxes at 1384 MHz, and that both the ~ 1.4 GHz and ~ 2.4 GHz fluxes are consistent with spectra from published, higher-resolution studies of Sgr A, such as Pedlar et al. (1989). We estimate a (background subtracted) 2368 MHz flux density for the $\sim 7'$ halo of emission surrounding Sgr A of 232 ± 12 Jy, consistent with a spectral turnover below 1.4 GHz as determined by Pedlar et al. (1989).

We have used these observations to described the morphology and spectral features of all the major GC sources to the west of Sgr A. Morphologically, we observe structures which are consistent with those observed at other frequencies for all major objects. We find that our observations are either consistent with, or provide lower limits to, flux densities from cataloged sources,when compared to previous observations. We note that due to a lack of previously-published flux densities at 2368 MHz, these lower limits are inferred from the spectral behavior at frequencies straddling this frequency.